Combining RBS/Channeling, X-ray diffraction and atomic-scale modelling to study irradiation-induced defects and microstructural changes

Xin Jin

UNIVERSITÉ DE LIMOGES

École Doctorale Sciences et Ingénierie des Matériaux, Mécanique, Énergétique (ED 609)

Institut de Recherche sur les Céramiques (IRCER)

Année : 2021

Thèse

pour obtenir le grade de

DOCTEUR DE L'UNIVERSITÉ DE LIMOGES

Discipline : Physique

présentée et soutenue par

Xin JIN

le 24 02 2021

Combining RBS/Channeling, X-ray diffraction and atomic-scale modelling to study irradiation-induced defects and microstructural changes

Thèse dirigée par Alexandre Boulle et Aurélien Debelle

JURY :

Patrice Gergaud	Directeur de Recherche, CEA LETI, Grenoble	Rapporteur
Katharina Lorenz	Principal Researcher, Universidade de Lisboa	Rapporteur
Marie-France Barthe	Directeur de Recherche, CNRS, CEMTHI, Orléans	Examinatrice (Président)
Jacek Jagielski	Professor, National Centre for Nuclear Research, Poland	Examinateur
Aurélien Debelle	Maître de Conférences, IJCLab, Orsay	Examinateur
Alain Chartier	Directeur de Recherche, CEA Saclay	Examinateur
Alexandre Boulle	Directeur de Recherche, CNRS, IRCER, Limoges	Examinateur

" $S = k_B ln\Omega$ "

L. Boltzmann

To be continued ...

Acknowledgments

First, I would like to express my gratitude to my two supervisors, Dr. Aurélien Debelle and Dr. Alexandre Boulle, without whom it is not possible to finish this thesis work. My work with Dr. Aurélien Debelle started from my M2 internship in Orsay. Since then, he led me into the field of research, and taught me general knowledge for almost all the techniques or methods which I encountered in my PhD. He is always very kind and patient when we have discussions and when he exams my manuscripts. His enthusiasm inspired me to always keep a positive mindset, which provides an important impetus to overcome challenges. I systematically studied XRD from Dr. Alexandre Boulle in Limoges. I have only stayed there during a relatively short period. But it is amazing that he managed to teach me XRD theories, experiments and computations in a very complete and clear way. I also learned a lot from his computer programs. In addition, both of my supervisors provided me strong support no matter in the scientific field or in other fields, for which I am very grateful.

Special and sincere thanks to my team members. Especially, Prof. Frédérico Garrido and Prof. Lionel Thomé are very friendly and helped me a lot in terms of understanding RBS/C as well as ion/solid interactions. Dee Jay Cerico provided constant help for almost three years.

I would like to thank my collaborators, including Dr. Jean-Paul Crocombette, Dr. Alain Chartier, Dr. Flyura Djurabekova, Prof. Kai Norlund and Dr. Shuo Zhang. Dr. Jean-Paul Crocombette almost participated to all of my thesis work. His help is instrumental for the studies related to RBS/C simulations and radiation effects in Fe. He can always pinpoint important factors. Dr. Alain Chartier provided important data related to the study of radiation effects in UO_2, which is one of the foundations of this thesis work. Dr. Flyura Djurabekova, Prof. Kai Norlund and Dr. Shuo Zhang provided valuable help in terms of RBS/C simulations, which strongly facilitated my work.

I would also like to thank Prof. Jacek Jagielski and Dr. Lech Nowicki for the discussions related to RBS/C simulations.

Many thanks to SCALP facility staff for their assistance, the lab of IJCLab (CSNSM), the PHINIICS and SIMME doctoral schools.

Last but not least, sincere thanks to my families for their remote support.

Contents

List of acronyms **3**

Introduction **5**

1 Particle-solid interactions and radiation effects **9**
1.1 Ion-solid interactions . . . 9
1.1.1 Nuclear energy loss . . . 9
1.1.2 Electronic energy loss . . . 18
1.2 Other particle-solid interactions . . . 21
1.2.1 Neutron irradiations . . . 21
1.2.2 Electron and photon irradiations . . . 23
1.3 Radiation effects . . . 24
1.3.1 Primary radiation damage . . . 25
1.3.2 Defect evolution and other radiation effects . . . 31

2 Characterization techniques **36**
2.1 Rutherford backscattering spectrometry in channeling mode . . . 36
2.1.1 Basic theory . . . 36
2.1.2 Applications . . . 42
2.2 X-ray diffraction . . . 46
2.2.1 Basic theories . . . 46
2.2.2 Applications . . . 50
2.2.3 Simulations . . . 53

3 Simulations of RBS/C spectra of irradiated materials **58**
3.1 MC-RBS/C simulation methods . . . 58
3.1.1 RBSADEC . . . 61
3.2 Improvement of RBS/C simulations . . . 63
3.2.1 Simulations of random spectra . . . 64
3.2.2 Target atomic thermal vibrations . . . 71
3.2.3 Incident ion beam divergence . . . 74
3.2.4 Simulation of aligned spectra . . . 77
3.3 Discussion and summary . . . 80

4 Combination of RBS/C and XRD with molecular dynamics to investigate radiation effects in materials **81**
4.1 Simulation methods: UO_2 . . . 81
4.1.1 Simulation of defects . . . 81

4.1.2 Analysis of defects 83
4.1.3 XRD and RBS/C methods 85
4.2 Characterization of radiation damage: UO_2 88
4.2.1 Strain kinetics 88
4.2.2 Disordering kinetics 92
4.3 Systematic study of model defective systems - Fe as a test-case 98
4.3.1 Description of model defective systems 98
4.3.2 Systematic study of model defective systems: Fe 101
4.4 Summary 119

Conclusions and perspectives **120**

Appendices **123**

A Dechanneling fractions in RBS/C spectra generated from UO_2 MD cells **123**

B Models of the disorder build-up **126**

List of acronyms

1D one-dimensional

2D two-dimensional

3D three-dimensional

arc-dpa athermal recombination corrected displacements per atom

ASD Alternative slowdown

BCA Binary collision approximation

BCC Body-center cubic

BK Brandt-Kitagawa

CDF Cumulative distribution function

CM Center of mass

dpa displacements per atom

DXA Dislocation analysis

DW Debye-Waller

EAM Embedded-atom method

FCC Face-centered cubic

FFP Free flight path

FFT Fast Fourier transform

FMD Freely migrating defect

FP Frenkel pair

FPA Frenkel pair accumulation

GPU Graphical processing unit

HBS High burn-up structure

HEI High energy ion

IBD Ion beam divergence

Lab Laboratory

LEI Low energy ion

LSS Lindhard, Scharff and Schiott

KMC Kinetic Monte Carlo

KP Kinchin and Pease

MC Monte Carlo

MD Molecular dynamics

MSDA Multi-step damage accumulation

NRT Norgett, Robinson and Torrens

NVE Number of particles, volume and energy

PDF Probability density function

PIPS Passivated implanted planar silicon

PKA Primary knock-on atom

PSA Planar scattering approximation

PWR Pressurized water reactor

RBS Rutherford backscattering spectrometry

RBS/C Rutherford backscattering spectrometry in channeling mode

RDA Randomly displaced atom

RE Rate equation

r.l.u reciprocal lattice unit

rms root mean square

RMSD root-mean-square deviation

RSM Reciprocal space map

SHI Swift heavy ions

SIA Self interstitial atom

SP-CSA Single-phase concentrated solid solution alloy

TDDFT Time-dependent density functional theory

TEM Transmission electron microscopy

XRD X-ray diffraction

YSZ Yttria-stabilized zirconia

ZBL Ziegler-Biersack-Littmark

Introduction

For most of human history, apart from light, people's lives are basically free from the radiation effect of energetic particles, despite the fact that these kinds of particles are pervasive in our solar system, e.g., ions in the solar wind. These ions are mainly composed of H and He with trace amount of heavier elements [1], and their average energy is around 1 keV/nucleon [2]. Due to the existence of Earth's magnetosphere, both ions and electrons in the solar wind are deflected away, and thus exert little influence on human society except by making people wondering at some spectacular phenomena induced by them, for example, aurorae [3, 4] and comet tails [5, 6].

However, in the modern society, there is an increasing number of activities involving the use of energetic particles; these later include ions, neutrons, electrons and photons. One important example is the ion irradiation used in several industry and research fields that have benefited greatly from the introduction of foreign atoms and modification of the target atomic structure. Ion implantation can be used for the doping of semiconductor materials, which is one vital step for modern integrated-circuit manufacturing [7, 8] and can have potential applications in novel optoelectronic devices as well [9]. In the field of nanoscience, ion irradiation keeps drawing attention due to the fact that it can be used to change the atomic structure of nanomaterials in a controlled manner [10–12] and to tailor various properties of nanomaterials including mechanical, electrical and magnetic properties [13–15]. In the nuclear industry, in order to effectively predict material behaviors in both fission and fusion nuclear reactors, a considerable amount of effort has been made to emulate reactor irradiation with ion irradiation due to the following advantages of the latter over the former: higher safety and accessibility, faster damage production and lower cost of post-irradiation characterization [16–18]. A last but not the least example of the application of ion irradiation lies in the field of astronomy, where the information related to the concentration of implanted ions and the degree of structure modification can be used to estimate the age or lifetime of the object directly exposed to the bombardment of energetic particles [19–21], and relevant irradiation-induced effects can be critical to some intriguing questions, for example, the possible origin of H_2O on the Moon [22, 23].

Apart from these benefits, the irradiation by energetic particles can often be detrimental to materials when their structures are modified in undesirable ways. This has produced a profound effect on the development of the nuclear materials bearing intense bombardment of particles generated during nuclear reactions. The amount of radiation damage in materials can be quantified by a commonly used parameter called displacements per atom (dpa); a damage level of 1 dpa means that, on average, each atom in the material has been permanently displaced from its original position once. In pressurized water reactors (PWR), which accounted for 66 % of operational reactors worldwide by the end of 2018 [24], the dpa value in in-core structural materials can be as high as 80 dpa [25]. The consequence of the high level of radiation damage is the significant deterioration of material properties. For example, reactor irradiation can degrade the fracture toughness of materials [26], which may result in structure failure under nominal operational conditions; it can also cause dimensional changes due to swelling and creep [27], which is able to hinder the normal operation of reactor components; under harsh environment in nuclear reactors, incidents of intergranular cracking in reactor components have been reported as being due to a complex mechanism called irradiation assisted stress corrosion cracking [28, 29], which poses potential risks on the reactor integrity.

Due to the degradation of materials induced by reactor irradiation, the lifetime of current operational reactors are limited accordingly, and subsequently the economics of nuclear power plants are affected, since capital costs, e.g., construction costs, make up a large part of total nuclear electricity generation costs [30]. Moreover, material behaviors under irradiation are posing great challenges for the safety of generation IV nuclear reactors [31] and future fusion reactors [32]. This is not only due to the higher irradiation dose in some of the more advanced reactors, but also because almost all these advanced reactors will operate in harsher environments as compared to those in current generation II and III reactors [33]. The coupling of intense irradiation with other extreme environments, for example, high temperature, can amplify additional deterioration mechanisms of materials, such as, high temperature helium embrittlement [34, 35].

In addition to the field of nuclear energy, radiation effects can also play deleterious roles in other fields, for example, defect production during ion doping [36], electrical properties degradation of detectors [37], thermoelectric properties degradation of devices in space [38], etc. Therefore, in order to develop materials with excellent irradiation-resistance ability as well as to further explore the usage of particle irradiation, it is crucial to have a comprehensive understanding of the underlying mechanisms of irradiation-induced effects in general, and of defects in particular.

Experimental studies of radiation effects in solid materials date back to the middle of the nineteenth century [39], when sputtering due to glow discharges was observed [40]. Currently, radiation damage is extensively characterized by directly identifying the defects induced by irradiation, using for instance transmission electron microscopy (TEM) [41], and by monitoring phenomenological parameters related to radiation damage levels obtained from techniques including, but not limited to, Rutherford backscattering spectrometry in channeling mode (RBS/C), X-Ray diffraction (XRD), Raman spectroscopy and positron annihilation spectroscopy [42]. In some cases, the phenomenological parameters can be directly used to quantify certain physical changes such as the amorphization process. In some situations, the disorder build-up (disorder versus irradiation dose) obtained from these phenomenological parameters can allow identifying the defects at the origin of the damage, provided that several complementary techniques (with different sensitivity to different defects) are combined.

In parallel with experiments, computational studies have been devoted to simulating the generation and evolution of radiation defects [43]. From atomistic levels, the initial stages of radiation effects, i.e., production of primary damage, can be effectively simulated by molecular dynamics (MD) simulations. However, conventional MD simulations are limited in time scale ($\sim 10^2 - 10^3$ ps) as well as in size scale (depending on computer capacities) [44]. For simulating damage evolution after the stage of primary damage, the tasks have to be delivered to other methods or techniques, e.g., the rate equation (RE) method, Kinetic Monte Carlo (KMC) simulations, etc. Yet, if the thermal migration of defects on large time scale is neglected, conventional MD simulations can still be used to mimic damage evolution induced by high doses irradiation. One method is to simulate overlaps of collision cascades induced by recoils [45, 46]; another one is to directly introduce defects, resulted from the primary damage (e.g. Frenkel pairs (FPs)), into MD cells [47, 48]. In terms of the characterization of radiation effects from simulated targets containing atomic information, numerous computational methods have been developed to identify radiation defects including point defects, dislocations, amorphous clusters, etc [49–51]. Nevertheless, signals from experimental characterization techniques have not yet been extensively produced from such computed targets. For example, the computational method which is able to generate RBS/C signals from MD cells was not developed until recently [52]. Thus, new insights on radiation effects are expected to be obtained from the simulation of the characterization technique signals, if they rely on perfectly known, computationally-generated data.

In this thesis, we will present a work dedicated to studying radiation damage in materials by combining computational and experimental RBS/C and XRD signals. Both techniques are currently used to estimate disorder parameters and the elastic strain (with

XRD only), and have the advantage of generating little or no damage in targets. It is of interest to integrate the computational and experimental approaches by simulating signals recorded during characterization experiments due to the following reasons: (i) the comparison of computational and experimental results can be utilized to evaluate the validity of computational simulations; (ii) it provides an efficient way to establish direct connections between defects and phenomenological parameters, since most experimental characterization techniques do not allow direct observation of defects (except using some often destructive and lengthy methods [53]); such connections are essential for the interpretation of experimental data.

Uranium dioxide (UO_2) is chosen as an example target for this approach. Indeed, as it is the most widely used nuclear reactors fuel, the radiation effects in this material have been extensively investigated, both experimentally and computationally [54], which provides benchmarks for testing our methodology. Besides, UO_2 targets containing various irradiation-induced defects have been recently generated by MD simulations using the FP accumulation method [55], which can serve as input data set for generating RBS/C and XRD signals. The investigation of radiation effects will be focused on the build-ups of disorder and elastic strain in damaged UO_2. In addition, to this specific work, a systematic investigation of Fe targets (each containing one single type of defects created by MD simulations) will also be presented. In the study using Fe targets, we will first give a description of the effect of different types of defects on elastic strain and disorder, and then present the variation of RBS/C signal as a function of He energy and its implication on defect types.

The thesis manuscript is organized into four chapters. In the first chapter, the basic theories of particle-solid interactions and the consecutive potential radiation effects are briefly presented. The second chapter recalls the basic principles of the RBS/C and XRD techniques. The third chapter focuses on the development of a RBS/C simulation program. In the fourth chapter, we first address the RBS/C and XRD simulation results from damaged UO_2 targets and studies on the build-ups of disorder and of elastic strain, and then provide results of the systematic study of Fe targets. Conclusions and perspectives are given at the end.

Chapter 1

Particle-solid interactions and radiation effects

In irradiation processes, both the fate of incident particles and the origin of radiation effects in solid materials are decided by how the particles interacts with target atoms. In this chapter, we will first present the basic theories of particle-solid interactions, with a particular focus on ion-solid interactions. Interactions due to other types of incident particles, including neutrons, electrons and photons, will also be briefly mentioned. Then, we will present how the bombardment of energetic particles gives rise to radiation effects.

1.1 Ion-solid interactions

As an energetic ion penetrates a target, it loses its energy through collisions with target atoms. At least since Bohr's work in the 1940s [56], it is customary to consider the energy loss process by distinguishing elastic collisions with target atoms and interactions with target electrons resulting in atomic excitations or ionizations. The energy loss due to the former mechanism is referred to as nuclear energy loss, and the energy loss due to the latter one is referred to as electronic energy loss. In the following, we shall follow this convention and we will show how to get essential understanding of the rather complex interaction processes which involve numerous variables, mainly based on classical mechanics.

1.1.1 Nuclear energy loss

The information about the nuclear energy loss is obtained by studying the kinematics of elastic collisions [57]. In an elastic collision, normally, only two isolated particles, namely the moving ion and an initially resting target atom, are involved. Fig.1.1(a) depicts such a collision in the laboratory (Lab) reference frame, in which the ion with a mass of M_1 is represented by the black solid circle and the target atom with a mass of

M_2 is represented by the blue solid circle. The black and blue dashed circles represent the initial positions of the ion and atom, respectively.

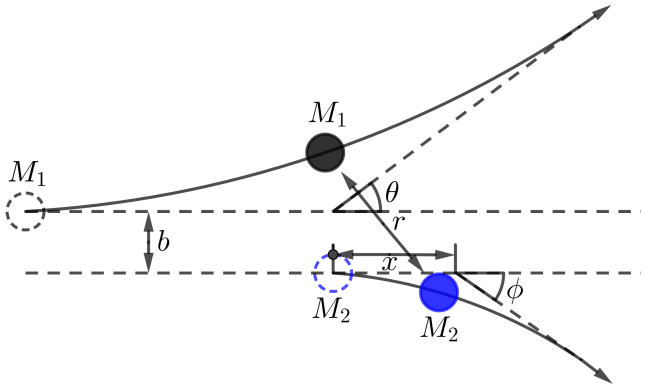

(a) Lab

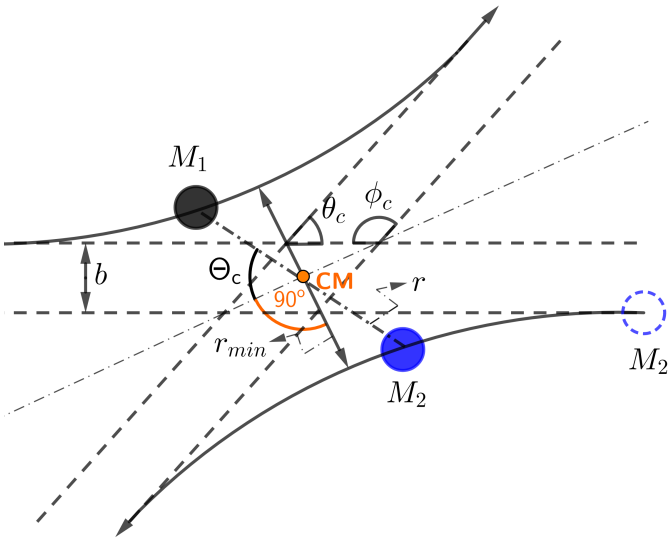

(b) CM

Figure 1.1 – Illustrations of binary collisions in the (a) Lab and (b) CM reference frames. The dashed lines are asymptotic lines of the actual trajectories (solid lines) of the ion (black circle) and atom (blue circle).

Conservations of particles energy and momentum can be expressed by the following

equations:

$$\frac{1}{2}M_1v_0^2 = \frac{1}{2}M_1v_1^2 + \frac{1}{2}M_2v_2^2 \tag{1.1a}$$

$$M_1v_0 = M_1v_1\cos\theta + M_2v_2\cos\phi \tag{1.1b}$$

$$0 = M_1v_1\sin\theta - M_2v_2\sin\phi \tag{1.1c}$$

where v_0 is the initial energy of the ion, v_1 is the ion energy after the collision, v_2 is the atom energy after the collision, θ is the ion scattering angle and ϕ is the atom scattering angle. From Eq.(1.1), we can get the kinematic factor, k, which is the ratio of the scattered energy of ion to the initial energy of ion, E_0:

$$k = \left(\frac{M_1\cos\theta \pm \sqrt{M_2^2 - M_1^2\sin^2\theta}}{M_1 + M_2}\right)^2 \tag{1.2}$$

Eq.(1.2) can be often found useful in Rutherford backscattering experiments, in which the plus sign should be taken, because the term of backscattering indicates $M_1 < M_2$. The energy transferred to the target atom, T, can also be calculated from Eq. (1.1). If the Lab frame can be changed into a center of mass (CM) reference frame as shown in Fig.1.1(b), then the transferred energy T can be expressed in a more concise form which is as follows:

$$T = T_M\sin^2\frac{\theta_c}{2} = \frac{4M_1M_2}{(M_1+M_2)^2}E_0\sin^2\frac{\theta_c}{2} \tag{1.3}$$

where T_M is the maximum transferable energy in a head-on collision, θ_c is the ion scattering angle in the CM system. In Fig.1.1(b), $\theta_c + \phi_c = \pi$, and the center of mass, which is the origin point in the CM frame, is denoted by the orange dot.

While the scattering angles in the equations above are implicitly indicated as known values, this is not the case in most of the conditions. Here we present two popular approaches for calculating the scattering angle and show how its examination leads to the concepts of collision cross section and stopping power. The first approach is to solve the classical scattering integral, and the second one is based on the impulse approximation [1].

Approach of the classical scattering integral

The first method is to calculate the classical scattering integral. In the CM system, the velocity of ion or atom can be decomposed into a radial (towards the origin) and a

[1] The scattering angle can also be calculated analytically using the so-called Magic formula, in which fitting parameters are decided by comparing results with those obtained from the classical scattering integral [58].

transverse component. Thus, the total kinetic energy of the ion and atom reads:

$$E_{KE} = \frac{1}{2}M_1\left[\left(\frac{dr_1}{dt}\right)^2 + r_1^2\left(\frac{d\Theta_c}{dt}\right)^2\right] + \frac{1}{2}M_2\left[\left(\frac{dr_2}{dt}\right)^2 + r_2^2\left(\frac{d\Theta_c}{dt}\right)^2\right] \tag{1.4}$$

in which r_1 is the distance from the ion to the origin, r_2 is the corresponding distance for the atom, and Θ_c is the angle between the line r and the line perpendicular to the shortest line connecting the ion and atom in the collision, r_{min} as give in Fig.1.1(b). By considering the fact that $r_1 + r_2 = r$ and $r_1/r_2 = M_2/M_1$, Eq.(1.4) can be converted to:

$$E_{KE} = \frac{1}{2}M_c\left[\left(\frac{dr}{dt}\right)^2 + r^2\left(\frac{d\Theta_c}{dt}\right)^2\right] \tag{1.5}$$

where M_c equals to $(M_1M_2)/(M_1+M_2)$. From Eq.(1.5), we see that the two-body problem can be replaced by the study of one equivalent particle with the reduced mass as M_c moving about a fixed center of force, which simplifies ensuing calculations. According to the property of the CM system, the total energy in that system, E_c, can be represented by:

$$E_c = E_{KE} + V(r) = \frac{M_2}{M_1 + M_2}E_0 \tag{1.6}$$

where $V(r)$ is the potential energy. Taking into account the energy conservation represented by Eq.(1.6) and the conservation of the angular momentum (which equals to $M_c r^2(d\Theta_c/dt)$), the rate of change of the angle Θ_c over r, $d\Theta_c/dr$, can be obtained, from which the scattering angle is derived as:

$$\theta_c = \pi - 2b\int_{r_{min}}^{\infty}\frac{dr}{r^2[1 - \frac{V(r)}{E_c} - (\frac{b}{r})^2]^{1/2}} \tag{1.7}$$

where b is the impact parameter. Eq.(1.7) indicates that the scattering angle is a function of the impact parameter b, total energy E_c and interatomic potential energy $V(r)$.

The potential used in Rutherford backscattering experiments, i.e., the Coulomb potential, can be expressed by:

$$V(r) = \frac{e^2 Z_1 Z_2}{r} \tag{1.8}$$

where $e^2 = 1.44$ eV·nm [2], Z_1 is the atomic number of the ion and Z_2 is the atomic number of the target atom. Using the Coulomb potential, the scattering angle is calculated as follows:

$$\sin^2\frac{\theta_c}{2} = \frac{\alpha^2}{\alpha^2 + (2E_c b)^2} \tag{1.9}$$

[2]The constant e^2 used in this work is in the cgs unit, in which the Coulomb law constant $1/4(\pi\epsilon_0)$ is equal to 1 where ϵ_0 is the vacuum permittivity

in which $\alpha = Z_1 Z_2 e^2$. While the use of the Coulomb potential can be valid when the interatomic distance is small, in most cases, we need to take into account the screening of the nucleus by its surrounding electrons. Such screening effect can be introduced into the potential calculation by multiplying Eq.(1.8) with a screening function, $\chi(r)$. Depending on the form of the screening function used, Eq.(1.7) may not be able to be solved analytically, in which case numerical evaluations are required. A widely used screening function, namely, the universal screening function, χ_U, was developed by Ziegler, Biersack and Littmark (ZBL), who performed the calculation by fitting the interatomic potentials of 261 atom pairs [59]. The analytical form of χ_U is expressed as follows:

$$\chi_U = 0.1818e^{-3.2x} + 0.5099e^{-0.9423x} + 0.2802e^{-0.4028x} + 0.02817e^{-0.2016x} \tag{1.10}$$

in which the reduced distance, x, is given by $x = r/a_U$, where a_U is the universal screening length defined by:

$$a_U = \frac{0.8854 a_0}{Z_1^{0.23} + Z_2^{0.23}} \tag{1.11}$$

where $a_0 = 0.053$ nm is the Bohr radius of the hydrogen atom. Thus, the universal interatomic potential, V_U, is expressed as:

$$V_U(r) = \frac{e^2 Z_1 Z_2}{r} \chi_U(x) \tag{1.12}$$

Generally, the higher the target atomic number Z_2 is, the stronger the screening effect will be.

Eq.(1.3), Eq.(1.7) and Eq.(1.12) can already provide accurate information for determining the trajectory of a single ion, if electronic collisions are temporarily neglected (which will be discussed in the next subsection). However, it is still interesting to see what kind of collective results, e.g., the stopping power, can appear due to a large number of interactions. For this purpose, we need to firstly evaluate probability-related quantities, namely, the angular and energy transfer cross sections.

The total angular cross section, $\sigma(\theta_c)$, can be represented by an area of πb^2 in the CM system, indicating that if the impact parameter is smaller than b, then the scattering angle of the ion will be greater than θ_c. The differential angular cross section is produced as follows:

$$\frac{d\sigma(\theta_c)}{d\Omega} = \frac{2\pi b db}{2\pi \sin\theta_c d\theta_c} = \frac{b}{\sin\theta_c} \left| \frac{db}{d\theta_c} \right| \tag{1.13}$$

Substituting Eq.(1.9) into Eq.(1.13), we can get the Rutherford differential cross sections

[60] [3]:

$$\frac{d\sigma(\theta_c)}{d\Omega} = \left(\frac{\alpha}{4E_c}\right)^2 \frac{1}{\sin^4(\theta_c/2)} \tag{1.14a}$$

$$\frac{d\sigma(\theta)}{d\Omega'} = \left(\frac{e^2 Z_1 Z_2}{4E_0}\right)^2 \frac{4[(M_2^2 - M_1^2 \sin^2\theta)^{1/2} + M_2 \cos\theta]^2}{M_2 \sin^4\theta (M_2^2 - M_1^2 \sin^2\theta)^{1/2}} \tag{1.14b}$$

where Eq.(1.14a) and Eq.(1.14b) use the notations in the CM and lab frames respectively, $(d\sigma(\theta_c)/d\Omega)d\Omega = (d\sigma(\theta)/d\Omega')d\Omega'$ and $\theta_c = \theta + arcsin(M_1 \sin\theta/M_2)$. In parallel to $\sigma(\theta_c)$, the total energy cross section, $\sigma(E)$, indicates the probability for collisions to occur, where energy transfers are possible, when the ion energy is E. The differential energy transfer cross section can be connected to the angular one through the following equation:

$$\frac{d\sigma(E)}{dT} = \frac{4\pi}{T_M}\frac{d\sigma(\theta_c)}{d\Omega} = \frac{4\pi}{T_M}\frac{b}{\sin\theta_c}\left|\frac{db}{d\theta_c}\right| \tag{1.15}$$

Now, we have almost all the tools to evaluate the stopping power. The average energy loss by the ion in an infinitesimal distance is obtained by multiplying the transferred energy T with the probability of the collision to occur and then integrating over all possible T. Hence, the nuclear stopping power, which is the average energy loss per unit length, is expressed as follows:

$$\frac{dE}{dx}\Big|_n = N \int_0^{T_M} T \frac{d\sigma(E)}{dT} dT \tag{1.16}$$

where N is the target atomic density. Further, the nuclear stopping cross section, S_n, is defined by dividing the nuclear stopping power by N. By converting the integration over T in Eq.(1.16) into that over the impact parameter b, and applying reduced notations [63], S_n is calculated as:

$$S_n(\varepsilon) = \frac{\varepsilon}{a_U^2} \int_0^{\infty} \sin^2\frac{\theta_c}{2} db^2 \tag{1.17}$$

where $\varepsilon = (a_U E_c)/\alpha$ is the reduced energy which equals to the reduced distance a_U divided by the distance of closest approach. Using the scattering integral (Eq.(1.7)), Ziegler *et al* [59] numerically solved Eq.(1.17) and then proposed the following analytical fitting

[3] This result based on classical mechanics happens to be the same with the result derived from quantum mechanics (e.g., based on the Born approximation [61]) except in one condition: If it is impossible to distinguish the particles involved in the interaction, e.g., a collision between two identical particles, a quantum-mechanical correction is needed [62]. However, in practice, if we can consider that the energy distribution of the particles which we are dealing with basically follows the Maxwell-Boltzmann statistics, then they do not act like identical particles, in which case there is no need to invoke the quantum-mechanical correction.

functions:

$$S_n(\varepsilon) = \frac{0.5\ln(1+1.1383\varepsilon)}{\varepsilon + 0.01321\varepsilon^{0.21226} + 0.19593\varepsilon^{0.5}},\ for\ \varepsilon \leqslant 30 \tag{1.18a}$$

$$S_n(\varepsilon) = \frac{\ln(\varepsilon)}{2\varepsilon},\ for\ \varepsilon > 30 \tag{1.18b}$$

in which the first equation uses the universal interatomic potential, and the second one is derived from the Rutherford backscattering [4]. Eq.(1.18) is applied in the widely used ion-solid interaction simulation code, SRIM [64]. As an example (chosen because it mimics an actual RBS/C experiment), the nuclear stopping power of He ions in UO_2 is presented in Fig.1.2, which increases with a higher energy in low energy regions and then decreases after reaching a peak (the electronic stopping powers in the figure will be presented in the following). For compound targets like UO_2, the calculation of stopping powers follows Bragg's rule [65] which states that the stopping power of a compound can be estimated by a weighted sum of the individual stopping powers.

Approach of the impulse approximation

Although accurate results can already be derived from the approach of the classical scattering integral, it is still interesting to present the approach of the impulse approximation due to the following reasons: (i) some methods used in the approach can be applied to calculate electronic stopping powers in the following; (ii) this approach provides a plausible physical reason about why nuclear stopping power decreases at high energy, which may be difficult to contemplate based on the scattering integral; (iii) the results obtained from this approach are still used by some calculation codes, such as DART [66, 67].

The impulse approximation is used to treat small-angle calculations, in which the ratio of the potential energy to the kinetic energy E_c in the CM system remains small through the entire collision process. In this approximation, we shall also only consider the trajectory of the equivalent particle with the mass as a reduced mass M_c as performed in the case of the scattering integral. The initial and final momentum of the particle are $\mathbf{P_1}$ and $\mathbf{P_2}$. The momentum change is $\triangle\mathbf{P} = \mathbf{P_2} - \mathbf{P_1}$. As shown in Fig.1.3, in the limit of

[4] At first glance, the introduction of new notations, i.e., reduced notations, may increase the complexity for understanding the results. However, the use of reduced notations decreases the number of variables, for example, it enables to describe the nuclear stopping for all combinations of ion-atom collisions using a single curve. Thus, it facilitates the comparison of results calculated from different methods, e.g., using different interatomic potentials, and minimizes the necessary data to be stored in relevant simulation codes.

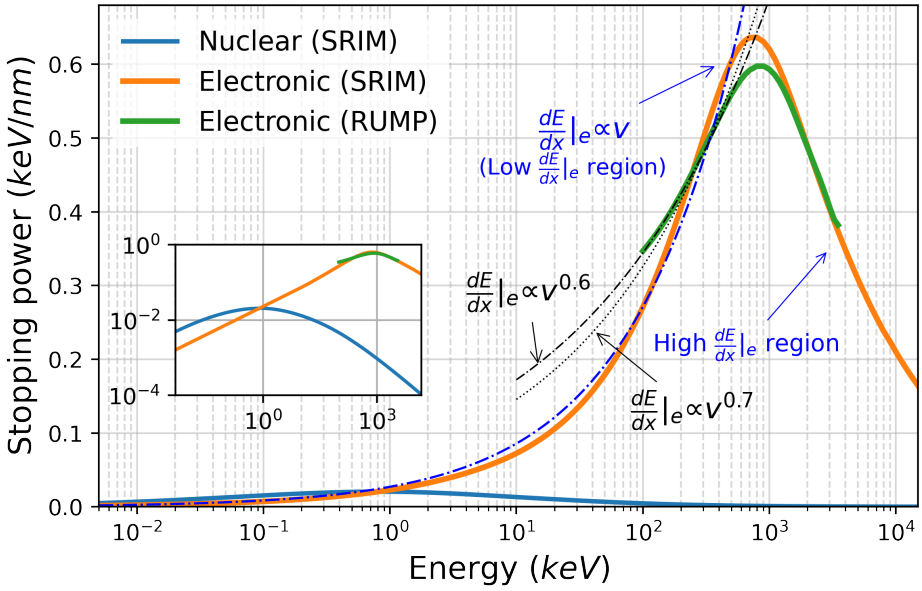

Figure 1.2 – Stopping powers of He ions in UO_2. The nuclear stopping power (blue solid line) is calculated by SRIM. The electronic stopping powers are calculated by SRIM (orange solid line) and RUMP (green solid line). The blue dashed and dotted line is the fit to the SRIM electronic stopping power in the low energy region, where the electronic stopping power increases with energy. Black lines are fits to the RUMP electronic stopping power. The inset shows the stopping powers in a log-log scale.

$\theta_c \ll 1$, the $\triangle\mathbf{P}$ follows following relation:

$$\frac{\triangle \mathbf{p}}{2M_c\mathbf{v}} \cong \frac{\theta_c}{2} \tag{1.19}$$

where $\mathbf{v}$ is the velocity of the equivalent particle. During the entire movement process of the particle, the component of the force acting on it, which is parallel to the incident direction, can be considered being balanced off. Hence, the change in momentum is only induced by the component of the force perpendicular to the incident direction, $\mathbf{F_0}$, which is given by:

$$\triangle \mathbf{P} = \int_{-\infty}^{\infty} \mathbf{F_0} dt = \frac{1}{\mathbf{v}} \int_{-\infty}^{\infty} \mathbf{F_0} dx = \frac{1}{\mathbf{v}} \int_{-\infty}^{\infty} -\frac{dV(r)}{db} dx \tag{1.20}$$

Considering both the Eq.(1.19) and Eq.(1.20), the scattering angle in the impulse approximation can be calculated as:

$$\theta_c = \frac{1}{E_c} \int_b^{\infty} \left(\frac{dV}{dr}\right) \frac{b}{r} \left[1 - \left(\frac{b}{r}\right)^2\right]^{-1/2} dr \tag{1.21}$$

which has the same dependency on variables as Eq.(1.7).

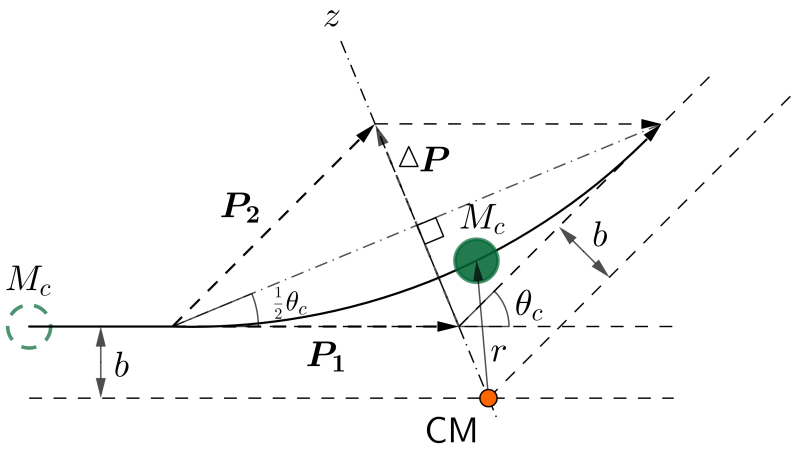

Figure 1.3 – Illustrations of the trajectory of the equivalent particle with the mass as M_c.

Originally, the impulse approximation was meant for small-angle collisions. In order to apply the approximation in a more general condition, Lindhard *et al* [68] extrapolated the treatment to wide-angle collisions by replacing θ_c with $2\sin(\theta_c/2)$ and replacing b^2 with $b^2 + b_0^2$, in which b_0^2 is an arbitrary constant. Then, using reduced notations, a universal one-parameter differential scattering cross section can be expressed as:

$$d\sigma = \frac{-\pi a^2}{2} \frac{f(t^{1/2})}{t^{3/2}} dt \tag{1.22}$$

where a is a screening distance, $f(t^{1/2})$ is a function depending on the assumed form of the screening function [69], and t is a dimensionless collision parameter defined by:

$$t = \varepsilon^2 \frac{T}{T_M} = \varepsilon^2 \sin^2 \frac{\theta_c}{2} \tag{1.23}$$

It can be found that t is a measure of the depth of penetration into the atom during a collision. Combining Eq.(1.16) and Eq.(1.23), the reduced nuclear stopping cross section can be given in a simple form:

$$S_n(\varepsilon) = \frac{1}{\varepsilon} \int_0^{\varepsilon} f(t^{1/2}) dt^{1/2} \tag{1.24}$$

Using this approximation, the stopping powers calculated from different interatomic potentials [5], including the universal interatomic potential, can be calculated by adjusting fitting parameters or forms of the function $f(t^{1/2})$ [70]. In addition, Eq.(1.20) indicates that the momentum change is related to the interaction time and thus related to the

[5] The potentials, which can be used in both the scattering integral and impulse approximation, should be spherically symmetrical.

particle velocity. It is possible that if the velocity is higher than a certain value, the momentum change can be decreased due to shorter interaction time, which could be the reason for the decrease of the nuclear stopping power with a high incident energy.

1.1.2 Electronic energy loss

It is claimed that the subject was originally addressed by J. J. Thomson before the discovery of the atomic nucleus at the beginning of the last century [56, 71]. In contrast to the description of the nuclear energy loss, there is a lack of a single theoretical model which can accurately describe the electronic energy loss in a broad energy range mainly based on classical mechanics. The time-dependent density functional theory (TDDFT) method may provide the solution based on the first principles [72, 73]. However, it is not in the scope of this thesis to describe the TDDFT method. In the following, we will show the mechanisms of the electronic stopping suitable for ions with low and high energies (or velocities), respectively [57], which is followed by a brief presentation of the empirical method used in SRIM.

Ions with low energies

The ions with low energies refer to the ions with velocity v smaller than $v_0 Z_1^{2/3}$, where $v_0 = 2.188 \times 10^8$ cm/s is the Bohr velocity. Qualitatively, for $v < v_0 Z_1^{2/3}$, the ion is not fully stripped of its electrons [74] and tends to neutralize by capturing electrons in target atoms. J. Lindhard, M. Scharff and H. Schiott (LSS) [63, 75] proposed that the electronic stopping power in this low energy region can be calculated as:

$$\left.\frac{dE}{dx}\right|_e = \xi_L 8\pi e^2 a_0 N \frac{Z_1 Z_2}{(Z_1^{2/3} + Z_2^{2/3})^{3/2}} \left(\frac{v}{v_0}\right) \tag{1.25}$$

where the correction factor $\xi_L \cong Z_1^{1/6}$. It can be found that the electronic stopping power is proportional to v.

It was shown that this Lindhard form for electronic stopping can be explained by the Firsov model [57, 76]. In the Firsov model [77], because of the low ion velocity, the collision time between the ion and atom, which are represented by Thomas-Fermi atoms, is long enough for a fusion of the ion and atom into a quasi-molecule to occur. During the lifetime of this quasi-molecule, the electrons of both the ion and atom are able to exchange. When an electron in the atom is captured by the ion, the ion loses a small amount of momentum proportional to $m_e v$, in which m_e is the mass of the electron. Thus, by examining the electron flux through the so-called Firsov plane dividing the ion and atom in the quasi-molecule, the energy loss to electrons per collision with one atom is

given by:

$$T_e = \frac{0.35(Z_1+Z_2)^{5/3}\hbar/a_0}{[1+0.16(Z_1+Z_2)^{1/3}b/a_0]^5}v \tag{1.26}$$

where $\hbar$ is the reduced Planck constant. Since the energy transfer T_e is impact parameter b dependent, by inserting Eq.(1.26) into Eq.(1.16) and performing integration on b, one can get the electronic stopping power which exhibits a similar form to that of the Lindhard one. The main difference between the two models comes from the different interatomic potentials used.

Ions with high energies

If the ion velocity is larger than $v_0 Z_1^{2/3}$, the ion can be considered as a bare nucleus, and its interactions with (supposedly free) target electrons can be accurately described by a pure Coulomb interatomic potential. Although the term of electronic stopping is often connected with inelastic collisions, interactions in the high energy region can be treated by an elastic approach introduced previously, i.e., the impulse approximation.

Inserting the Coulomb potential to Eq.(1.20), the energy transferred to an electron in a collision is given by:

$$T_e = \frac{\triangle p^2}{2m_e} = \frac{2Z_1^2e^4}{b^2m_ev^2} \tag{1.27}$$

Once again, according to Eq.(1.16), the electronic stopping power can be obtained as follows:

$$\frac{dE}{dx}\Big|_e = n_e\int_{b_{min}}^{b_{max}} T_e 2\pi b db = \frac{4\pi Z_1^2e^4n_e}{m_ev^2}\ln\frac{b_{max}}{b_{min}} \tag{1.28}$$

In Eq.(1.28), the minimum impact parameter b_{min} is related to the maximum transferred energy T_{max} according to Eq.(1.27). Since $m_e \ll M_1$, T_{max} can be represented by $2m_ev^2$, and the b_{min} is derived as:

$$b_{min} = \frac{Z_1e^2}{m_ev^2} \tag{1.29}$$

The maximum impact parameter b_{max} is related to the minimum transferred energy, T_{min}, which a target-atom electron can accept. T_{min} can be represented by the average excitation energy of an electron, I. Hence, b_{max} is derived as:

$$b_{max} = \frac{2Z_1e^2}{(2m_ev^2I)^{1/2}} \tag{1.30}$$

Substituting Eq.(1.29) and Eq.(1.30) into Eq.(1.28), and considering a correction due to distant resonant energy transfer, the electronic stopping power can be expressed as:

$$\frac{dE}{dx}\Big|_e = \frac{2\pi Z_1^2e^4}{E_0}NZ_2\left(\frac{M_1}{M_e}\right)\ln\frac{2m_ev^2}{I} \tag{1.31}$$

The average excitation energy I, in eV, for most elements is roughly $10Z_2$ [57].

It can be found that, in the high energy region, the electronic stopping power is inversely proportional to v^2 (or E_0), which exhibits an opposite trend compared to the stopping power in the low energy region. After taking into account the corrections for relativistic terms and for the non-participation of the strongly bound inner shell electrons, Eq.(1.31) can be transformed into the Bethe formula.

Empirical approach

In order to accurately describe the electronic stopping powers of ions in both the low and high energy regions, empirical approaches, for example, the one used in SRIM, can be applied. Ziegler *et al* [59] collected a data base of H electronic stopping cross sections, S_H, from experimental measurements of both H and He ions in solids. Then, the electronic stopping cross sections for heavy ions, S_{HI}, can be obtained from S_H at the same velocity using the scaling rule [78]:

$$S_{HI} = S_H(Z^*_{HI})^2 = S_H Z^2_{HI}\gamma^2 \tag{1.32}$$

where Z_{HI} is the atomic number of the heavy ion, $Z^*_{HI} = Z_{HI}\gamma$ is the effective charge of the heavy ion, and γ is its fractional effective charge obtained based on the Brandt-Kitagawa (BK) theory [79].

An example of an electronic stopping power calculated from SRIM, i.e., the stopping power of He ions in UO_2, is shown in Fig.1.2. Compared to the nuclear stopping power, the electronic stopping power dominates the total stopping when the ion energy is high. In addition, there are also other available stopping data, for example, the data used in the RUMP code [80]. Fig.1.2 also shows the electronic stopping power calculated from RUMP in the energy range of 100 keV to 3.5 MeV which corresponds to the lower cutoff and upper fit energies in that code [81]. It is found that the RUMP data provides more accurate descriptions of the electronic stopping power of He ions in UO_2 based on RBS experiments. One reason is that there may be anomalously lower energy loss to materials with a band gap due to fewer energy excitation levels available, and experimental data indicates that the electronic stopping power is proportional to $v^{0.7}$ instead of v in Si and Ge in the low energy region [59]. Indeed, according to the least square fit, Fig.1.2 shows that the RUMP stopping power is proportional to $v^{0.6}$ in the energy range of 100 keV to 250 keV (corresponding to the velocity of $v_0 Z_1^{2/3}$), which is close to that of Si and Ge. In contrast, the electronic stopping power calculated by SRIM is roughly proportional to v in the low energy region, where the electronic stopping power increases with the He energy.

1.2 Other particle-solid interactions

Apart from ion irradiations, neutron, electron and photon irradiations can often be found in harsh environments, such as nuclear reactors. Thus, it is pertinent to briefly discuss their interactions with solid materials. Some insights on these interactions can be readily obtained by applying the methods used to treat ion-solid interactions.

1.2.1 Neutron irradiations

Since neutrons have no electric charge, they can directly interact with target nuclei. Among various types of interactions with nuclei, the elastic scattering, i.e., the (n, n) reaction, is one of the major sources of radiation damage found in reactor structural materials. If the classical mechanics depicted in Sec.1.1.1 are applied to treat such an elastic scattering, the Coulomb potential needs to be changed to a hard-sphere potential:

$$V(r) = \begin{cases} \infty & , r \leqslant R \\ 0 & , r > R \end{cases} \tag{1.33}$$

where the parameter R represents the sum of the neutron and the nucleus radii, which is also equal to the distance of closest approach, r_{min}. Since the same energy and momentum conservation laws can be used, the transferred energy T is still given by Eq.(1.3). The relation between the impact parameter b and the scattering angle θ_c is represented by:

$$b = r_{min} \cos \frac{\theta_c}{2} \tag{1.34}$$

Inserting Eq.(1.34) into Eq.(1.13), the angular differential cross section is obtained as:

$$\frac{d\sigma(\theta_c)}{d\Omega} = \frac{r_{min}^2}{4} \tag{1.35}$$

And the energy transfer differential cross section can be generated by using Eq.(1.15):

$$d\sigma(E) = \frac{\pi r_{min}^2}{T_M} dT \tag{1.36}$$

From these new equations obtained by using the hard-sphere potential, we can find distinct differences between the neutron and ion irradiations:

1. The angular distribution of scattered neutrons is isotropic [6], and the probability of energy transfer is constant over the range 0 to T_M. In contrast, small-angle

[6] Actually, with the increase of neutron energy (> 1 MeV), the scattering becomes more forward [82]. More accurate calculations can be performed using the optical model for nuclear scattering [83].

scatterings are dominant in ion-solid interactions. Therefore, the spectrum of the transferred energy from neutron irradiations due to elastic collisions is harder than that from ion irradiations [7];

2. By integrating Eq.(1.35), the total neutron elastic scattering cross section can be calculated as πr_{min}^2. Then, we can estimate that the mean free path between two collisions, $1/(N\pi r_{min}^2)$, is on the order of magnitude of 0.1 m, which is way larger than the typical range($\sim \mu m$) in ion irradiation processes.

In terms of other reactions, for example in radiative captures, i.e., (n, γ) reactions, the energy T from the emission of a single γ photon of energy E_γ ($E_\gamma < Q$, where Q is the energy released from nuclear reactions) is given by [82]:

$$T = \frac{E_\gamma^2}{2M_d c^2} \tag{1.37}$$

where M_d is the mass of the daughter nucleus (recoil nucleus). In general, (n, γ) reactions lead to rather small T since the photon cannot carry away very much momentum [84]. In addition to radiative captures, nuclear fissions could be interesting reactions to mention, since UO_2 is used as an example material in this thesis. Usually, the fission reaction can be represented by:

$$^{235}U + n \rightarrow {}^{236}U^* \rightarrow {}^{A_{d1}}X_{d1} + {}^{A_{d2}}X_{d2} + 2.42n + Q \tag{1.38}$$

where ^{236}U is on the excited state, 2.42 is the average number of prompt neutrons generated [8], X_{d1} and X_{d2} are two daughter nuclei with their mass numbers as A_{d1} and A_{d2}, respectively. The daughter nuclei are not determined uniquely, and they usually consist of one light and one heavy nuclei with the most probable mass numbers as 95 and 140, respectively. The average Q released from the fission is around 200 MeV, and roughly 80 % of the fission energy becomes kinetic energy of the daughter nuclei. The most probable T to the light and heavy daughter nuclei are 98 MeV and 66 MeV, respectively, which will be further transferred to target atoms through ion-solid interactions. The remaining energy is shared by neutrons, γ rays, β and γ decays of daughter nuclei [85].

Generally, neutron reactions can be quite complex. In practice, for example, in representative neutron transportation codes, e.g., the MCNP [86] and TRIPOLI [87] codes, detailed data like reaction cross sections are extracted from nuclear data libraries, such as the ENDF/B library [88].

[7] A harder spectrum indicates that there are more neutrons or ions in high energy regions.

[8] The prompt neutrons are emitted at the instant of fission (within 10^{-16} s), which is in contrast to delayed neutrons emitted following the β decay of the fission fragments.

1.2.2 Electron and photon irradiations

In electron irradiations, both elastic collisions with target atoms and inelastic scatterings can take place. In Sec.1.1.2, we already mentioned the collision of an electron at rest with an ion of high velocity. However, if we want to study the interaction in a reciprocal way, i.e., the interaction of a moving electron with an atom at rest, there will be noticeable differences mainly due to the very small mass of an electron compared to that of an ion:

1. In many electron irradiation conditions, the relativistic effect may not be negligible (for example, when the electron energy is 100 keV, it already has a speed of $0.55c$). In these conditions, the transferred energy in elastic collisions can still be described by $T = T_M \sin^2(\theta_c/2)$, but T_M must be adjusted to:

$$T_M = \frac{2E_e(E_e + 2m_e c^2)}{M_2 c^2} \tag{1.39}$$

   where E_e is the electron kinetic energy, m_e and M_2 are rest masses of electrons and target atoms, respectively [89].

2. Accelerated charged particles can give rise to bremsstrahlung. Compared to ions, electrons are significantly affected by such radiative process of energy loss at much lower energy. Therefore, when the electron energy is high, the stopping power is contributed by collisions as well as by the energy loss due to bremsstrahlung. The critical energy at which the two stopping terms are equal can be obtained as follows[90]:

$$E_c \approx \frac{1600 m_e c^2}{Z_2} \tag{1.40}$$

   It can be found that E_c decreases with a higher Z_2. Hence, high Z materials are not preferred in shielding β radiations.

For photon irradiations, we mainly refer to X-rays or γ-rays radiations. These photons interact with solids mainly through three processes, which leads to the emission or generation of electrons:

1. Photons can transfer their energy, E_p, to electrons in the vicinity of an atom through the photoelectric effect. In this process, the kinetic energy received by the so-called photoelectron, T_e, is given by:

$$T_e = E_p - E_b \tag{1.41}$$

   where E_b is the binding energy of the electron. In the filling process of the vacancy left by the photoelectron, additional energy can be released, which can further induce the emission of either characteristic X-ray photons or Auger electrons.

2. The photon can inelastically scatter with a (free) electron by Compton scattering, after which the wavelength of the scattered photon becomes larger. By applying relativistic kinematics and conservation of total energy and of momentum, the scattered photon energy is given by [91]:

$$E'_p = \frac{E_p}{1 + (E_p/m_e c^2)(1 - \cos\theta)} \tag{1.42}$$

   Then, the kinetic energy of the scattered electrons is calculated as $T_e = E_p - E'_p$.

3. If a photon is in the vicinity of an atom, the photon with its entire energy can be converted into an electron-positron pair by pair productions. There exists an energy threshold of 1.022 MeV for this process. Following the annihilation of the positron, two photons, each with an energy of 0.511 MeV, are created, which may further interact through the photoelectrical process or Compton scattering [83].

In addition, photons can also experience elastic scattering with free electrons through Thomson scattering, in which the wavelength of the photons does not change. Although this process generates little effect on targets, it is the basis for one of the methods used to characterize radiation damage in this thesis, i.e., the XRD method. Following classical theories, if an unpolarized beam with the intensity as I_0 is scattered by a single free electron, the intensity of the scattered beam, I, can be calculated by the Thomson scattering equation:

$$I = I_0 \frac{e^4}{m_e^2 c^4 R^2} \left(\frac{1 + \cos^2\phi_T}{2} \right) \tag{1.43}$$

where the I is measured at a distance R from the electron at an angle ϕ_T with the incident beam direction and the last term, $(1 + \cos^2\phi_T)/2$, is the polarization factor[92].

1.3 Radiation effects

Radiation effects basically stem from the change of target atomic structures. In elastic collisions, the energy transferred from incident particles provides the impetus for displacing target atoms. The displaced atoms may form stable defects which can undergo evolutions as a function of time and projectile particle fluence. As a direct result of particle-solid interactions, the generation of stable defects from displaced atoms is referred to as the primary radiation damage. In this section, we will present basic mechanisms related to primary radiation damage, which is followed by the description of defect evolution. Other effects due to the introduction of foreign atoms and electronic stopping, which are mainly found in ion-solid interactions, will be mentioned at the end of the section.

1.3.1 Primary radiation damage

In the framework of elastic collisions, a target atom can be permanently displaced from its original position if the transferred energy T is larger than the threshold displacement energy, E_d. Typical values of E_d, depending on materials, vary from 20 to 100 eV [93]. In the process of irradiation, the target atom permanently displaced by a projectile particle is called the primary knock-on atom (PKA). Displaced atoms (or recoils) including PKAs can in turn displace other atoms, by which way a collision cascade is formed. Fig.1.4 shows an example of collision cascades created by 4 MeV Au ions in MgO according to SRIM simulations. Collision cascades containing less than 200 recoils are represented by grey spheres, and those having more than 200 recoils are represented by other colors. Fig.1.4 indicates that an energetic particle can generate numerous collision cascades with dendritic shapes, in which a large branch can have small sub-branches, resembling a fractal structure. In terms of radiation damage, the number of displacements in all the collision cascades has drawn particular attention shortly after the advent of nuclear reactors in the 1940s [94], and various methods for calculating this value have been proposed.

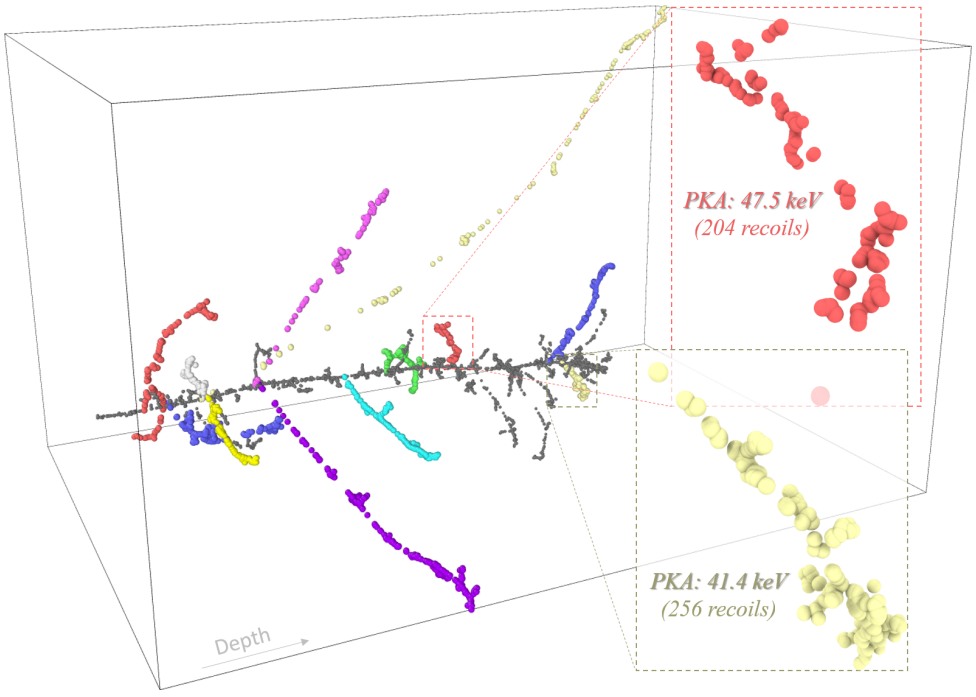

Figure 1.4 – Collision cascades created by 4 MeV Au ions in MgO simulated by SRIM using the full damage cascades mode. The grey spheres indicate the collision positions involved in collision cascades in which the total number of recoils is less than 200. For collision cascades containing more than 200 recoils, the collision positions are indicated by other colors. (Insets show a collision cascade induced by a PKA with 47.5 keV energy and another one induced by a PKA with 41.4 keV energy. $E_d(Mg) = E_d(O) = 60$ eV [93]).

Calculation of displacements

Before an accurate picture of stopping power was established, the well-known analytical model for estimating the average number of displacements, $< N_d(E) >$, produced by a projectile with an energy E, was proposed by Kinchin and Pease (KP) in the 1950s [95]. Based on binary elastic collisions between like atoms and using a hard sphere interatomic potential, $< N_d(E) >$ can be calculated as follows:

$$< N_d(E) >= \begin{cases} 0, & if\ E < E_d \\ 1, & if\ E_d \leqslant E < 2E_d \\ E/2E_d, & if\ 2E_d \leqslant E < E_{KP} \\ E_{KP}/2E_d, & if\ E \geqslant E_{KP} \end{cases} \tag{1.44}$$

where E_{KP} is an energy limit depending on the properties of both projectile and target atoms, above which all the energy is lost in inelastic interactions, and below which the electronic energy loss is neglected. It has been shown that this form of function can be reached based on different arguments. One method is to firstly assume a conservation of displacement:

$$< N_d(E) >=< N_d(E-T) > + < N_d(T) > \tag{1.45}$$

in which $< N_d(T) >$ is the average displacements induced by recoils with an energy T, and $< N_d(E-T) >$ is the average displacements created by the scattered projectile. Then, the $< N_d(E) >$ in the KP model can be obtained from the following integral equation:

$$< N_d(E) >= \int_0^T [< N_d(E-T) > + < N_d(T) >] P(E,T) dT \tag{1.46}$$

where $P(E,T)$ is the probability density of transferring energy T. For elastic collisions using a hard sphere potential, the probability density just equals to $(1/E)$.

The KP model exhibits a quality of conciseness, but it suffers from non-negligible discrepancies with experimental results. Therefore, two important improvements of the KP model have been made:

1. The hard sphere potential was replaced by a more realistic one, that is, a potential varying as an inverse power of the transferred energy T [96]. This improvement can be represented by multiplying the original equation with a constant ξ, which is smaller than 1. It is because a more realistic potential prefers forward-scattering ($T \ll E$), which leads to a higher portion of energy spent in subthreshold collisions than hard-sphere scattering [97]. Both analytical theory and computer simulations suggest ξ near 0.8 [98].

2. The energy E can be replaced by the so-called damage energy, $\nu(E)$, which is the amount of PKA energy not given to electrons. For collisions between like atoms ($Z_1 = Z_2$), Lindhard *et al.* [99] proposed the damage energy as follow:

$$\nu(E) = \frac{E}{1 + kg(\varepsilon)} \tag{1.47}$$

where k is related to the Lindhard electronic stopping cross section, $g(\varepsilon)$ is a function of the reduced energy ε (The exact expressions of k, ε and $g(\varepsilon)$ can be found from relevant literatures [57]).

Applying above improvements, we can get $< N_d(E) >$ from the so-called modified KP model or the Norgett, Robinson and Torrens (NRT) model:

$$< N_d(E) >= \begin{cases} 0, & if\ E < E_d \\ 1, & if\ E_d \leqslant E < 2.5E_d \\ \frac{0.8\nu(E)}{2E_d} & if\ 2.5E_d \leqslant E < \infty \end{cases} \tag{1.48}$$

Alternatively, $< N_d(E) >$ can be obtained from binary collision approximation (BCA) simulations, which is argued to be more "correct" than using the analytical models [9] due to the following reasons: (i) the BCA simulations can take into account the collisions between different atoms ($Z_1 \neq Z_2, M_1 \neq M_2$); (ii) more accurate electronic stopping powers can be used in the simulations, like the one used in SRIM. However, the stochastic treatment applied in the BCA simulations cannot relieve the situation encountered by the analytical models. In general, the dpa calculated with the NRT model (dpa can be obtained by dividing the displacement number by the total number of target atoms in the damaged region), for example, in metals, tends to overestimate the number of stable defects by a factor of 3 to 4 [100].

The salvation has long been considered to be the integration of the recombination effects. Based on the BCA simulations, Robinson and Torrens proposed a vacancy capture radius, r_v. Only when the distance between the target atom original location and its rest location after the collision is larger than r_v, a stable defect forms. Thus, $< N_d(E) >$ can decrease by increasing r_v [101]. Recently, Nordlund *et al.* [100] proposed a modified, more sophisticated disorder parameter, based on the dpa definition, that is called athermal recombination corrected dpa (or arc-dpa). In this description, a defect surviving fraction, $\xi_{survive}$, is multiplied with $< N_d(E) >$ calculated by the NRT model. Their argument is similar to that of Robinson, which states that only defects far from the cascade center

[9] It is more correct in terms of the physical treatment, but the discrepancy with experimental values could be larger.

can survive. Fitting parameters in $\xi_{survive}$ need to be determined from MD simulations or experiments. Since the $< N_d(E) >$ value depends on the method used, it has been appealed that when the displacement value is reported, the method used to estimate it should be clearly stated [102, 103].

In general, the NRT model or the approach based on the BCA simulations are of importance credited to their broad adoptions in various materials. However, the whole process of recombination cannot be embedded in, and the term "displacement" conceals the various nature of the generated defects. Therefore, an alternative description is needed to better understand the generation of primary radiation damage.

Cascade evolutions

Generally, the stage of primary radiation damage lasts around 10 ps [104], which is too short to be observed experimentally. On the contrary, the cascade phenomenon can be caught by MD simulations. The cascade development can be separated into the collision phase and the thermal spike (or heat spike, or displacement spike [105]) phase [106] [10]. In the collision phase, the PKA energy is distributed among atoms through collisions, which creates highly disordered regions. The number of displacements increases sharply until a maximum displacement is reached, which occurs in around 0.1 to 1 ps, depending on the PKA energy. In the thermal spike phase, the PKA energy shared among numerous atoms is dissipated through lattice vibrations. At the beginning of this second phase, the density of deposited energy in the disordered region is so high that local melting can occur [107]. Then, the thermal spike undergoes a quick cooling down period, which can be considered as a recrystallization process of hot liquid. During this recrystallization (or recombination) process, the majority of displaced atoms return to regular lattice sites. When the disordered region regains thermal equilibrium with the bulk at the end of thermal spike, only a fraction of displacements survive, which constitutes stable defects. In general, the number of stable defects, N_d^{MD}, is smaller than the number of displacements calculated by the NRT model, N_d^{NRT}, and the ratio of N_d^{MD} to N_d^{NRT} decreases with energy until the onset of subcascade formation [104] [11].

As an example, Fig.1.5 shows the development of a collision cascade induced by a 2.46 keV Si PKA in 3C-SiC at 300 K, according to a MD simulation. The simulation was performed with a $30a \times 30a \times 30a$ SiC cell containing 216000 atoms using the LAMMPS code [109, 110] (a is the lattice parameter of 3C-SiC). The Tersoff/ZBL style potential [111]

[10] Note that there is a different meaning for the term of "thermal spike" when it is used in case of irradiation with high energy ions, in which the ion energy is mainly dissipated by electronic excitations.

[11] Recently, it is found that the ratio of N_d^{MD} to N_d^{NRT} in alloys could continue to decrease even after the subcascade formation, when the PKA is a light constituent atom in the alloy [108].

was used to describe the interactions between atoms, and periodic boundary conditions were applied in all directions. The number of particles, volume and energy (NVE, a microcanonical ensemble) in the cell were kept constant. A kinetic energy of 2.46 keV was imparted to a Si atom in the bulk region to initiate the collision cascade. In order to prevent shock waves or thermal energies re-entering the cell through periodic boundaries, the velocities of atoms in the boundary layers, with a width of $2a$, are scaled to that corresponding to 300 K [12]. In Fig.1.5.(a-f), the vacancy and interstitial pairs as well as antisites were analyzed with the Wigner-Seitz cell method using the OVITO software [112]; in Fig.1.5.(g-h), the potential energy of each atom was calculated by the LAMMPS code. The simulation shows that the number of vacancy and interstitial pairs reaches a maximum, which is 67, at around 0.1 ps, and then starts to decrease. The number of antisites exhibits a similar trend, but with a longer time to reach the maximum. After around 1 ps, the total number of defects becomes stable; compared to the maximum number, 54 % of vacancy and interstitial pairs survive from recombinations, which become stable Frenkel pairs; the dominant defects are Frenkel pairs and the rest are antisites. Both the figures of defects and plots of potentials indicate that there seem to be the formation of subcascades.

The displacements surviving the recrystallization process can have various types. Some defects and the associated formation mechanisms are described hereafter:

- Frenkel pairs: A Frenkel pair is formed if a vacancy and an associated interstitial are separated by a minimum distance that prevents their recombination [113]. In the MD simulations of collision cascades in Cu [107], it is found that only interstitials escaping from melted regions can survive. With a higher PKA energy, the melted region will be larger, and the survived fraction can be smaller. Therefore, the ratio of N_d^{MD} to N_d^{NRT} tends to decrease with a higher PKA energy, until the formation of subcascades.

- Vacancy clusters: Vacancies left in a melted region can be pushed towards the center region by the recrystallization front, as shown in MD simulations performed in Co/Cu bilayer cells [114]. Thus, vacancies are able to meet and form clusters [12].

- Interstitial clusters: In a collision cascade, if the melted region has an elongated shape, the recombination of excess interstitials in the tip and vacancies in the center can be prevented by the recrystallization occurring between the tip and the center, which traps the excess interstitials and generates clusters. Such mechanism is called the "liquid-isolation" mechanism, which is observed in Pt [115]. There is

[12]Note that large vacancy clusters are called voids, and bubbles when they are filled with gas atoms.

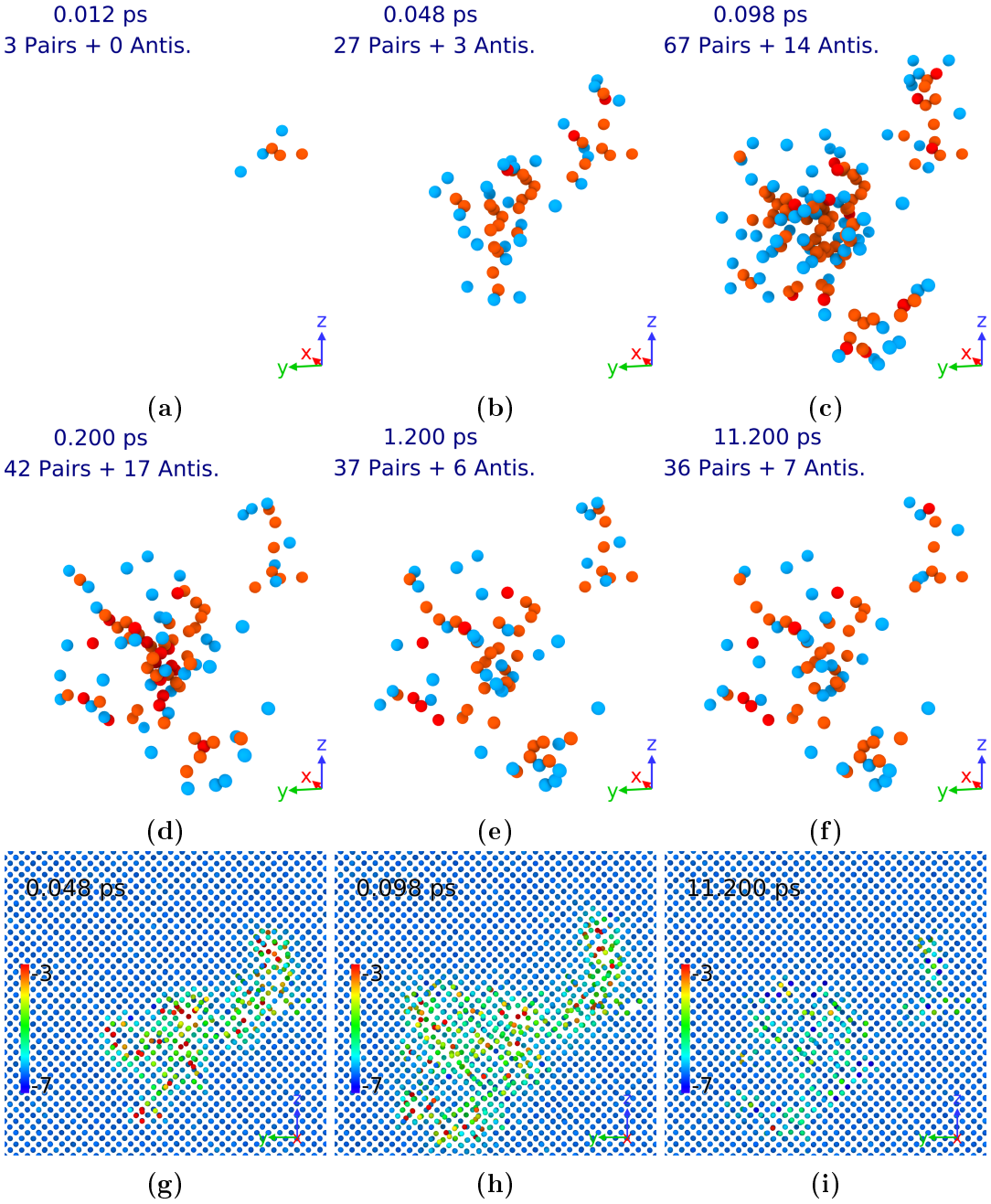

Figure 1.5 – Collision cascade in 3C-SiC induced by 2.46 keV Si PKA. (a)-(f) show interstitial (blue) and vacancy (orange) pairs, and antisites (red) at 0.012, 0.048, 0.098, 0.200, 1.200 and 11.200 ps respectively. (g)-(i) show atoms in a layer, with the width as $2a$ (a is the lattice parameter), affected by the collision cascade at 0.048, 0.098 and 11.200 ps respectively, in which the potential energy of each atom is presented by the color bar legend ranging from -7 eV to -3 eV.

also another mechanism proposed for the formation of large clusters, which is due to the interaction of shock waves [116].

- Dislocation loops: Both interstitial-type and vacancy-type dislocation loops are

found in high-energy collision cascades, for example, cascades induced in W [117] and Fe [118]. It can be argued that if the total kinetic energy imparted to clusters is high enough, there is a possibility for the formation of dislocation loops due to the collapse of clusters.

- Amorphous clusters: The formation of amorphous clusters are observed in semiconductors, e.g., Si and Ge [115]. The reason is attributed to the relatively weaker defect annealing in semiconductors compared to that in metals, due to different types of bonds [119].

1.3.2 Defect evolution and other radiation effects

Defect evolution

After primary damage events are formed, in the time scale of ~ 10 ps, mobile defects can diffuse and interact with each other and/or with other defects, which eventually decides the form of the radiation defects observed experimentally [13]. For example, both vacancies and/or self interstitial atoms (SIAs) are highly mobile at temperatures of practical interest [121]. Vacancies and interstitials can annihilate upon meeting each other, or they can be absorbed by defect sinks, such as dislocations, voids, free surfaces, etc. Such diffusion is usually accomplished by the interchange between atoms and neighboring point defects in a random way, and the diffusion coefficient, D, of a target atom is described as follows:

$$D = f_v D_v C_v + f_i D_i C_i + f_{2v} D_{2v} C_{2v} + \cdots \tag{1.49}$$

where f is a correlation factor close to unity, C is the defect concentration, the subscripts v, i and $2v$ represent vacancy, interstitial and di-vacancy, respectively. Since irradiation can introduce point defects whose concentrations are much larger than the thermal equilibrium concentrations, D can be increased by irradiation. As a result, the diffusion is enhanced by radiation [122]. In general, the timescale of defect evolution due to diffusion exceeds the one that can be handled by MD simulations. The task of handling such defect evolution can be tackled by using methods like RE or KMC, as mentioned in the introduction part. The diffusion of defects could play a crucial role in the accumulation of damage. For example, simulations based on the RE method reveal that, when the temperature is increased, an asymmetry in the vacancy and interstitial migration energies leads to a delayed damage accumulation, as observed in MgO, in contrast to c-ZrO_2 for which both migration energies are similar and the disordering process is accelerated [123].

[13] If the defect mobility is strongly limited, it seems that primary defects can also be directly observed in dedicated experiments, such as in the experiment of self-ion irradiation of W at cryogenic temperature [120].

As defects interact with each other, new types of defects can be generated through processes which often appear to be driven by the search for a system-energy minimization. For example, large clusters of interstitials tend to form dislocation loops, by which way the energy per interstitial is decreased [124]; in face-centered cubic (FCC) systems, e.g., CeO_2 and UO_2 (where the cation sublattice has the FCC structure), if the size of dislocation loops is large enough, it is energetically favorable for the $1/3 < 111 >$ loops (Frank loops) to transform into $1/2 < 110 >$ loops (perfect loops) [125, 126], releasing the energy stored in stacking faults [127] [14]; in body-center cubic (BCC) systems, e.g., α-Fe, $< 100 >$ loops can be formed through the direct interaction of $1/2 < 111 >$ loops of comparable size (both loops are perfect loops) [129], which is also energetically feasible according to Frank's rule.

For one of the example materials used in this thesis work, i.e., UO_2, the defect story usually starts from the creation of point defects (intersitials and vacancies) that is followed by the formation of $1/3 < 111 >$ Frank loops of interstitial type [55, 130]. Those Frank loops, by interacting with $1/6 < 11\overline{2} >$ dislocations (Shockley partial dislocations), can transform into $1/2 < 110 >$ perfect loops which are able to coalesce and form perfect dislocation lines [131–134]. In contrast to the evolution sequence of interstitials, vacancies tend to agglomerate into voids. The nucleation and growth of the voids presumably have two routes: (i) homogeneous nucleation due to thermal diffusion of defects [54] and (ii) inhomogeneous nucleation resulting from cascade overlaps [135] which can be described by the direct impact model [136]. In particular, a high burn-up structure (HBS, or rim structure) has been observed at the periphery of the UO_2 fuel irradiated inside nuclear reactors. The main HBS features are sub-divided grains, which contain a much lower defect density than the central region of the fuel, and increased porosity [54]. The formation of HBS had been attributed to recrystallization [137]. However, it has been argued that a more reasonable mechanism is based on the subdivision of original crystals due to a polygonization process in which fission product precipitates play an important role by pinning dislocations [138].

UO_2, like elemental pure bulk metals [44] and some insulators (c-ZrO_2 [139], MgO [140]) do not amorphize even at high radiation fluence. In contrast, some metallic alloys [141], some pyrochlores like $Gd_2Ti_2O_7$ [142] and most semiconductors (Si [143], SiC [144, 145]) are amorphizable materials. This last stage of defect evolution drives the final response of materials to irradiation, which could involve numerous factors. For example, in Sec.1.3.1, it has been mentioned that amorphous clusters can be directly created by collision cascades because of an inefficient defect annealing. Thus the overlap of such

[14] There is a controversy on the transform of Frank loops to perfect loops. A recent study on 316L stainless steel does not support the existence of a critical loop size for unfaulting [128].

cascades is able to render the target completely amorphous, such as in 3C-SiC [146]. On the contrary, in materials in which efficient recrystallization can happen within and after the whole collision cascade development, the total number of defects can even be decreased by overlapping cascades, such as in $\alpha-$Fe [147]. For more mechanisms, readers can refer to relevant papers [148–150].

Radiation effects: implanted ions (and ion range)

Implanted ions affect material properties not only by transferring energy to targets, but also through their presence as foreign atoms. On the one side, desirable species of ions can be introduced into targets to tailor electrical [151] and optical [152] properties of materials, generating beneficial effects; on the other side, ions deposited in materials may exert influence on defect evolution, for example, by suppressing void swelling [153], favoring amorphization [140], etc. In practice, and with respect to nuclear materials science, the additional effect on defect evolution brought by injected ions can impose limitations on emulating neutron irradiations with ion irradiations [17].

In order to assess the radiation effects induced by the deposition of implanted ions, it is necessary to evaluate their resting positions, which corresponds to their range. The range, R, can be calculated by integrating the inverse of the energy loss function:

$$R = \int_0^E \frac{dE}{dE/dx|_n + dE/dx|_e} \tag{1.50}$$

Values of R can be obtained by analytical approaches, such as the LSS theory [63]. Since an ion is constantly deflected by elastic collisions until it stops, the concept of R refers to the total length of the zigzag-like trajectory. For evaluating radiation effects, a more interesting quantity is the projected range, R_p, which is a value obtained by projecting R along the impinging direction. By neglecting electronic energy loss, the LSS theory provides a rule-of-thumb to approximate R_p from R [57]:

$$R_p \approx \frac{R}{1 + 3(M_2/M_1)} \tag{1.51}$$

The final depth distribution of ions, $N(z)$, can be approximated by a Gaussian distribution:

$$N(z) = \frac{\tau}{\triangle R_p \sqrt{2\pi}} exp\left[-\frac{(z - R_p)^2}{2(\triangle R_p)^2}\right] \tag{1.52}$$

where τ is the ion fluence, R_p is the mean value and $\triangle R_p$ is the standard deviation representing the straggling of the projected range.

For most cases, accurate range values can be calculated from BCA simulations, such as

with the use of SRIM [64]. When ions start to significantly interact with multiple atoms or the interatomic potential is angle-dependent, in principle, more accurate results can be obtained from MD simulations [154, 155]. In addition, SRIM calculations are based on the assumption of amorphous-like targets. However, it is reported that a large fraction ($\sim$ 20 - 60 %) of all crystal directions leads to ion channeling [156]. The ramification of ion moving along channeling directions is a decreased probability of having elastic collisions with small impact parameters compared to that in amorphous targets. Thus, in the case of channeling, the nuclear stopping term in Eq.(1.50) becomes smaller and the range is increased [15].

Radiation effects: electronic energy loss

In the low energy range where nuclear energy loss dominates, the role of electronic energy loss on modifying materials is considered to be insignificant, and its effect is simply represented by a viscous force acting on impinging ions. However, at higher energy, the electronic slowing-down process can have a significant effect on the material. In the inelastic thermal spike model, it is considered that the energy transferred to the electronic systems can be dissipated in the form of heat through an electron-phonon coupling, as follow:

$$C_e \frac{\partial T_e}{\partial t} = \nabla k_e \nabla T_e - g_p(T_e - T_l) + A(r,t) \tag{1.53a}$$

$$C_l \frac{\partial T_l}{\partial t} = \nabla k_l \nabla T_l + g_p(T_e - T_l) \tag{1.53b}$$

where C, k, T represent the heat capacity, thermal conductivity and temperature, respectively, the subscripts e and l represent the electronic and lattice systems, respectively, g_p is the electron-phonon coupling constant and $A(r,t)$ is the energy deposited to the electronic system as a function of space r and time t [157].

According to this inelastic thermal spike model, the energy transferred from the electronic to the lattice system creates a local heating along the ion trajectory. Such local heating can induce damage production even at intermediate energies where the nuclear and electronic energy loss are roughly of the same magnitude, such as in a-SiO_2 [158]. If the ion energy is further increased, latent tracks can be produced, for instance by swift heavy ions (SHIs) [159, 160]. The formation of tracks is attributed to the local melting resulting from the heat transferred from the electronic system to the lattice system, followed by a rapid quenching [161]. The threshold energy for track formation is found to increase with

[15] Apart from the decrease of nuclear energy loss, according to the Eq.(1.26) in the Firsov model, larger impact parameters can also lead to smaller electronic energy loss. This effect is observed in TDDFT calculations [73].

a higher thermal diffusivity [162]. Apart from the damage mechanism of local heating, the electronic energy loss can cause the cleavage of chemical bonds, resulting in radiolysis that gives rise to the formation of stable defects [163]. For example, in alkali halides, the excitation state induced by inelastic scattering can decay/relax through non-radiative processes, forming a double-halogen ion (H-center) and an anion vacancy (F-center) [164]. Although the term of electronic energy loss is dedicated to ion irradiation, radiolysis can also be induced by electron and high energy photon irradiations [165] which induce excitations and ionizations as in the case of ion irradiations [16].

What is in stark contrast to the defect production is that the electronic energy loss can also lead to damage recovery. For example, both experimentally and computationally, it is found that the electronic energy deposited by high energy ions (HEIs) can induce the recovery of pre-existing defects induced by low energy ions (LEIs) in SiC due to a local and highly efficient thermal annealing [145, 167]. A threshold electronic stopping power (presumably for annealing point defects) for this process to occur is proposed as 1.4 keV/nm [168]. As compared to the result of this type of sequential irradiation (i.e., LEI irradiations followd by HEI irradiations), a more pronounced defect recovery is found when LEIs and HEIs are used together (dual-beam irradiation), which was observed in MgO and SiC [144, 169]. The reason can be attributed to the fact that it is easier to anneal slightly disordered regions than highly disordered ones. Thus, during simultaneous irradiations, defects are annealed before they collapse to form a highly disordered region [157]. The study on HEI irradiations sheds light on the defect recovery induced by local heating. The beneficial effect of local heating may also take place in the process of collision cascades created by elastic collisions. One case is that the damage production in Ni-based single-phase concentrated solid solution alloys (SP-CSAs) tends to be lower than that in pure Ni, which could be related to a longer thermal spike lifetime because of less efficient heat conduction resulting from the chemical disorder in SP-CSAs [170].

There are also other factors affecting the final state of irradiated materials, including, temperature [171], dose rate [172], sub-threshold collisions [173], etc. In a short summary, the observable (micro-)structural modifications of materials under the bombardment of energetic particles is the integrated result of various atomic-scale processes that depend on the material intrinsic properties and on the irradiation conditions. Thus, it is of paramount importance to monitor such modifications, which can be accomplished by using the characterization techniques presented in the next chapter.

[16] In addition to inelastic scattering, electron irradiations can cause sputtering of samples through elastic collisions, which may impose a practical limit to the spatial resolution of TEM analysis [166].

Chapter 2

Characterization techniques

Both RBS/C and XRD are non-destructive techniques that are extensively utilized for the characterization of radiation effects in solids [42]. In this chapter, we will present the basic theories related to these two techniques as well as their specific applications used in this thesis work for gaining insights on radiation effects. In addition, we will provide details about how the XRD simulations used in this work are performed. Since significant efforts have been made to simulate RBS/C signals, the process of RBS/C simulations will be presented in the next, dedicated chapter.

2.1 Rutherford backscattering spectrometry in channeling mode

2.1.1 Basic theory

RBS/C is a special mode of more general characterization technique called RBS, named after E. Rutherford. It is claimed that the channeling concept was suggested during the 1910s [174], which is roughly in the same period when the Rutherford backscattering was discovered in the Geiger-Marsden experiments. Nevertheless, it seems that the concept of channeling did not get much attention until the 1960s, when "anomalous" effects related to channeling, such as anomalously long ranges of incident ions, were observed both in experiments [175, 176] and simulations [177, 178]. In this section, we will give the basic theory of RBS followed by that of channeling.

RBS

In a RBS experiment, a beam of light ions, usually He ions with energies on the order of MeV, are used to probe a target. A detector is placed at an angle close to the incident ion direction, but on the way back (hence, the backscattering process), in order to record

the energy distribution of backscattered ions, which allows generating the RBS signal. The Rutherford backscattering is described by an elastic scattering between an incident ion and a target atom, in which the interatomic potential is the Coulomb potential given in Eq.(1.8).

The energy of ions backscattered from the target surface, E_s, can be simply calculated by multiplying the kinematic factor, k, given in Eq.(1.2), with the incident energy, E_0. If the target is a very thin layer with a thickness $\triangle t$ containing only one element, then the yield recorded by the detection system, Y, can be calculated by:

$$Y = \triangle\Omega' \triangle t Q N \frac{d\sigma}{d\Omega'} \tag{2.1}$$

where $\triangle\Omega'$ is the solid angle subtended by the detector, Q is the number of incident particles, N is the target atomic density and $d\sigma/d\Omega'$ is the Rutherford differential cross section according to Eq.(1.14b). As shown in Fig.2.1, with a lighter target element, both the backscattered energy (E_s) and yield (the yield is determined by $d\sigma/d\Omega'$) decreases. Since the backscattered energy depends on the target element, the RBS technique can be used to detect the element type in targets. If a target with multiple elements is characterized, the element type can be determined by the measurement of the backscattered energy, and the dependency of the yield on the target element can provide the information about the stoichiometry.

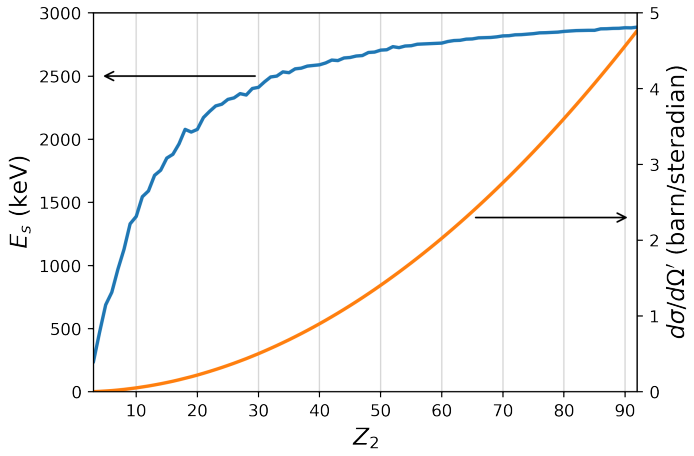

Figure 2.1 – Rutherford backscattering energy and differential cross section. The incident ion is a 3.085 MeV He ion. The backscattering angle is 165^o. The target elements range from Li to U.

If the target is thick, the incident ion that encounters a Rutherford backscattering event in the bulk will lose a considerable amount of energy in the penetration process. In

a first order approximation, the ion energy at depth t, E_t, can be approximated by:

$$E_t = E_0 - t\left(\frac{dE}{dx}\right)_{E_0} \tag{2.2}$$

where the incident direction of the ion is assumed to be perpendicular to the target surface, $(dE/dx)_{E_0}$ is the stopping power of incident ion entering the target. If the ion encounters a Rutherford backscattering event at depth t and is detected, then the detected energy is calculated by:

$$E_D(t) = kE_t - \frac{t}{|\cos\theta|}\left(\frac{dE}{dx}\right)_{E_D} \tag{2.3}$$

where k is the kinematic factor, θ is the angle of the detector center with respect to the direction of incident ion and $(dE/dx)_{E_D}$ is the stopping power of the incident ion leaving the target [179]. Therefore, an increase in t will lead to a spread of the distribution of E_D towards lower energies, and the RBS signal will exhibit a continuum spectrum from the maximum backscattered He energy to the minimum detectable energy (i.e., that for a He ion escaping the target after a backscattering event). The conversion of $E_D(t)$ into t is given as follows:

$$t = \frac{kE_0 - E_D(t)}{k(dE/dx)_{E_0} + (dE/dx)_{E_D}/|\cos\theta|} \tag{2.4}$$

The yield at each small depth interval, $Y(t)$, can still be calculated by Eq.(2.1). Since $d\sigma/d\Omega'$ is higher with a lower incident energy E_t, the yield in RBS spectrum gradually increases with a lower value of E_D, as shown in Fig.2.2 in which the blue spectrum represents the RBS spectrum obtained from a simulation of 1.4 MeV He ions on an Fe crystal. In RBS experiments, the target atoms in front of the incident ions have a random spatial distribution as if the target were amorphous, irrespective of its original target structure. Thus, a regular RBS spectrum can also be called a random spectrum when it is compared to spectra obtained in the channeling mode as introduced in the following.

Channeling

As introduced in Sec.1.3.2, incident ions encounter less large angle scattering events in channeling conditions than in random geometry. This channeling condition can be achieved by aligning the direction of an incident ion beam along a major axis of the crystal target. As shown in Fig.2.2, the yield of the spectrum obtained in the channeling mode (orange), denoted as aligned spectrum, is substantially smaller than that of a random spectrum.

The smaller yield in the aligned condition is mainly due to the fact that bulk atoms are covered by surface atoms along the channeling direction, which hinders small-impact-

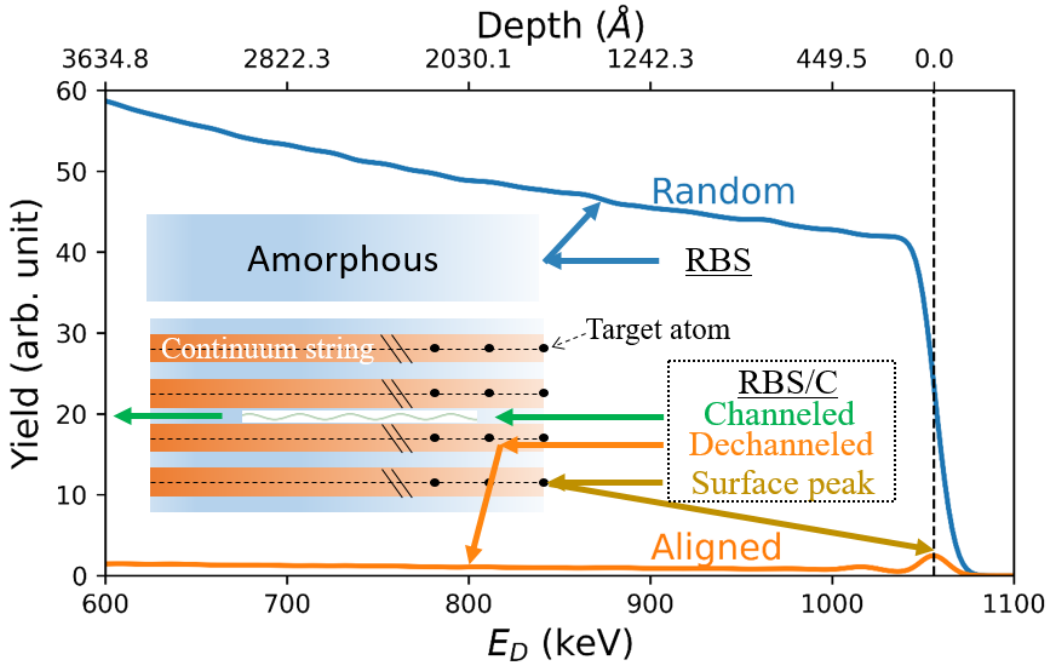

Figure 2.2 – RBS and RBS/C spectra of 1.4 MeV He ions on an < 001 >-oriented Fe pristine crystal.

parameter-collisions between incident ions and the bulk atoms. As illustrated in Fig.2.3, incident ions can be consecutively deflected by the first (A_1) and second (A_2) atoms in an atomic row. However, if the incident ion direction is parallel to the atomic row, then the impact parameter of the ion with the second atom, b_2, will always be larger than that with the first atom, b_1. If the interatomic potential is described by the Coulomb potential, and both the deflection angle due to the first atom, θ, and the ratio of M_1 to M_2 are small, then the relation between b_2 and b_1 can be calculated with the help of Eq.(1.9):

$$b_2 = b_1 + \frac{Z_1 Z_2 e^2 d_a}{E_0 b_1} \tag{2.5}$$

where d_a is the atomic spacing in the atomic row. According to Eq.(2.5), there is a minimum value for b_2, called the Coulomb shadow cone radius, which prohibits the collision between the ion and atoms inside this radius [180]. This effect is called the shadowing effect. Although the atomic thermal vibration magnitude can diminish the effect of shadowing, in general, there will still be more collisions with small impact parameters between incident ions and surface atoms as compared to those occurring in underneath layers. Thereby, a surface peak is observed in the aligned spectrum, as shown in Fig.2.2.

The origin of the yield behind the surface peak in the aligned spectrum can be

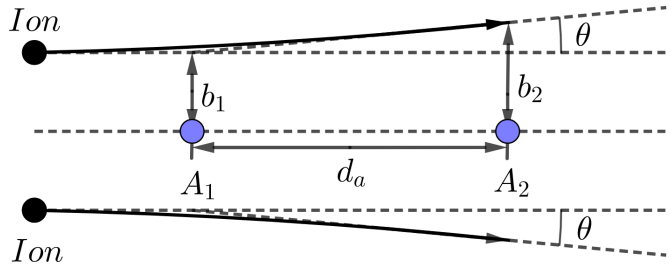

Figure 2.3 – Illustration of the shadowing effect in the Lab reference frame. A_1 and A_2 represent the first and second atom along an atomic row, respectively.

explained with the so-called continuum model. When incident ions are channeled, they experience successive gentle elastic collisions with target atoms in atomic rows. Lindhard [181, 182] proposed to consider the atomic rows as continuum strings, by which way the evaluation of binary collisions between ions and atoms are simplified to the study of the interactions between ions and strings. In this model, ions feel the continuum potential, U_a, due to the continuum strings, which can be calculated by:

$$U_a(r) = \int_{-\infty}^{+\infty} \frac{1}{d_a} V(\sqrt{z^2 + r^2}) dz \tag{2.6}$$

where z is the coordinate along the atomic row and r is the perpendicular distance between the ion and a row, as indicated in Fig.2.4. In addition, a well-channeled ion will have the same angles between a string, ψ, before and after the ion is scattered by the string.

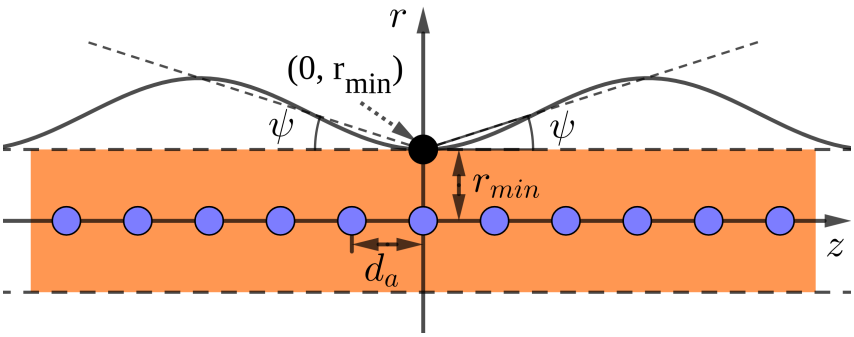

Figure 2.4 – Illustration of the continuum model. The blue circles represent target atoms. The orange region represents the continuum string. The ion trajectory is represented by the sinusoidal-like curve.

There is a minimum perpendicular distance of approach, r_{min}, for which the continuum model remains valid. In a channeling condition, the transverse kinetic energy of the ion, $E_\perp$, which is the component of kinetic energy perpendicular to the string, should be smaller than $U_a(r_{min})$. $E_\perp$ can be estimated as $E_0\psi^2$, where ψ is small. Hence, a general

criterion for channeling is given by:

$$\psi \leqslant \psi_c = \sqrt{\frac{U_a(r_{min})}{E_0}} \tag{2.7}$$

where ψ_c is the critical angle of channeling. There can be several definitions for ψ_c depending on the selection of r_{min}. One popular form of ψ_c, due to its simplicity is calculated as follows:

$$\psi_1 = \sqrt{\frac{2Z_1Z_2e^2}{E_0 d_a}} \tag{2.8}$$

in which the critical angle ψ_1 decreases with higher incident energy E_0 or d_a [182]. Experimentally, a critical angle denoted as $\psi_{1/2}$ can be measured by performing angular scans, in which the angle ψ is increased from 0 to a value larger than ψ_c. Thus, the yield will also increase in this process. The $\psi_{1/2}$ is determined as the angle where the yield is equal to the average of the minimum yield and the yield in the dechanneling condition.

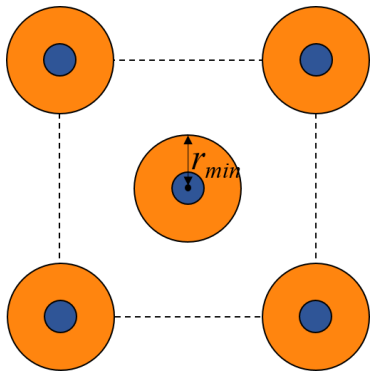

Figure 2.5 – The view of the continuum strings along the incident direction. The blue circles represent regions where small-impact-parameter-collisions between ions and target atoms can occur. The orange region represents the continuum string.

Fig.2.5 provides a view of the continuum string along the aligned direction. Ions entering the target through the blue regions will collide with target surface atoms with small impact parameters, which gives rise to the surface peak in the aligned spectra. Ions entering the target through the orange regions will not be directly backscattered, but their perpendicular distances to the strings are smaller than r_{min}. In this condition, the continuum model is not valid anymore so that these ions cannot be steered by the strings. Subsequently, these ions, called dechanneled ions, will experience collisions with target atoms as if the target were amorphous. The yield after the surface peak is mainly induced by these dechanneled ions. On the contrary, if an ion enters into the target through the white regions in Fig.2.5 and its initial moving direction with respect to the strings is smaller than ψ_c, the ion just bounces with the strings, but has no small-impact-

parameter-collisions with individual atoms. This kind of ions is called a channeled ion, which is steered into the target bulk and basically contributes to no backscattering signal. (More strictly, even in a pristine sample, with an increase of penetration depth of ions, some channeled ions can be dechanneled due to multiple scatterings with target electrons and collisions with targets atoms located at positions relatively far away from their original position because of thermal vibrations.) Due to the increase of $d\sigma/d\Omega'$ with decreased ion energy, the aligned spectrum will also gradually increase with a larger depth, as what occurs in the random spectrum [180]. [1]

2.1.2 Applications

Disorder levels

In targets containing defects, the yield in an aligned RBS/C spectrum can be primarily increased by two phenomena. The first one is due to the presence of atoms (e.g., point defects) right in front of the path of well channeled ions, which induces direct backscattering of ions, as for collisions with surface atoms. In the second phenomenon, the original crystalline structure is distorted by defects, which leads to dechanneling of channeled ions. This distinction between the direct scattering and dechanneling is called the two beam method [183]. Within the frame of this two beam method, the aligned spectrum generated from a defective sample should be decomposed according to the contribution of direct scattering and dechanneling, as shown in Fig.2.6. The relative disorder $f_d(t)$ in a target at depth t is then calculated as follows:

$$f_d(t) = \frac{y_a(t) - y_{de}(t) - y_s(t)}{y_r(t) - y_{de}(t) - y_s(t)} \tag{2.9}$$

where y_r represents the total yield of a random spectrum, y_a represents the total yield of an aligned spectrum for a damaged cell, y_{de} represents the yield induced by dechanneled ions and y_s represents the yield in the surface peak in an aligned spectrum of a pristine crystal.

In the current work, RBS/C simulations for characterizing disorder levels were mainly performed using MD cells with a thickness smaller than 50 nm. Examples of such RBS/C spectra, generated from a pristine and a damaged UO_2 MD cells, are shown in Fig.2.7, in which random spectra and aligned spectra are represented by blue and orange lines, respectively. It can be observed that the aligned spectra generated from both the pristine and damaged cells exhibit a peak shape due to the small thickness of the cells. Under

[1] In this work, we only talk about the axial channeling. There is also planar channeling, in which incident ions are steered by target atomic planes.

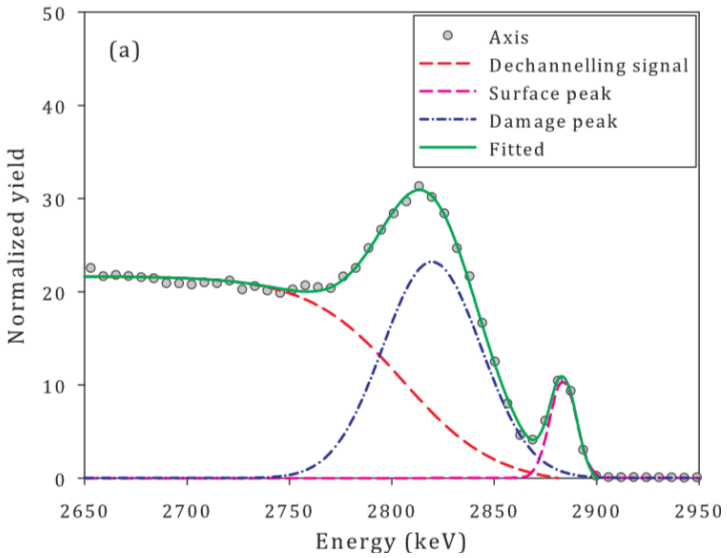

Figure 2.6 – Example of decomposing an aligned spectrum according to the two beam method. The green line is the fit to the signals of aligned spectrum. The blue, red and purple solid lines represent the contribution from the direct scattering (with defects), dechanneling and scattering with surface atoms, respectively. (Source: T. Nguyen, Ph.D. thesis, 2013 [184])

this condition, we can assume that there is no significant amount of dechanneling, and f_d given in Eq.(2.9) can be simplified to:

$$f_d = \frac{y_a - y_p}{y_r - y_p} \tag{2.10}$$

where y_p represents the total yield of an aligned spectrum generated from a pristine cell. Referring to Fig.2.7, y_p and y_a correspond to the areas under the orange spectra for pristine and damaged cells, respectively, while y_r is the total area under the blue spectrum.

Alternatively, an aligned spectrum can be fitted with a simulated one generated from a target containing known defects. Frequently, the defects used are a type of virtual defects called randomly displaced atoms (RDAs). If, by varying the concentration of RDAs along the target depth, the spectrum to be characterized can be well fitted by the simulated one obtained from the target containing RDAs, then the depth profile of relative disorder can be represented by that of the RDAs [185]. The disorder levels measured from experiments that will be presented in Chapter 4 are calculated from this RDA approach. In order to make sure that f_d calculated from Eq.(2.10) has a good correspondence with the quantity of RDAs, simulated spectra are generated from UO_2 cells containing different amounts of RDAs. f_d calculated from Eq.(2.10) as a function of the RDA level is presented in Fig.2.8, which shows that the value of f_d and RDA are roughly the same. There is only a slight discrepancy in the high RDA level, which is probably related to the algorithm for

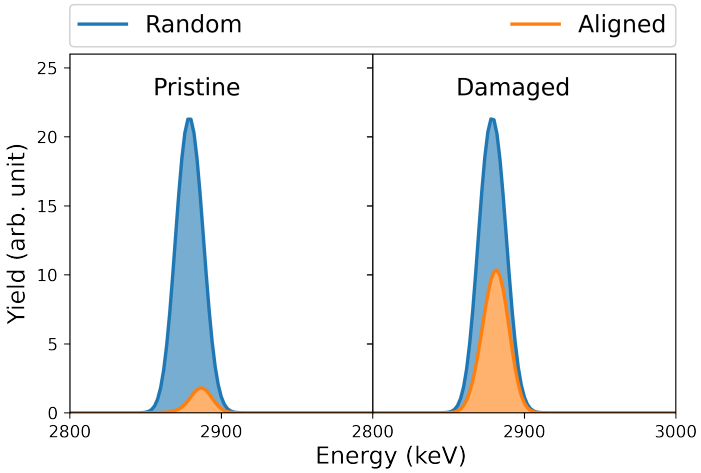

Figure 2.7 – RBS/C spectra generated from 3.085 MeV He ions on <001>-oriented pristine and damaged UO_2 MD cells. Blue lines represent the spectra generated in random configurations, and orange lines represent the spectra generated in $< 001 >$-oriented aligned configurations. The cell thickness is 22 nm.

generating the RDAs.

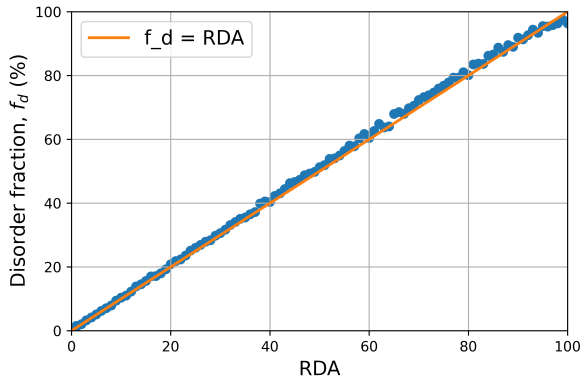

Figure 2.8 – Disorder fractions calculated from UO_2 MD cells containing different RDAs. The thickness of the cell is 22 nm. Blue circles represent the calculated disorder fractions. The orange line is a linear curve (thus representing $f_d = RDA$)

Identification of defect nature

The RBS/C technique can have a different response to different types of defects, which can be revealed by measuring the variation of the dechanneled fraction with changing the energy E_0 of incident ions. The probability of dechanneling per unit depth dP_D/dt is given by:

$$\frac{dP_D}{dt} = \sigma_D n_D(t) \tag{2.11}$$

where σ_D is the dechanneling cross section and $n_D(t)$ is the defect density at the depth t. Thus, the modification of the dechanneling fraction is connected to σ_D. As shown in Fig.2.9, isolated point defects can increase the dechanneling fraction by deflecting incident ions with an angle larger than the critical angle ψ_c. If the mass of ion M_1 is much less than that of target atom M_2 (which is the case for RBS/C measurements) and the form of critical angle is selected as ψ_1, then the cross section due to point defects, σ_D^p, can be estimated by integrating the Rutherford differential cross section given by Eq.(1.14) as follows:

$$\sigma_D^p = \int_{\psi_1}^{\pi} \frac{d\sigma}{d\Omega} d\Omega \approx \frac{\pi Z_1^2 Z_2^2 e^4}{E_0^2 \psi_1^2} = \frac{\pi Z_1 Z_2 e^2 d_a}{2E_0} \tag{2.12}$$

which indicates that the dechanneling fraction induced by point defects is roughly proportional to $1/E_0$ [180].

Dislocations can introduce distortions on atomic rows near the dislocation cores, which leads to an angle, θ', between the distorted atomic rows and the original channeling direction. If θ' is larger then the critical angle ψ_1, then it is considered that the distorted atomic rows cannot steer the channeled ions anymore. Based on this condition, it is found that the dechanneling fraction induced by dislocations is proportional to $E_0^{1/2}$. For dislocation lines, the dechanneling cross section, σ_D^{line}, can be calculated by:

$$\sigma_D^{line} = C_1 \left(\frac{E_0 b}{Z_1} \right)^{1/2} \tag{2.13}$$

where C_1 is a constant depending on the angle of channeling direction with respect to the dislocation direction, and b is the Burger vector of the dislocation. For dislocation loops, the dechanneling cross section, σ_D^{loop}, is smaller than σ_D^{line}, and it increases with increasing loop radius, r_{loop}. σ_D^{loop} would approach σ_D^{line} when r_{loop} is large. Nonetheless, σ_D^{loop} is still proportional to $E_0^{1/2}$. The relation between σ_D^{loop} and σ_D^{line} can be given by:

$$\sigma_D^{loop} = \sigma_D^{line} \frac{r_{loop}}{r_{loop} + r_c} \tag{2.14}$$

where r_c is a fitting constant [186]. One should note the difference between the dechanneling induced by point defects and by dislocations. In the former case, the dechanneled ions are deflected with an angle larger than ψ_1; in the latter one, the dechanneling occurs when incident ions cannot be steered by distorted atomic rows. Thus, it is not necessary that the dechanneled ions induced by dislocations have deflection angles larger than ψ_1. Some ions penetrating distorted atomic rows may still satisfy the channeling conditions in pristine bulk region due to a transparency effect [187].

The above relations between σ_D and E_0 are proposed based on analytical treatments,

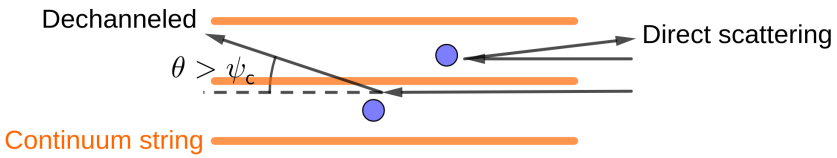

(a) Isolated point defects

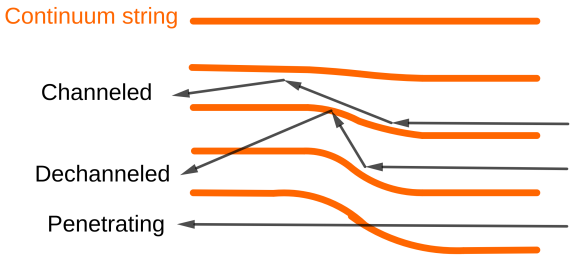

(b) Distortion of atomic rows

Figure 2.9 – Illustrations of mechanisms of dechanneling due to defects. The penetrating component indicates the ions dechanneled in the distorted region by penetrating the inclined atomic row.

which provides means for characterizing the type of defects in targets. However, the analytical calculations also involve certain approximations. In fact, if one wants to precisely and comprehensively determine the disorder level and the defect nature at the origin of this disorder, the use of atomistic calculations to generate or fit experimental signals is required, which is the purpose of the current work. In this framework, we will revisit in Chapter 4 the above-mentioned relations by simulating RBS/C signals from targets containing realistic defects .

2.2 X-ray diffraction

2.2.1 Basic theories

The generation of XRD signals results from the superposition of coherent X-rays (electromagnetic waves) scattered from different locations inside a target. The resultant amplitude of the scattered X-rays at the observation point can exhibit dramatic different features compared to the original one, including enhanced amplitudes resulting from constructive interferences and diminished amplitudes resulting from destructive interferences, depending on the wave phases. The electric field of X-rays, E, is in general written as:

$$\boldsymbol{E} = \mathbf{A_0} e^{i(\omega t - \mathbf{k_0 R})} \tag{2.15}$$

where $\mathbf{A_0}$ is the amplitude of the incident wave, ω is the angular frequency, t is the time, $\mathbf{k_0}$ is the wave number and $\mathbf{R}$ is the space coordinate. The magnitude of $\mathbf{k_0}$ is usually defined as equal to $2\pi/\lambda$, in which λ is the wavelength. The basic mechanisms of XRD can be obtained by examining the superposition of electric fields [2].

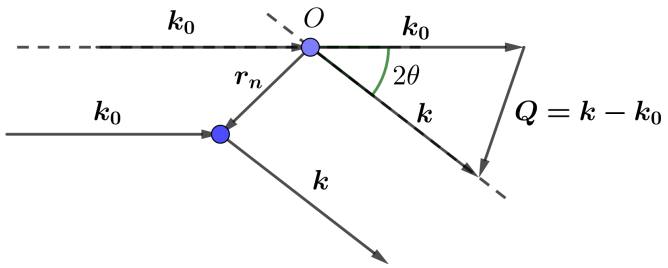

Figure 2.10 – Elastic scattering of X-rays from two scattering centers

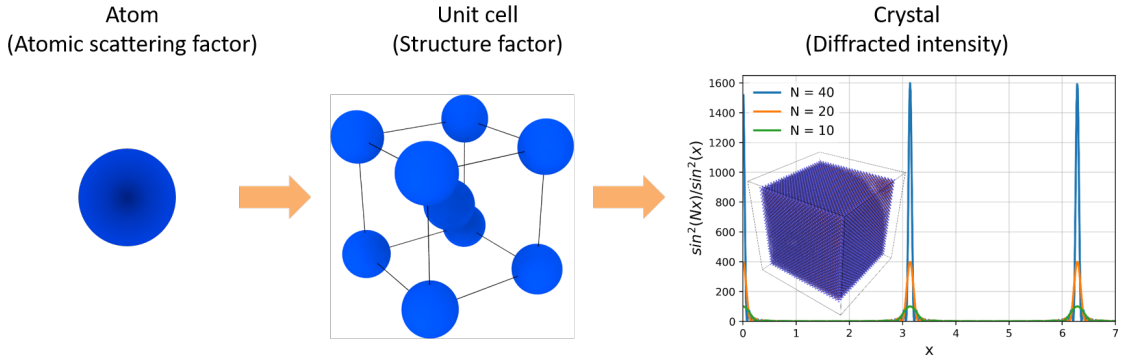

Figure 2.11 – Hierarchy of scattering structures: an atom, a unit cell and a crystal

As introduced in Sec.1.2.2, there are several ways by which photons can interact with target electrons. Since a coherent beam is required for constructive or destructive interferences, we are interested in the Thomson scattering (elastic scattering) [3]. In order to calculate the superposition of X-rays, we firstly need to know the relation among different X-rays elastically scattered from different scattering centers. As shown in Fig.2.10, a beam of polarized X-rays with wave vector $\mathbf{k_0}$ and amplitude A_0 are scattered by two scattering centers such as, for instance, free electrons. By assuming a polarized beam with the electric field normal to the plane of the paper, the electric field E_O of X-rays scattered at the point O can be given by:

$$E_O = \frac{A_0 e^2}{m_e c^2 R_d} e^{i(\omega t - \mathbf{kR_d})} \tag{2.16}$$

[2] In this thesis, the diffraction is treated by the kinematical theory. For a more rigorous evaluation, especially, for the diffraction from large perfect crystals, the dynamical theory should be applied [188].

[3] Compton scattering gives rise to diffuse background [92].

where $e^2 = 1.44$ eV·nm is in the cgs unit as that used in Eq.1.8, $\mathbf{R_d}$ is the distance vector from the point O to an observation position, $\mathbf{k}$ is the wave vector of scattered X-rays, $e^2/(m_e c^2)$ represents the classical radius of the electron [189] (Note that the polarization factor appeared in Eq.(1.43) is omitted, because we are assuming a beam polarized perpendicular to the plane of the paper.). The angle between the incident and scattered X-rays is 2θ. Then the electric filed E_n of X-rays scattered from the second point, which is at a distance r_n of point O, can be represented by multiplying Eq.(2.16) with an additional term that accounts for the path difference between the two waves:

$$E_n = \frac{A_0 e^2}{mc^2 R_d} e^{i(\omega t - \mathbf{kR_d})} e^{i\mathbf{Qr_n}} \tag{2.17}$$

where $\mathbf{Q} = \mathbf{k} - \mathbf{k_0}$ [4]. The resultant electric field at the observation point is just the summation of equations which have similar form to Eq.(2.17). Practical information can be obtained by performing such summation at different scales of atomic structures as shown in Fig.2.11

1. At the scale of an atom, an electron in an atom has no definite position so that X-rays could be scattered anywhere inside the 'volume' defined by the valence shells. Thus, the resultant electric field from an electron, E_e, in an atom is given by:

$$E_e = \frac{A_0 e^2}{mc^2 R_d} e^{i(\omega t - \mathbf{kR_d})} \int e^{i\mathbf{Qr}} \rho dV = \frac{A_0 e^2}{mc^2 R_d} e^{i(\omega t - \mathbf{kR_d})} f_e(\mathbf{Q}) \tag{2.18}$$

   where ρ represents the electron density, and the integral term is called the scattering factor per electron, $f_e(\mathbf{Q})$. The summation of $f_e(\mathbf{Q})$ contributed by all electrons in an atom gives the atomic scattering factor, $f_a(\mathbf{Q})$.

2. At the scale of a unit cell, the resultant electric field, E_u, is given by taking into account all atoms inside the cell:

$$E_u = \frac{A_0 e^2}{mc^2 R_d} e^{i(\omega t - \mathbf{kR_d})} \sum_p f_a^p(\mathbf{Q}) e^{i\mathbf{Qr_p}} = \frac{A_0 e^2}{mc^2 R_d} e^{i(\omega t - \mathbf{kR_d})} F \tag{2.19}$$

   in which f_a^p is the atomic scattering factor of atom p, and the summation term is called the structure factor, F. The calculation of F provides a guideline for selecting scattering planes denoted by (hkl). For example, in FCC systems, h, k and l values of scattering planes must be all even or all odd, otherwise no constructive interferences can be generated; in BCC systems, this condition is changed to that the sum of h, k and l must be even.

[4] Vector notations are replaced by scalar notations for electric fields and amplitudes. Since it is assumed that R_d is much larger than r_n, the difference of oscillating directions of scattered X-rays at the observation point is negligible.

3. At the scale of a crystal, a similar procedure as in Eq.(2.19) is applied to all unit cells as follows:

$$E_c = \frac{A_0 e^2}{mc^2 R_d} e^{i(\omega t - \mathbf{kR_d})} F \sum_{m_3=0}^{N_3-1} \sum_{m_2=0}^{N_2-1} \sum_{m_1=0}^{N_1-1} e^{i\mathbf{Q}(m_1\mathbf{a_1}+m_2\mathbf{a_2}+m_3\mathbf{a_3})} \tag{2.20}$$

where $\mathbf{a_1}$, $\mathbf{a_2}$, $\mathbf{a_3}$ are basis vectors of the crystal unit cell in a real space, and the crystal is assumed to have a shape of parallelopipedon with the edge lengths as $N_1 a_1$, $N_2 a_2$ and $N_3 a_3$ along the basis vectors. Eventually, the measured intensity, I_p, is proportional to the square modulus of the scattered electrical field $E_c E_c^*$:

$$I_p \propto |F|^2 \frac{\sin^2(N_1\mathbf{Qa_1}/2)}{\sin^2(\mathbf{Qa_1}/2)} \frac{\sin^2(N_2\mathbf{Qa_2}/2)}{\sin^2(\mathbf{Qa_2}/2)} \frac{\sin^2(N_3\mathbf{Qa_3}/2)}{\sin^2(\mathbf{Qa_3}/2)} \tag{2.21}$$

where the summation terms in Eq.(2.20) can be transformed into terms of $\sin^2(Nx)/\sin^2(x)$, in which N and x are variables. The value of $\sin^2(Nx)/\sin^2(x)$ have maxima when the ratio of x to π is integer, and it drops quickly, especially for large value of N, when x slightly deviates from integers of π. This feature gives rise to intensity peaks observed in XRD, which is the signature of an interference pattern.

Eq.(2.21) indicates that, in order to have XRD peaks, three conditions called Laue equations mush by satisfied:

$$\mathbf{Qa_1} = 2v_1\pi \tag{2.22a}$$

$$\mathbf{Qa_2} = 2v_2\pi \tag{2.22b}$$

$$\mathbf{Qa_3} = 2v_3\pi \tag{2.22c}$$

where v_1, v_2 and v_3 are three integers. Laue equations can be used to construct two more convenient methods for seeking diffraction conditions. Before presenting these methods, it is worth mentioning the basis vectors in a reciprocal space which are calculated as follows:

$$\mathbf{b_1} = \frac{\mathbf{a_2} \times \mathbf{a_3}}{\mathbf{a_1}(\mathbf{a_2} \times \mathbf{a_3})} \tag{2.23a}$$

$$\mathbf{b_2} = \frac{\mathbf{a_3} \times \mathbf{a_1}}{\mathbf{a_1}(\mathbf{a_2} \times \mathbf{a_3})} \tag{2.23b}$$

$$\mathbf{b_3} = \frac{\mathbf{a_1} \times \mathbf{a_2}}{\mathbf{a_1}(\mathbf{a_2} \times \mathbf{a_3})} \tag{2.23c}$$

These basis vectors have the following properties:

$$\mathbf{b_i a_j} = \delta_{ij} \tag{2.24}$$

where δ_{ij} is the Kronecker function. A vector $\mathbf{H_{hkl}} = h\mathbf{b_1} + k\mathbf{b_2} + l\mathbf{b_3}$ in the reciprocal lattice is perpendicular to planes denoted by the Miller indices (hkl) in the real space, and its magnitude is equal to the inverse of the spacing of adjacent (hkl) planes, i.e., $1/d_{hkl}$. The calculation of X-ray diffraction is often conducted in the reciprocal space for the sake of convenience.

With the aid of the properties of the reciprocal lattice, Eq.(2.22) can be simplified to:

$$\mathbf{Q} = (\mathbf{Qa_1})\mathbf{b_1} + (\mathbf{Qa_2})\mathbf{b_2} + (\mathbf{Qa_3})\mathbf{b_3} = 2\pi(h\mathbf{b_1} + k\mathbf{b_2} + l\mathbf{b_3}) = 2\pi\mathbf{H_{hkl}} \tag{2.25}$$

in which v_1, v_1 and v_1 are replaced by h, k and l. Therefore, the diffraction condition is directly related to the reciprocal lattice vectors: diffraction occurs when the scattering vector divided by 2π coincides with one reciprocal lattice vector. Furthermore, the magnitude of $\mathbf{Q}$ is $(2\pi/\lambda)2\sin\theta$. Thus, Eq.(2.25) can be transformed to:

$$2d_{hkl}\sin\theta = \lambda \tag{2.26}$$

which is the widely used Bragg's law [190].

2.2.2 Applications

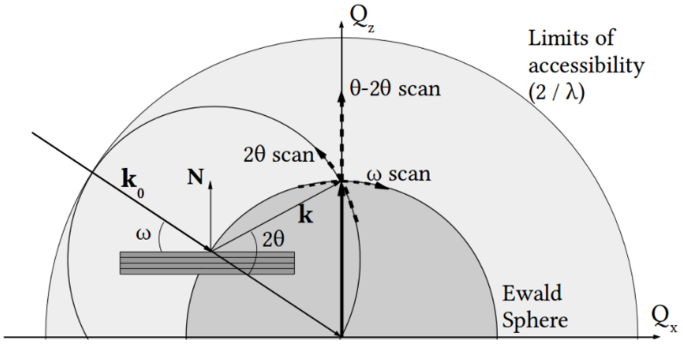

Figure 2.12 – Illustration of XRD scans, including $\theta - 2\theta$ and ω scans (Source: J. Channagiri, Ph.D. thesis, 2015 [191]; A. Debelle, Nucl. Instrum. Methods Phys. Res., B, 2010 [192])

Experimentally, XRD signals are usually recorded by performing so-called $\theta - 2\theta$ and ω scans. Fig.2.12 presents a schematic illustration of these XRD scans in the reciprocal space, in which the horizontal axis Q_x is parallel to the target surface, and the vertical

axis Q_z has the same direction to the surface normal $\mathbf{N}$. The wave vectors of incident and scattered X-rays use the same notations as given in Fig.2.10. The angle between $\mathbf{k_0}$ and $\mathbf{k}$ is always 2θ, but the angle between the k_0 and the target surface is ω. With basic trigonometry, the projections of $\mathbf{Q}$ onto Q_x and Q_z can be represented by following equations:

$$\mathbf{Q_x} = \frac{4\pi}{\lambda} \sin\theta \sin(\omega - \theta) \tag{2.27a}$$

$$\mathbf{Q_z} = \frac{4\pi}{\lambda} \sin\theta \cos(\omega - \theta) \tag{2.27b}$$

In the $\theta - 2\theta$ scan, ω is always equal to θ such that $\mathbf{Q_x} = 0$. Thus, only the reciprocal lattice points on the Q_z axis are covered. In the ω scan, ω varies independently with 2θ, while 2θ is kept constant. Since $\mathbf{Q_x}^2 + \mathbf{Q_z}^2 = \mathbf{Q}^2$, the endpoint of $\mathbf{Q}$ moves as if it was drawing a circle with the radius as its own magnitude. In terms of the Ewald sphere, its radius is $|\mathbf{Q}|/(2\pi)$. Thus, there is a maximum value for this radius, which is the limit of accessibility $(2/\lambda)$ as shown in Fig.2.12. If only the $\theta - 2\theta$ is recorded, a one-dimensional (1D) XRD spectrum is recorded, while varying both ω and θ allows generating a 2D reciprocal space map (RSM) around a reciprocal lattice point.

Elastic strain

Radiation defects, such as interstitials, can exert forces on atomic planes, which gives rise to irradiation-induced elastic strain, e^{def}, in damaged regions [193]. The effect on an XRD signal is a shift of diffraction peaks recorded in the damaged region as compared to those in the pristine region. The strain along the direction normal to the target surface can be calculated by:

$$e^{def} = \frac{d^{def}_{hkl} - d^{p}_{hkl}}{d^{p}_{hkl}} = \frac{\sin\theta^{p} - \sin\theta^{def}}{\sin\theta^{def}} \tag{2.28}$$

where d^{p}_{hkl} is the interplanar distance in the pristine region, d^{def}_{hkl} is the interplanar distance in the damaged region, θ^{p} and θ^{def} are the corresponding θ values of XRD peaks according to Eq.(2.26), respectively. However, in most of ion irradiation experiments, a large part of the bulk target is left intact, and this part can be viewed as a substrate onto which one can find the irradiated layer. The substrate hinders the volume change of the damaged region along in-plane directions, and hence increases the measured strain along the surface normal direction. In this case, the measured elastic strain should be divided by an elastic factor, f^{surf}, to get rid of the substrate effect. The elastic factor is given by:

$$f^{surf} = 1 + \frac{2\nu}{1 - \nu} \tag{2.29}$$

where ν is the Poisson's ratio of the target [192].

Disorder levels

Target atoms constantly vibrate around their original positions due to thermal vibrations. These vibrations can be taken into account by introducing a displacement term $\mathbf{u_p}$ into Eq.(2.19) as follows:

$$E_{u^T} = \frac{A_0 e^2}{mc^2 R_d} e^{i(\omega t - \mathbf{kR_d})} \sum_p f_a^p e^{i\mathbf{Q}(\mathbf{r_p}+\mathbf{u_p})} \tag{2.30}$$

where E_{u^T} is the new resultant electric field. Thus, by summing over the whole crystal, the measured intensity I_{p^T} exhibits a relation to thermal displacements as follows:

$$I_{p^T} \propto \sum_p \sum_{p'} f_a^p f_a^{p'*} e^{i\mathbf{Q}(\mathbf{r_p}-\mathbf{r_{p'}})} < e^{i\mathbf{Q}(\mathbf{u_p}-\mathbf{u_{p'}})} > \tag{2.31}$$

If $\mathbf{Q}(\mathbf{u_p} - \mathbf{u_{p'}})$ is small, or if this value follows a Gaussian distribution, the last term in Eq.(2.31) can be represented by (assuming that the displacements are mutually independent):

$$< e^{i\mathbf{Q}(\mathbf{u_p}-\mathbf{u_{p'}})} >= e^{-\frac{1}{2}\mathbf{Q}^2<\mathbf{u_p}>^2} e^{-\frac{1}{2}\mathbf{Q}^2<\mathbf{u_{p'}}>^2} = e^{-M_p} e^{-M_{p'}} \tag{2.32}$$

which indicates that the intensity of a diffraction peak would decrease due to thermal vibrations. Therefore, when the crystal consists of only one element, the decrease of intensity can be conveniently represented by multiplying a factor e^{-2M} called the Debye-Waller factor on I_p, in which M is equal to:

$$M = 8\pi^2 < u_\perp^2 > \frac{\sin^2\theta}{\lambda^2} \tag{2.33}$$

where $u_\perp$ is the projection distance of $\mathbf{u_p}$ along the direction of $\mathbf{Q}$, that is the direction normal to diffraction planes [92]. In some articles, the factor $B = 8\pi^2 < u_\perp^2 >$ in Eq.(2.33) is called the temperature factor [194], according to which the thermal vibration magnitude of target atoms can be calculated [195].

Similar to the effect of thermal vibrations, irradiation can also displace atoms and subsequently induces the attenuation of the intensity of diffraction peaks. The attenuation degree can be represented by a static Debye-Waller factor, DW. In this work, the DW factor is expressed as $DW = \sqrt{I_{p^d}/I_{p^T}}$ where I_{p^d} is the intensity from the damaged region [5]. The DW factor is used to estimate the disorder level of targets. In general,

[5] In literature, it can often be found that the DW factor is represented by $DW = I_{p^d}/I_{p^T}$. Here, in

with increasing the level of disorder, the DW factor would decrease from 1 (pristine) to essentially 0 (amorphous or severely distorted). A general form of the DW factor is given by:

$$DW = \int p(\delta \mathbf{u}) e^{i\mathbf{Q}\delta\mathbf{u}} \tag{2.34}$$

where $\delta\mathbf{u}$ represents a local atomic displacement and $p(\delta\mathbf{u})$ is the probability density function (PDF) of $\delta\mathbf{u}$. While a Gaussian distribution is a fair description of atomic thermal vibrations, A. Boulle and A. Debelle [196] have shown that a Lévy-stable distribution is more suitable for describing atomic displacements induced by irradiation. In such Lévy distributions, the atomic displacement PDF exhibits heavy tails, which indicates that some displaced atoms are far from the standard deviation given by a Gaussian distribution.

2.2.3 Simulations

XRD simulations can be performed by simply adding electric fields scattered from all atoms inside a crystal or utilizing fast Fourier transform (FFT) algorithms assuming that the field of atomic displacement is known. For calculations involving large number of atoms, the latter method is favorable compared to the former one in terms of computational speed. Since in these cases, the computational complexity of FFT, scaling as $Nlog(N)$ (N points in real space and N points in reciprocal space), is less than that of direct addition, scaling as N^2 [197]. However, the atoms in targets used in this work, i.e., MD cells containing arbitrary defects, may not be regularly distributed on 3 dimensional (3D) lattice. Thus, we chose the direct addition method to evaluate scattered intensities, which is accelerated by running codes on general purpose graphical processing units (GPUs).

According to Eq.(2.20), if a crystal target is assumed as a "super unit cell", the resultant amplitude of scattered X-rays, $\mathbf{A_{MD}}(\mathbf{Q})$, can be represented by:

$$\mathbf{A_{MD}}(\mathbf{Q}) = \sum_p f_a^p(\mathbf{Q}) e^{i\mathbf{Q}\mathbf{r_p}} \tag{2.35}$$

As shown in Eq.(2.25), $\mathbf{Q}$ can be described as a vector equal to $2\pi(h\mathbf{b_1} + k\mathbf{b_2} + l\mathbf{b_3})$ on a reciprocal space. Thus, by selecting hkl values in the vicinity of a Bragg reflection plane, a distribution of scattered intensity, $I_{MD}(Q_{b_1}, Q_{b_2}, Q_{b_3})$, in a 3D reciprocal space is obtained as:

$$I_{MD}(Q_{b_1}, Q_{b_2}, Q_{b_3}) = \mathbf{A_{MD}}(\mathbf{Q})\mathbf{A^*_{MD}}(\mathbf{Q}) \tag{2.36}$$

where $\mathbf{Q}_i$ represents the component of $\mathbf{Q}$ along the direction indicated by the subscript

order to keep consistency with our previous calculations, we choose to represent DW by $\sqrt{I_{p^d}/I_{p^T}}$.

i. In order to facilitate data evaluations, $I_{MD}(Q_{b_1}, Q_{b_2}, Q_{b_3})$ is further converted to a 2D intensity distribution, i.e., a reciprocal space map (RSM), by integrating along one specific direction, as follows:

$$< I_{MD}(Q_{b_1}, Q_{b_3}) >= \int I_{MD}(Q_{b_1}, Q_{b_2}, Q_{b_3}) dQ_{b_2} \tag{2.37}$$

in which case Q_{b_2} is normal to the scattering plane of the calculated RSM [197]. In addition, if a target contains multiple elements, anomalous-scattering factors can be added to f_a to take into account dispersion corrections, which depends on the wavelength of incident X-rays [198].

In defective crystals, the atoms are displaced from their original positions so that $\mathbf{r_p}$ can be represented by:

$$\mathbf{r_p} = \mathbf{r_p^o} + \mathbf{u_p}(\mathbf{r_p^o}) \tag{2.38}$$

where $\mathbf{r_p^o}$ represents the position of atom p in a pristine cell and $\mathbf{u_p}(\mathbf{r_p^o})$ is the associated displacement vector. The $\mathbf{u_p}(\mathbf{r_p^o})$ can be further decomposed to two terms:

$$\mathbf{u_p}(\mathbf{r_p^o}) = \nabla \mathbf{u_p}(\mathbf{r_p^o}) \cdot \mathbf{r_p^o} + \delta \mathbf{u_p}(\mathbf{r_p^o}) \tag{2.39}$$

where the first term, $\nabla \mathbf{u_p}(\mathbf{r_p^o}) \cdot \mathbf{r_p^o}$, represents a concerted movement of atoms in the whole cell due to the presence of defects, such as swelling of lattice, and the second term, $\mathbf{r_p^o}$, is the local atomic displacement given in Eq.(2.34), such as the displacement of an interstitial. $\nabla \mathbf{u}$ can be considered to be a strain tensor which is expressed as follows:

$$\nabla \mathbf{u} = \begin{bmatrix} e_{xx} & e_{xy} & e_{xz} \\ e_{yx} & e_{yy} & e_{yz} \\ e_{zx} & e_{zy} & e_{zz} \end{bmatrix} \tag{2.40}$$

where $e_{ij} = \partial u_i / \partial j$. In this strain tensor, the diagonal components, e_{ii}, represent either contraction or expansion along the direction i. Whereas, the off-diagonal components, e_{ij} $(i \neq j)$, indicate the existence of shear strain or rigid rotations. By inserting Eq.(2.38-2.40) into Eq.(2.36), one can calculate an averaged intensity which is composed of a coherent term and an incoherent term due to the diffuse scattering. Currently, we are interested in the coherent intensity, I_{coh}, which can be expressed as follows:

$$I_{coh} = \left| \sum_p f_a^p \left\langle e^{i\mathbf{Q}\delta\mathbf{u_p}(\mathbf{r_p^o})} \right\rangle e^{i\mathbf{Q}^T[\mathbf{I}+\nabla\mathbf{u_p}(\mathbf{r_p^o})]\mathbf{r_p^o}} \right| \tag{2.41}$$

where $\mathbf{I}$ is the identity matrix. The first exponential term just represent the DW factor given in Eq.(2.34), and the second exponential term affects the position of Bragg peak. By

recalling the Laue equations given in Eq.(2.22), we can find that Bragg reflections happen when the argument of the second exponential term equals to an integer multiplied with 2π. If, in a pristine cell, the Bragg reflection is measured at a vector, $\mathbf{Q_0}$, represented by $(0, 0, Q_{b_3})^T$, then the positions of Bragg peak in a damaged cell, $\mathbf{Q_d}$, will be shifted to $\mathbf{Q}^T(\mathbf{I}+\nabla\mathbf{u})^{-1}$ in order to fulfill the Laue equations. When the strain is small, $\mathbf{Q_d}$ can be estimated by:

$$\mathbf{Q_d} = \mathbf{Q}^T(\mathbf{I} - \nabla\mathbf{u}) = (-e_{zx}Q_{b_3}, -e_{zy}Q_{b_3}, (1 - e_{zz})Q_{b_3}) \tag{2.42}$$

Therefore, the information related to strain, that is e_{ij}, can be obtained by measuring the change of the positions of Bragg peaks.

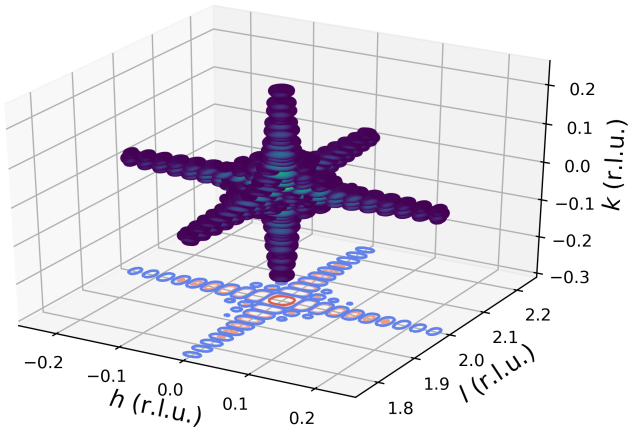

Figure 2.13 – The 3D intensity distributions calculated in the vicinity of the [002] Bragg reflection of a pristine UO_2 MD cell. The corresponding 2D distribution is displayed on the hl plane. Units of h, k and l are reciprocal lattice units (r.l.u), i.e., multiples of b_1, b_2 and b_3. (Intensities lower than the 0.04 % of the maximum are not shown here.)

Examples of strain components extractions from UO_2 MD cells are given hereafter. The cells used contain 768000 atoms and have a cubic shape with a 21.6 nm edge length. The x, y and z axes of the cells are along the [100], [010] and [001] directions, respectively. The 3D amplitude distribution is calculated in the vicinity of 002 Bragg reflection according to Eq.(2.36). Fig.2.13 shows the 3D intensity distribution calculated from a pristine cell, in which the reciprocal lattice units, h, k and l are along the x, y and z directions, respectively. Subsequently, the 3D intensities are integrated along the y direction in order to calculate 2D RSMs as shown in Fig.2.14, in which black dots define the peak location, O_i, where the subscript i, starting from 1, indicates the number of the peak. The intensity of O_i decreases with a higher value of i. Thus, O_1 always represents the peak with the maximum intensity. The location of these peaks are automatically detected using a dedicated module implemented in Python. In order to avoid the detection

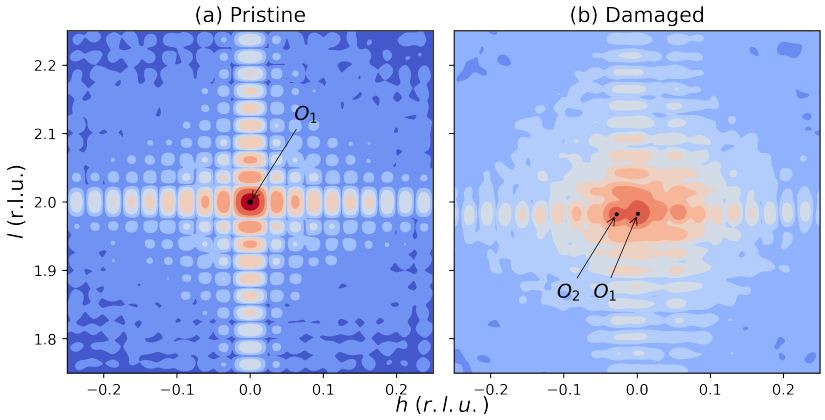

Figure 2.14 – The 2D intensity distributions calculated in the vicinity of the [002] Bragg reflection of pristine and damaged UO_2 MD cell. Peaks are indicated by black dots, in which the maximum one is denoted by O_1. Units of h and l are reciprocal lattice units (r.l.u). The intensities (on a logarithmic scale) are represented in a warm to cold color scale;

of interference fringes, we choose to only detect the peaks with intensities higher than 30 % of the intensity of O_1. The presence of multiple peaks usually indicates the existence of sub-crystallites or mosaic structures.

By comparing Fig.2.14.a and Fig.2.14.b, we can find that the position of the maximum peak in the damaged cell is shifted relative to that in the pristine cell. Since the position of this peak corresponds to the $\mathbf{Q}$ vector, the $\mathbf{Q_0}$ measured in the pristine cell can be represented by (h_0, l_0), where h_0 and l_0 are the h and l values of O_1 (here $h_0 = 0$ and $l_0 = 2$), respectively. In the damaged cell, the $\mathbf{Q_d}$ would be shifted to (h_d, l_d), where h_d and l_d are the h and l values of O_1, respectively. According to Eq.(2.42), $h_d = -e_{zx} l_0$ and $l_d = (1 - e_{zz}) l_0$. Thus, the elastic strain in the damaged cell along the z direction can be calculated by:

$$e^{def} = e_{zz} = \frac{l_0 - l_d}{l_0} \tag{2.43}$$

We can also find that the intensity of maximum peak in the damaged cell is smaller than that in the pristine one. In this case, the DW factor is calculated by:

$$DW = C_{DW} \sqrt{\frac{I_d^{h_d}}{I_0^{h_0}}} \tag{2.44}$$

where $I_d^{h_d}$ is the intensity integrated along the row $h = h_d$ in the damaged cell, $I_0^{h_0}$ is the corresponding value in the pristine cell and C_{DW} is a normalization factor defined by:

$$C_{DW} = \sqrt{\frac{I_0^{tot}}{I_d^{tot}}} \tag{2.45}$$

where I_d^{tot} represents the total intensity measured from the damaged cell and I_0^{tot} represents the corresponding value obtained from the pristine one. This normalization factor C_{DW} comes from the fact that the electron density of damaged cell is different compared to that of the pristine one due to the change of cell volume, and the scattered amplitude is proportional to the electron density. It is worth mentioning that the off-diagonal strain e_{zx} can be calculated by:

$$e_{zx} = -\frac{h_d}{l_0} \tag{2.46}$$

which can represent the tilt angle of the cell. Nonetheless, with only the information of e_{zx}, it is not enough to determine if the tilt is induced by a shear strain or a rigid rotation. For this purpose, the value of e_{xz} can be calculated by measuring the reflection from the [100] direction of the cell. As illustrated in Fig.2.15, a shear strain requires $e_{zx} = e_{xz}$, and a rigid rotation is possible when $e_{zx} = -e_{xz}$.

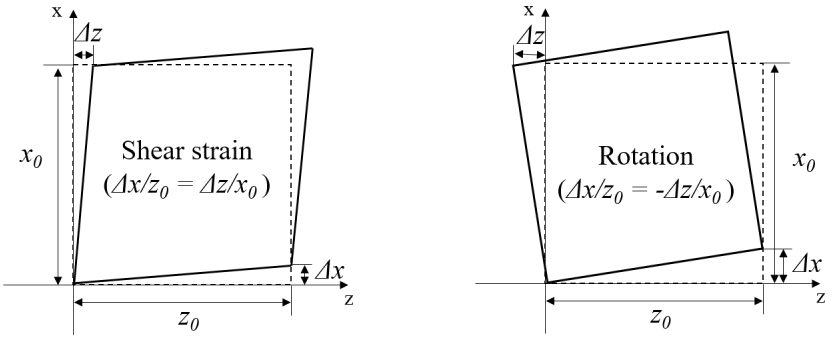

Figure 2.15 – Schematic illustration of shear strain and rigid rotation. $\Delta x/z_0$ and $\Delta z/x_0$ correspond to e_{xz} and e_{zx}, respectively.

Chapter 3

Simulations of RBS/C spectra of irradiated materials

As RBS/C signals are highly sensitive to modifications of the crystal structure, there is great interest to use this non-destructive method to extract information related to defects in crystalline materials. Analytically, the depth distribution of defects can be extracted from measured RBS/C spectra in the framework of the two-beam method [183], which distinguishes the RBS/C yield generated by direct scattering events from that due to dechanneling. The two beam method is usually implemented by using the so-called iterative procedure [199–201], in which defect densities are determined from surface to bulk regions step by step. However, it is difficult to acquire information about the detailed nature of defects from this analytical approach. Alternatively, RBS/C spectra can be generated from Monte Carlo (MC) simulations, in which the trajectories of incident ions are followed in a simulated target. By comparing simulated spectra to experimental spectra, it is possible to get clear insights on the detailed nature of defects. In this chapter, we will first give a brief review on the development of MC simulations of RBS/C spectra, from early simulations of ion channeling to the development of the RBSADEC code used in this work. Then, we will present our work dedicated to extending the applicability of the RBSADEC code.

3.1 MC-RBS/C simulation methods

The first step of MC-RBS/C simulations would be the reproduction of the trajectories of well-channeled ions. In the early 1960s, M. Robinson and O. Oen [177, 202] simulated the interaction of incident ions with target atoms by taking into account the target structure. In their simulations, the channeling phenomenon was observed, and it allowed explaining abnormal (at that time) results found in experiments of ion penetration

(namely, a too large ion range in channeling conditions as compared to that in an amorphous-like structure). The simulations were performed in the framework of the BCA model, with the use of screened interatomic potentials. The simulations proceeded from the search of the target atoms with which the incident ion could collide. At each collision event, the scattering integral and time integral were evaluated (note that the form of the scattering integral was given in Eq.(1.7)). The first integral led to the determination of the projectile deflection angle. The second one was applied to assess the shift of the center of mass of the ion / target atom system during the collision, which determines the starting location of the deflection trajectory approximated by a straight asymptotic line. Thus, the history of the ion is followed by a repeated procedure of search and collision until the ion is terminated by certain conditions (e.g., reaching a given threshold energy). Although the BCA method was originally designed for two-body collisions, in their simulations, Robinson and Oen also took into account the interaction of an ion with multiple target atoms simultaneously, a process called simultaneous collisions.

After around 10 years, M. Robinson and I. Torrens [101] developed the well-known program called MARLOWE used to describe ion-solid interactions in crystalline solids. The MARLOWE program is more sophisticated (e.g., application of more realistic interatomic potentials) than Robinson's simulation program used in the 1960s. Nevertheless, the basic procedures for determining the ion trajectories are roughly the same. The RBSADEC code determines the ion trajectories according to the methods used in MARLOWE. Theoretically, it is possible to generate RBS/C spectra through this kind of simulations. However, in practice, it would take an unacceptable amount of time due to the extremely rare probability of backscattering events.

A breakthrough was made by J. Barrett in his channeling simulations in the late 1960s and early 1970s [203, 204]. The calculation of ion trajectories was much simpler than in MARLOWE: (i) in a collision event, only the deflection angle is calculated according to the impulse approximation; (ii) energy losses (including both elastic and electronic components) of the ion are neglected. Thermal vibrations of target atoms follow a Gaussian distribution. Instead of waiting the occurrence of close nuclear encounter events such as large angle scatterings, Barrett's calculated the probability of such events to occur for each collision event. This probability is called the nuclear encounter probability. Its normalized quantity, P_{NE}, is derived as follows:

$$P_{NE} = \frac{\cos\psi_b}{2\pi u_1^2 N d N_c} \sum_{i=1}^{N_c} e^{-\rho_i^2/(2u_1^2)} \tag{3.1}$$

where ψ_b is the angle between the incident beam direction and the channel direction, i

is an index number labeling a particular binary collision, u_i is the 1D root mean square (rms) vibration magnitude of target atoms, ρ_i is the radial distance from the trajectory to the row containing the ith atom, N is the target atomic density, d is the spacing along the row and N_c is given by the number of calculated trajectories multiplied by the thickness of the crystal divided by d [174]. Although Barrett did not generate particular RBS/C spectra, he was able to calculate quantities closely related to RBS/C signals, e.g., half-angles of channeling and minimum yields, using P_{NE}.

Based on the early development of simulations of ion-solid interactions, several MC-RBS/C simulations have been developed after incorporating the concept of P_{NE}. One example is the BISIC code, which can be used to simulate the depth profile of implanted ions [205]. The procedure for calculating the ion trajectory is similar to that used in MARLOWE. In lieu of treating electronic energy loss as a viscous force as that applied in SRIM, the electronic energy loss is calculated at each collision event with a target atom according to the impact parameter [206]. Small deflections due to multiple scatterings with electrons are accounted for as well [207]. In each collision event, a virtual backscattered ion is generated, which moves towards the detector. The yield contributed by this ion is determined by the product of the associated P_{NE} with the Rutherford cross section. The energy loss is calculated according to the path of the ion [208]. By this way, the code provides the yield as a function of the ion energy, i.e., a RBS spectrum [209, 210]. It is worth mentioning that this code has been used to generate RBS/C spectra from targets containing realistic point defects and small clusters, in which the target is allowed to relax in order to reproduce the effect of distortions induced by injected defects [211, 212].

Another example is the McChasy code [213]. It determines the ion trajectories using a method called the planar scattering approximation (PSA) based on the BCA method. In the PSA method, atoms are located in planes that are perpendicular to the channeling direction. When an ion passes through a plane, it interacts simultaneously with several atoms on that plane. The deflection angle is calculated by the impulse approximation [214]. P_{NE} is determined when the ion passes through the plane. Then, RBS/C spectra are obtained in a way similar to that used in BISIC [213, 215]. This code can generate RBS/C spectra from targets containing RDAs. This type of defects describes reasonably well the disorder produced during amorphization of materials (which contain small clusters of point defects that evolve into amorphous regions), but do not account properly for dislocation-type defects (and the lattice distortions around the RDAs are not taken into account either). Yet, this code and the disorder level derived from the data refinement are very useful for determining and comparing disordering kinetics in all crystalline materials under any irradiation conditions. After further development, the code was improved to account for extended defects, such as dislocations, for which the distortion around the

dislocation core is computed by analytical methods [216, 217].

There are also simulations with different features with the above-mentioned codes, in which the influence of atoms adjacent to the colliding target atom on the ion may be taken into account more thoroughly. One example is Barrett's program called LAROSE [218], which can be viewed as an updated version of his previous program for channeling calculation [204]. The program views the target lattice as composed of rows with one row defined as central. When an ion interacts with an atom in this central row according to the binary collision method, the influence from other rows are taken into account by calculating the continuum potential felt by the ion. Another program named FLUX treats the interaction of ions and nearby atoms in a way similar to that used in LAROSE [207]. Subsequently, RBS/C spectra are obtained using the method similar to that applied in BISIC. Nonetheless, the introduction of continuum rows may impose strong limitations on the choice of target structures. For example, it is difficult to claim that there still exists the so-called continuum potential in highly disordered or amorphous targets.

3.1.1 RBSADEC

Compared to the above-mentioned codes, RBSADEC has a unique virtue which is the ability to generate RBS/C signals from targets containing arbitrary structures. Note that arbitrary does not mean here without any logic, on the contrary, it implies that any defect type and thus any (preferentially) real microstructure can be used. The input data can be obtained from atomic-scale modelling techniques such as MD simulations [52]. A new version of McChasy (McChasy2) can also use MD cells as targets. However, the details of McChasy2 have not yet been published. In the RBSADEC code, the interaction of incident ions with target atoms is determined according to the method used in MARLOWE. The interatomic potential is described by the universal Ziegler-Biersack-Littmakr (ZBL) potential [59]. The associated scattering and time integrals are numerically solved by using the Gauss-Mehler quadrature integration method [219].

More precisely, the interaction starts with the search, considering the potential impact parameters, of target atoms with which the ion can collide with (these atoms are called collision partners). All target atoms in front of the moving direction of an ion are potential candidates of such an event. The code checks the impact parameters, b_i, between the ion and candidate atoms i and excludes those atoms with b_i larger than a maximum value b_{max}, such as the atom T_3 shown in Fig.3.1. b_{max} is defined as the radius of the average atomic volume, r_v, calculated by $[3/(4\pi N)]^{1/3}$, where N is the atomic density. Then, the projection lengths, ξ_i, of atoms with $b_i < b_{max}$ along the moving direction of ion are calculated. Eventually, the atom(s) with the minimum projection length, ξ_{min}, is(are)

selected as the collision partner(s).

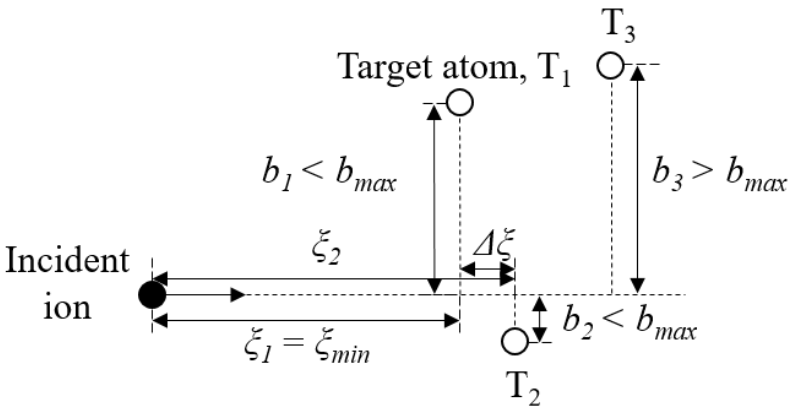

Figure 3.1 – Illustration of the search of collision partners.

For each collision, the nuclear encounter probability, P'_{NE}, is determined similarly to that used in the Barrett's calculation, which is expressed as follows:

$$P'_{NE} = \frac{1}{2\pi u_1^2} e^{-b^2/(2u_1^2)} \tag{3.2}$$

where u_1 is the 1D rms atomic thermal vibration magnitude. The atomic thermal vibrations follow uncorrelated Gaussian distributions. At the same time, a virtual backscattered ion is generated at the collision point. If this virtual ion can finally make its way to the detector, the yield contributed by the ion is determined by the product of P'_{NE} with the associated Rutherford differential cross section. The initial direction of the virtual ion is confined in a cone with its center pointing to the detector center, in order to take into account the multiple scatterings with target atoms [220], as shown in Fig.3.2. The angle between the cone center and its boundary is defined as the spread angle, θ_s, which is a preset and fixed value, i.e., 60°. Since, generally, the backscattered direction is not along any major crystallographic direction, it is legitimate to consider that target atoms in front of the virtual ion are randomly distributed. Therefore, there is no need to implement the procedure of searching for collision partners for virtual ions, as that used for the "real" incident ions. Instead, the code calculates a straight free flight path (FFP) between two successive collisions for virtual ions. At the end of each FFP, an impact parameter is randomly selected in order to determine the deflection angle of the virtual ion induced by a new collision event. This procedure can be called the amorphous slowing-down process, and its computation is much quicker than that of the collision-partner-search process. In addition, the nuclear energy loss at each collision is calculated according to Eq.(1.3), and the electronic energy loss in FFP is subtracted according to the table of electronic stopping power which is provided by users as a prerequisite file.

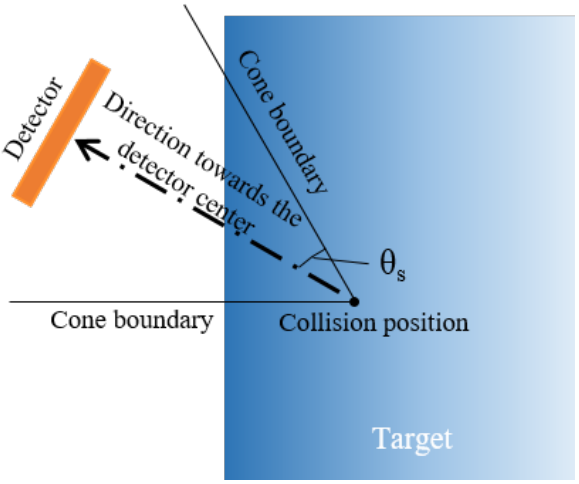

Figure 3.2 – Illustration of the initial directions of virtual ions.

When the lifetime of a virtual ion is over, for example, by reaching the detector, the incident ion will move forward and search new collision partners. Thus, as the incident ion penetrates through the target and collides with atoms, virtual ions are continuously created during elastic collision events. A RBS/C spectrum is then generated according to both yield and energy of backscattered virtual ions reaching the detector. As stated before, this code can read targets containing arbitrary structures, not only limited to point defects or dislocations described by analytical methods. This code has been used to simulate RBS/C spectra from MD cells containing realistic defects, the results of which exhibit satisfactory agreements with experiments, as shown in refs. [45, 52, 221] and in the next chapter of this manuscript.

3.2 Improvement of RBS/C simulations

The RBSADEC code represents an important progress in the simulation of RBS/C spectra. It can generate satisfactory results in several conditions previously mentioned. However, we found that the simulated spectra in some conditions exhibited non-negligible discrepancies with experimental ones. Fig.3.3 shows RBS/C spectra of 3.085 MeV He ions on a pristine <011>-oriented UO_2 crystal, both in random and aligned configurations. The open circles represent experimental spectra, which were obtained using the ARAMIS ion accelerator of the JANNuS-SCALP platform in Orsay [222, 223] with a 3.085 MeV He^{2+} beam. The random spectrum was recorded by rotating the crystal target off the <011> direction by a tilt angle of 4°. A passivated implanted planar silicon (PIPS) detector was located at 165° with respect to the aligned beam direction in order to detect backscattered He ions. The energy resolution of the detector system was 15 keV. Solid lines in Fig.3.3 represent the simulated spectra obtained from the original RBSADEC

code, in which the UO_2 target was defined by a box with the z axis along the <011> direction, which means the z axis is perpendicular to the target surface. Periodic boundary conditions were applied in the x and y directions. The atomic coordinates were set according to the perfect crystal. The table of electronic stopping power of He ions in UO_2 was extracted from RUMP [80]. The incident ion direction was defined by a polar angle, θ_n, and an azimuthal angle, ϕ_n, as shown in Fig.3.4. The simulated random spectrum was obtained by setting the θ_n of the beam center to 4° and increasing the ϕ_n of the beam center from 0° to 359°, with 1° as interval for each ion.

It can be found that the simulated spectra, both in random and aligned configurations, fit well the experimental ones, but only in the high energy region. In contrast, when the energy is below 2000 keV (corresponding roughly to 1 μm), the simulated spectra gradually deviate from the experimental ones. Thus, we performed a work dedicated to improving this fit, as well as to extend the flexibility of the code. In the following, this work will be separated into four parts.

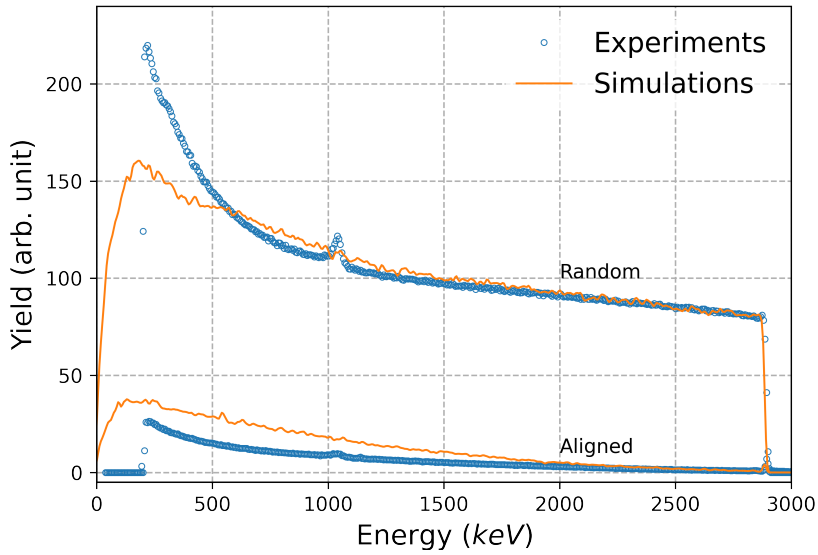

Figure 3.3 – RBS/C spectra of 3.085 MeV He ions on an pristine <011>-oriented UO_2 crystal in random and aligned configurations. Open circles and solid lines represent experimental spectra and the spectra generated by the original RBSADEC code, respectively.

3.2.1 Simulations of random spectra

Since, in the random configuration, the arrangement of target atomic structure appears as amorphous for incident ions, the shape of random spectra is mainly determined by the approach of the amorphous slowing down process and the electronic stopping power. The table of electronic stopping power from RUMP has already been proven valid in

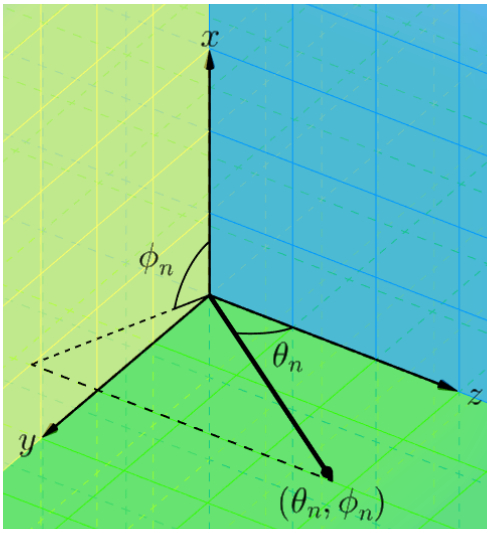

Figure 3.4 – Illustration of incident directions of ions in spherical coordinates.

other codes, e.g., in the McChasy code. This indicates that the improvement should be performed on the slowing-down approach, which is composed of two parts, i.e., the selection of both impact parameters and FFPs with a random distribution. Over past decades, multiple models for the selection of these two quantities have been proposed. Our approach is to incorporate different models into RBSADEC, and then test which model can generate the most satisfactory spectra.

Models of FFPs

The original model used in the RBSADEC code is to choose the FFP according to a random sampling described by a Poisson process. The average value of this Poisson process is set to $10r_v$. This model will be denoted as the random sampling model in the following.

Another widely used model is the one used in TRIM [58, 59]. In this model, the length of the FFP, L_{FFP}, is energy dependent, and its value is chosen so that the mean angular deflection per L_{FFP} remains at 5°. However, attention should be paid to this model. On the one hand, the electronic energy loss along L_{FFP}, $\triangle E_e$, is calculated by:

$$\triangle E_e = \left.\frac{dE}{dx}\right|_e (E_s) \times L_{FFP} \tag{3.3}$$

where E_s is the energy of the ion at the starting point of FFP. During the free flight, it is assumed that the electronic stopping power $\left.\frac{dE}{dx}\right|_e (E_s)$ is constant and determined by E_s. However, for He ions with energies in the MeV range, the FFPs can be as large as a micrometer, as shown in Fig.3.5. It may not be valid to consider that the electron stopping power remains constant over such a long path. Therefore, we divided each FFP

into several small segments. The energy of a He ion at the starting point of each segment is calculated as follows:

$$E_i = E_{i-1} - \frac{dE}{dx}\Big|_e (E_{i-1}) \times L_{sub} \tag{3.4}$$

where i is the segment number and L_{sub} is the segment length equal to 100 Å. The electronic stopping power and energy loss at each segment i are evaluated according to E_i. Finally, the total energy loss in the FFP is the summation of the energy losses in every segments. On the other hand, when the He energy is very small, the length of the FFP can be decreased so much that its value is smaller than the mean atomic separation defined by $N^{1/3}$. In this case, the FFP is set to this mean atomic separation. In the following, this FFP model will be denoted as the energy dependent model.

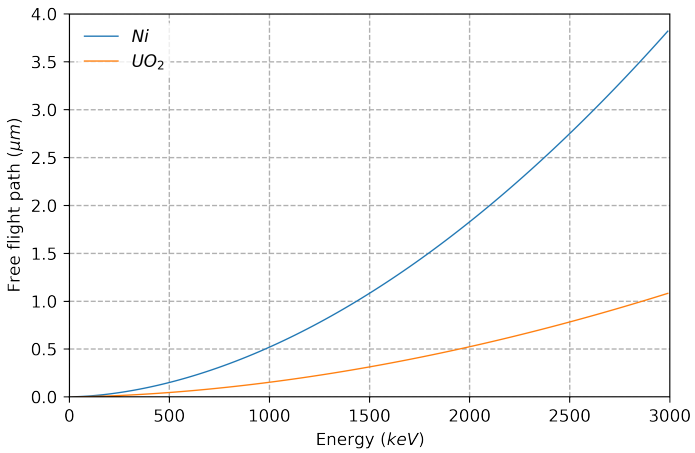

Figure 3.5 – FFPs of He ions in UO_2 (orange) and Ni (blue).

A third model is to set the FFP as a constant value, i.e., 100 Å. This model has been also applied in some BCA calculation codes [103, 224]. In the following, the model will be denoted as the fixed value model.

Models of impact parameters

Models for randomly selecting impact parameters always depend on FFPs. In the original method of the RBSADEC code, it is assumed that an ion can definitely collide with a target atom inside a fixed volume. However, there is an ambiguity about the exact value of this fixed volume. According to the published paper [52], it seems that it is intended to set the fixed volume as $1/N$. Yet, inside the code, this value is r_v^3. Here, we will use r_v^3 for testing the original approach. Thus, the impact parameter will be selected from 0 to a maximum value b_{max} defined as $(r_v^3/\pi L_{FFP})^{1/2}$. As shown in Fig.3.6, the fixed volume can be represented by a cylinder. With a longer L_{FFP}, b_{max} will be smaller in order to keep the volume of the cylinder unchanged. The probability of certain impact

parameters being selected, $f_1(b)$, linearly increases with the value of b. Its probability density function (PDF) is defined as:

$$f_1(b) = \frac{2\pi b L_{FFP}}{r_v^3} \; for \; 0 \leqslant b \leqslant b_{max} \tag{3.5}$$

It can be found that, by imposing the maximum value for b in Eq.(3.5), the cumulative distribution function (CDF) of $f_1(b)$ is no larger than 1. In the following, this model will be denoted as the original fixed-volume model.

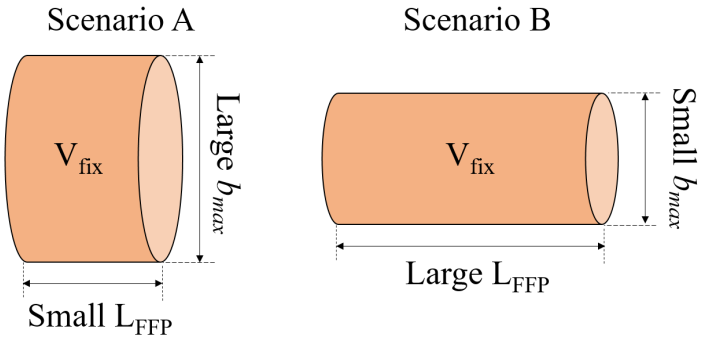

Figure 3.6 – Illustration of the fixed-volume method

The second model is similar to the first one in the sense that both of them use the fixed-volume method. The difference is that the maximum impact parameter is set to $[1/(\pi N L_{FFP})]^{1/2}$ so that the fixed volume equal to $1/N$ which equals to $4\pi r_v^3/3$. Its PDF, $f_2(b)$, is expressed as follows:

$$f_2(b) = 2\pi N b L_{FFP} \; for \; 0 \leqslant b \leqslant b_{max} \tag{3.6}$$

which also linearly increases with b. In the following, this model will be denoted as the modified fixed-volume method.

The third model is the one used in TRIM [58], which looks more sophisticated than the fixed-volume methods. This model not only considers the probability of finding a target atom at b, but also considers the probability of not finding an atom with an impact parameter smaller than b. Its PDF function, $f_3(b)$, is calculated as follows:

$$f_3(b) = e^{-\pi N L_{FFP} b^2} \cdot 2\pi N b L_{FFP} \tag{3.7}$$

in which the right term is the same as in Eq.(3.6). In the following, this model will be denoted as the TRIM-exponential model.

Quantitative comparisons between the three impact parameter models are presented in Fig.3.7. The target is UO_2 and the L_{FFP} is set to 100 Å. It can be found that the probability derived from the original fixed-volume model, in its validity range, is always larger than those derived from the other two models. The modified fixed-volume model shares similarity with the TRIM-exponential model in the small impact parameter region. One particular feature of the TRIM-exponential model is that there is no limitation of the maximum impact parameter in this model; the probability gradually vanishes in the high impact parameter region.

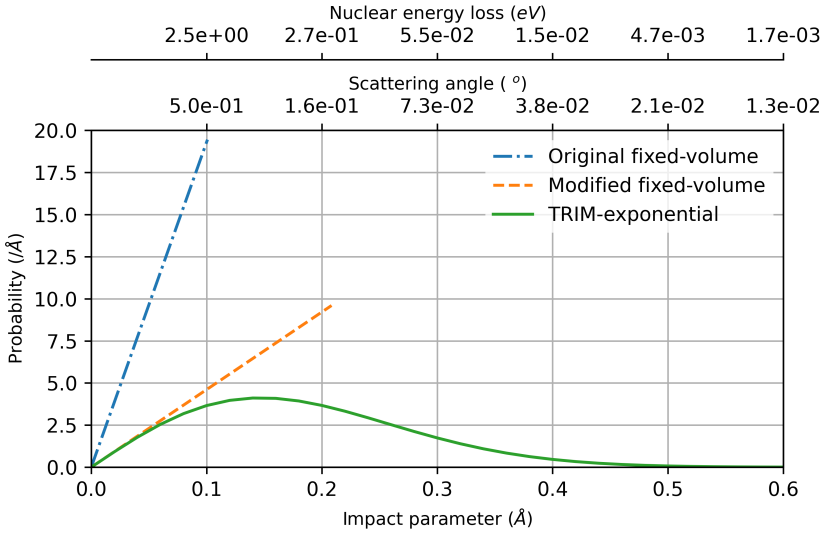

Figure 3.7 – The PDFs of the three impact parameter models in UO_2 with the L_{FFP} equal to 100 Å. The upper two axes represent the nuclear energy loss and deflection angle of a 2 MeV He ion colliding with a U atom. (Figure source: Jin et al., Model. Simul. Mat. Sci. Eng., 2020. [225])

A complete approach for describing the amorphous slowdown process needs the combination of the FFP and impact parameter models. Here, we propose five approaches for testing their ability of generating satisfactory spectra, which are: the original, the TRIM-based, and the alternative slowdown (ASD1, ASD2 and ASD3) approaches. The combinations of options used in these different approaches are listed in Table I. Note that the original approach is the one used in the original RBSADEC code.

Implementations of amorphous slowdown approaches

In order to test the validity of different amorphous slowdown approaches, the RBS/C spectra in random directions obtained from a UO_2 crystal using 3.085 MeV He ions are compared in Fig.3.8. In this figure, the circles represent the experimental spectra, and the solid lines with markers represent the simulated spectra using (a) the original approach

Table I – Amorphous slowdown approaches

	FFP models	Impact parameter models
Original	Random sampling	Original fixed-volume
TRIM-based	Energy dependent	TRIM-exponential
ASD1	Random sampling	TRIM-exponential
ASD2	Fixed	TRIM-exponential
ASD3	Fixed	Modified fixed-volume

and (b) the TRIM-based approach. For the purpose of amplifying the difference between these two approaches, the simulated spectra are generated by varying the value of the spread angle θ_s from 0° to 180° (The effect of the spread angle will be explained in the next paragraph). It is worth mentioning that there is a peak at around 1.5 MeV in the experimental spectra. It is due to an ^{16}O (^{4}He, ^{4}He) ^{16}O elastic scattering resonance for He ions with energy 3.038 MeV [226], which has not yet been implemented in the code.

Firstly, the simulated spectra from the two approaches exhibit similar trends with varying θ_s. With a higher value of θ_s, the fraction of the yield in the low energy region is higher. Note that the yields are normalized, and thus we are comparing the fraction of the yield in different energy regions (the absolute yield in the whole spectrum, actually, decreases with a higher θ_s.). It can be explained by the fact that, with a higher θ_s, more ions would have a larger angle between the initial direction of the backscattered virtual ion and the direction towards the detector center. For these ions (if they are detected), more elastic collisions are required to change their moving direction to the direction pointing to the detector, when these ions leave from the target surface. Thus, their trajectories are more zigzagged, and eventually they would lose more energy. Nonetheless, the simulated spectra obtained from the TRIM-based approach clearly better fit the experimental one compared to the spectra obtained from the original approach, no matter which value of θ_s is used. These two approaches use different models for both the FFP and impact parameter. Then, the next step is to determine if the difference results from one or the other parameter, or if a specific combination is required. In the following, the spread angle will always be set to 75°.

Let us start with evaluating the role of the different FFP models. This goal can be achieved by comparing the spectra obtained from the TRIM-based, ASD1 and ASD2 approaches, which use the same impact parameter model (TRIM-exponential), but use the energy dependent, random sampling and fixed FFP models, respectively. It can be found that the spectra from these three approaches are basically the same and fit well the experimental one. Hence, we can conclude that all the FFP models used are valid. The only exception is that there appears an unphysical peak on the spectrum obtained

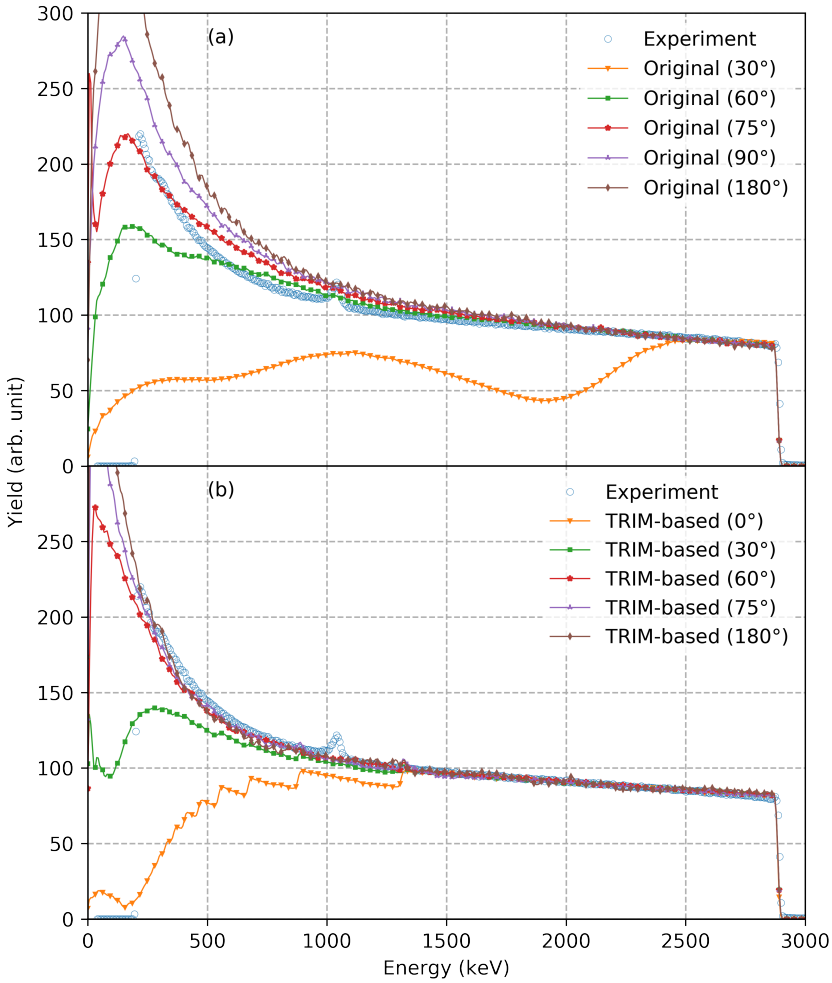

Figure 3.8 – RBS/C spectra of 3.085 MeV He ions on an UO_2 crystal in random directions. Open circles represent experimental spectra. Solid lines with markers represent simulated spectra using (a) the original approach and (b) the TRIM-based approach. In the legend are given the values of the spread angles. (Figure source: Jin et al., Model. Simul. Mat. Sci. Eng., 2020. [225])

from the TRIM-based approach. It can be attributed to the fact that a 5° variation of the moving direction at the end of the FFPs in the energy dependent model is too big compared to the variation in the other two FFP models. This mechanism can also be viewed from the spectrum in Fig.3.8 obtained from the TRIM-based approach with a 0° of spread angle. The spectrum appears to be stepwise in the low energy region. Each step could be attributed to the abrupt change of the ion moving direction by 5°. Actually, the unphysical peak sits on top of the first step counted from the high energy side.

Now, our attention can be focused on the impact parameter model. By comparing the spectra obtained from the original and ASD1 approaches shown in Fig.3.9, we can find that, indeed, the TRIM-exponential model can generate a better spectrum in terms

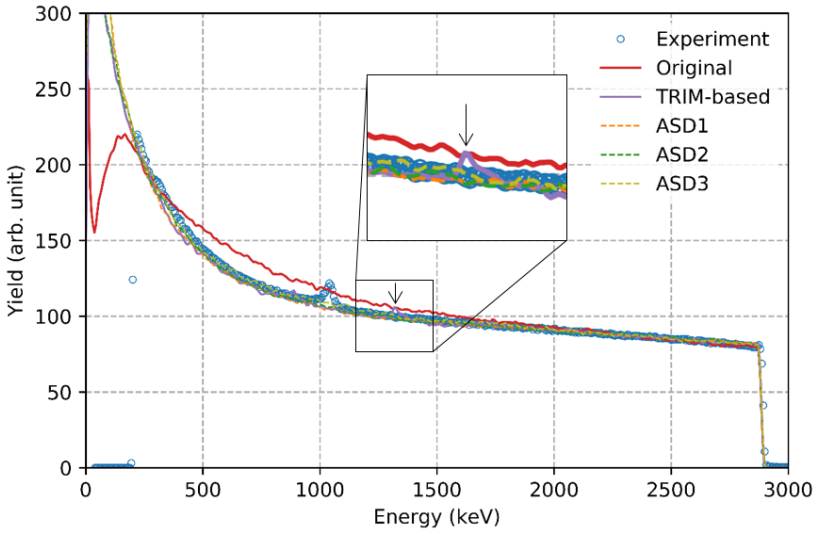

Figure 3.9 – RBS/C spectra of 3.085 MeV He ions on an UO_2 crystal in the random configuration. Open circles represent the experimental spectrum. Solid lines represent simulated spectra using all five approaches listed in Table I. The inset shows an unphysical peak in the simulated spectrum obtained from the TRIM-based approach. (Figure source: Jin et al., Model. Simul. Mat. Sci. Eng., 2020. [225])

of the fitting quality compared to the original fixed-volume. In contrast, the comparison of the spectra obtained from the ASD2 and ASD3 approaches indicates that the effect of the TRIM-exponential and modified fixed-volume models are the same in the current simulation conditions. Although the PDFs of the TRIM-exponential and modified fixed-volume models are different in the high impact parameter region, as shown in Fig.3.7, the ion trajectories are mainly decided by the collision events with small impact parameters. However, the PDF of the original fixed-volume is different from the other two models, even in the small impact parameter region. Even if the spectrum obtained from the original fixed-volume model can fit the experimental one in the high energy region, the discrepancy can be accumulated with the penetration of ions into deeper depth, which eventually leads to a significant deviation of the generated spectra from the experimental one. Therefore, we can conclude that the improvement of the RBS/C random spectrum can be achieved by implementing the TRIM-exponential or modified fixed-volume model for the selection of impact parameters in the amorphous slowdown process. In the following, we will use the TRIM-based approach for further simulations.

3.2.2 Target atomic thermal vibrations

Before we try to improve the quality of the simulated RBS/C aligned spectra, we want to address some issues indirectly affecting these latter, which are, on the one hand (in this section), the definition of the target atomic thermal vibrations, and on the other hand (in

the next section), the divergence of the incident beams. The 1D rms value of the atomic thermal vibration magnitude u_1 can have an influence on the aligned spectra by affecting the nuclear encounter probability given in Eq.(3.2), as well as the trajectory of incident ions. Originally, the value of u_1 was calculated according to the Debye theory:

$$u_1 = (\frac{3\hbar^2}{k_B})^{1/2} \frac{(T/m)^{1/2}}{T_D} \tag{3.8}$$

where $\hbar$ is the reduced Planck constant, k_B is the Boltzmann constant, T is the target temperature, T_D is the Debye temperature and m is the mass of the target atoms. Eq.(3.8) is derived from an analytical approximation, which is valid at high temperatures (i.e., $T \gtrsim T_D$) [227]. Incidentally, Eq.(3.8) can be rearranged to give a relation involving the energy of a vibrating atom obtained by different ways. The Debye temperature is related to the maximum frequency, ω_m, of the vibrating atom as follows [228]:

$$T_D = \frac{\hbar}{k_B} \omega_m \tag{3.9}$$

For the simulations using UO_2, the T and T_D values are set to 285 K and 614 K, respectively [229]. The corresponding magnitudes for U and O atoms are listed in Table.II, which are 2.2 pm and 8.5 pm, respectively.

Within the Debye theory, there is no possibility to decouple the atomic thermal vibration magnitudes of two elements of a binary compound, as in UO_2 for instance. Yet, this option should be available, as it is required in UO_2. So we introduced this possibility in the new version of the code, and now let users be able to input the value of u_1 for each element in order to increase the flexibility, and accuracy of the code. Such parameters can be determined from experiments. According to the temperature factor given in Eq.(2.33) measured from neutron diffraction experiments at room temperature, the values of u_1 for the U and O atoms are 6.9 pm and 8.5 pm, respectively [195]. According to angular scans performed in RBS/C experiments, the values of u_1(U) and u_1(O) are determined to be 6.5 pm and 9 pm, respectively [230]. One can note that the discrepancy with the values derived from the Debye theory is large for U atoms, which are contributing the most to the basckscattering signal.

The aligned RBS/C spectra of 3.085 MeV He ions on an <011>-oriented UO_2 pristine crystal are presented in Fig.3.10, in which the u_1 values of simulated spectra (lines) are determined from the Debye theory, and from neutron diffraction and RBS/C experiments. (Note that, in this section, we do not intend to fit the experimental aligned spectra. We only want to exhibit that the effect of thermal vibration magnitudes is significant.) It can be found that, obviously, the simulated spectra using thermal vibration magnitudes

Table II – 1D rms thermal vibration magnitudes of U atoms u_1(U) and O atoms u_1(O) in UO_2

	u_1(U) (pm)	u_1(O) (pm)
Debye theory (analytical approximation)	2.2	8.5
Neutron diffraction experiments (the temperature factor)	6.9	8.5
RBS/C experiments (angular scans)	6.5	9

obtained from the neutron diffraction and RBS/C experiments bear great similarity, and the simulated spectrum using thermal vibration magnitudes derived from the Debye theory is inevitably characterized by a lower yield. The main reason is that the u_1(U) derived from the Debye theory is significantly lower than those from experiments. Even if a numerical method is used to calculate u_1 according to the Debye theory [227], the results (u_1(U) = 2.3 pm, u_1(O) = 9.0 pm) are still similar to those derived from the analytical approximation. Then the reason could be attributed to the fact that the Debye theory may not work for some compound crystals [216]. In the following, we will use the u_1 values derived from RBS/C experiments.

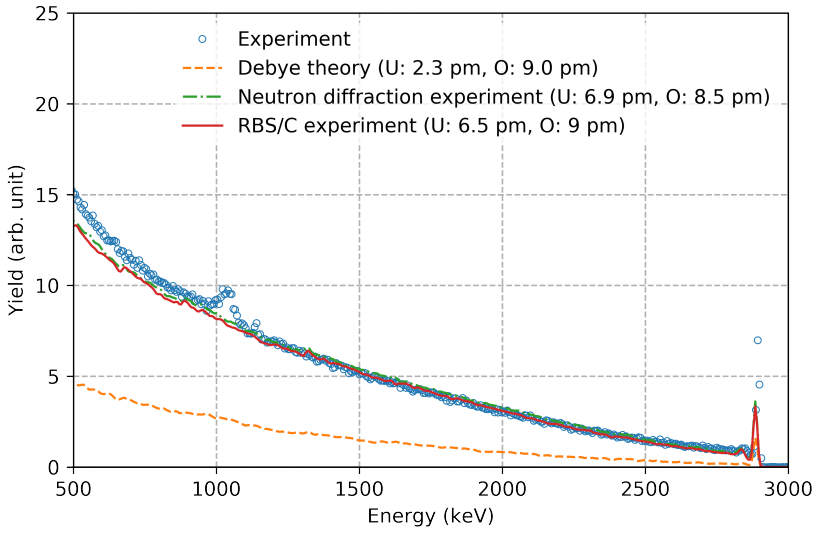

Figure 3.10 – RBS/C spectra of 3.085 MeV He ions on an <011>-oriented UO_2 pristine crystal in the aligned configuration. Open circles represent experimental spectra. Lines represent simulated spectra, for which target atomic thermal vibration magnitudes are obtained from different methods. (Figure source: Jin et al., Model. Simul. Mat. Sci. Eng., 2020. [225])

3.2.3 Incident ion beam divergence

The implementation of an incident ion beam divergence (IBD) description in a simulation code is utilized to take into account both the divergence of ion beams emitted from the accelerator and the target surface disorder (which can affect the ion trajectories). In the original approach, the directions of incident ions are uniformly distributed in a given small solid angle. In spherical coordinates, as shown in Fig.3.4, the distribution of the direction along the azimuthal angle ϕ_n is uniform, and the distribution along the polar angle θ_n follows a PDF function, $P_A(\theta_n)$, as given below:

$$P_A(\theta_n) = \frac{\sin\theta_n}{1-\cos\theta_n^m} \; for \; 0 \leqslant \theta_n \leqslant \theta_n^m \tag{3.10}$$

where θ_n^m is a maximum polar angle set by users. In the following, this type of IBD will be denoted as IBD-A.

It is of interest to consider what is the spatial distribution of the ions on a target surface in front of the ion source. If we assume that incident ions are emitted from a point source and the degree of divergence is small, then the PDF function of the spatial distribution of these ions on a target surface, $P_A(x,y)$, can be expressed as follows:

$$P_A(x,y) = \frac{1}{2\pi d_t^2(1-\cos\theta_n^m)} \; for \; |x| < d_t\theta_n^m \; and \; |y| < d_t\theta_n^m \tag{3.11}$$

where $P_A(x,y)$ is expressed in 2D Cartesian coordinates with the x and y axes in the target surface plane, and d_t is the distance between the ion source and the target surface [225]. In Fig.3.11.a, the green dots represent the angular distribution of ions generated by the code, and the red line is plotted according to Eq.(3.10), in which the θ_n^m is set to 0.12°. By setting the d_t to 5 cm, the 2D spatial distribution of ions on the target surface is presented in Fig.3.11.b, in which the intensities per area are color coded. The blue dots in Fig.3.11.c represent the probability density of ions distributed along a region near $y = 0$ on the surface, which can be well fitted by Eq.(3.11) (orange line).

Alternatively, it may be intuitive to let the angular distribution of ions have a Gaussian distribution as follows:

$$P_B(\theta_n) = \frac{2}{\sqrt{2\pi\sigma_1^2}} e^{-\frac{\theta_n^2}{2\sigma_1^2}} \; for \; \theta_n \geqslant 0 \tag{3.12}$$

where σ_1 is the standard deviation of the Gaussian distribution. Its corresponding spatial

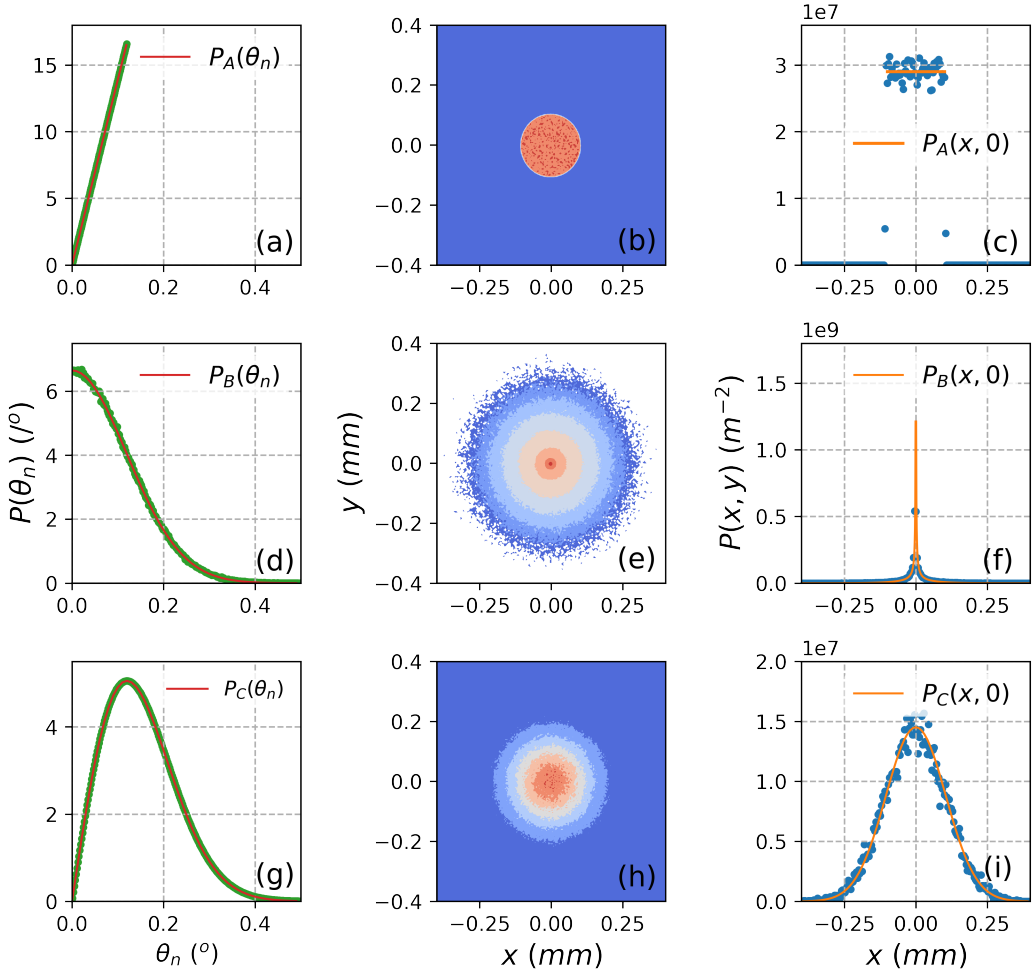

Figure 3.11 – Distributions of incident ions with different IBD types (a) The PDF of angular distribution of incident ions generated by the code using IBD-A is represented by the green dots, and the analytical function $P_A(\theta_n)$ is represented by the red line; (b) The intensity of ions (IBD-A) distributed on the target surface is color coded; (c) A sampling is performed along a narrow region where $y = 0$ on the target surface (IBD-A), and the calculated probability density per area is represented by the blue dots. The analytical function $P_A(x, 0)$ is represented by the orange line; (d-f) The corresponding distributions of ions using the divergence type of IBD-B; (g-i) The corresponding distributions of ions using the divergence type of IBD-C. The characteristic angles of IBDs (i.e., θ_n^m, σ_1 and σ_2) are set to 0.12°, and d_t is set to 5 cm. (The intensity map in (e) is represented in a logarithmic scale.)

distribution can be calculated as:

$$P_B(x, y) = \frac{1}{\pi d_t \sqrt{2\pi\sigma_1^2(x^2 + y^2)}} e^{-\frac{(x^2+y^2)}{2\sigma_1^2 d_t^2}} \tag{3.13}$$

In the following, this type of IBD will be denoted as IBD-B. By setting σ_1 to 0.12° and using the same d_t used in IBD-A, the angular distribution of IBD-B is given in Fig.3.11.d.

Its spatial distribution shows a peak at the center which quickly diminishes in the nearby regions as shown in Fig.3.11.e. Since the peak is too high, the intensity is color coded in a logarithmic scale. The sampling along $y = 0$ is given in Fig.3.11.f.

Another type of angular distribution can be set to have a Rayleigh distribution as follows:

$$P_C(\theta_n) = \frac{\theta_n}{\sigma_2^2} e^{-\frac{\theta_n^2}{2\sigma_2^2}} \; for \; \theta_n \geqslant 0 \tag{3.14}$$

where σ_2 is the scaling factor of the Rayleigh distribution. In the following, this type of IBD will be denoted as IBD-C. One interesting property of IBD-C is that its spatial distribution on the target surface would show a 2D Gaussian distribution, which resembles experimental measurements [231], as follows:

$$P_C(x, y) = \frac{1}{2\pi\sigma_2^2 d_t^2} e^{-\frac{(x^2+y^2)}{2\sigma_1^2 d_t^2}} \tag{3.15}$$

By setting σ_2 to 0.12° and using the same d_t used in IBD-A, the PDF of the angular distribution of IBD-C would increase from 0 at 0° and then decrease after reaching a maximum value as shown in Fig3.11.g. The spatial distribution is much smoother, according to Fig3.11.h, compared to that of IBD-B. The sampling dots (measured along $y = 0$) presented in Fig3.11.i indicate that the spatial distribution indeed follows a Gaussian distribution given in Eq.(3.15).

A comparison of RBS/C aligned spectra (lines) generated by the code using different IBDs is presented in Fig.3.12. (Note that we only want to exhibit the effect of IBDs, and do not intend to fit the experimental spectra here.) It can be observed that when the characteristic angles, i.e., θ_n^m, σ_1 and σ_2, are set to a same value (0.12°), the spectrum of IBD-C is the highest in the low energy region, whereas the spectrum of IBD-A is the lowest. Thus, it is important to know what kind of IBD types are used when simulated spectra from different codes are compared. The simulated spectra in the high energy region are roughly the same, which indicates that the difference in the low energy region occurs due to the accumulation of discrepancies along the ion path. Nonetheless, it is still possible to generate similar spectra by using different IBDs. In Fig.3.12, the simulated spectra can have roughly the same yields by increasing θ_n^m to 0.18° and decreasing σ_2 to 0.09°. Since many simulations had been performed by using the IBD-B before the introduction of the IBD-C into the code, in the following, simulated spectra are generated by using IBD-B with $\sigma_1 = 0.12$ °.

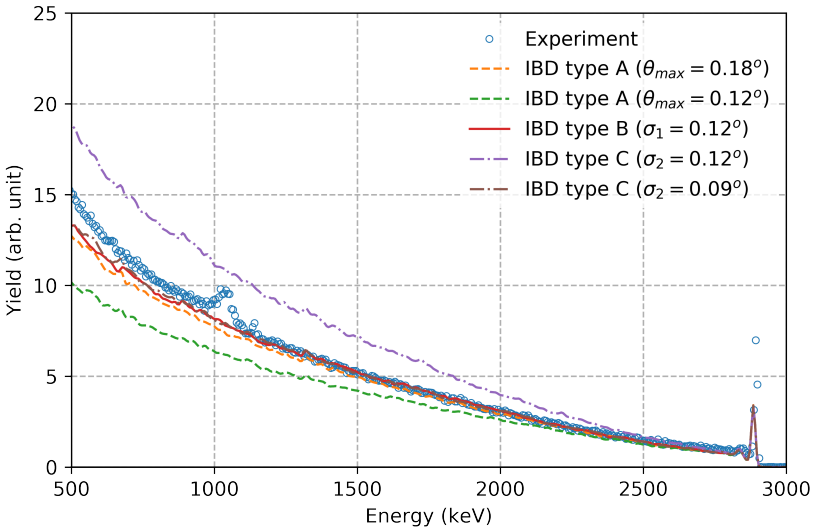

Figure 3.12 – RBS/C aligned spectra of 3.085 MeV He ions on an <011>-oriented UO_2 pristine crystal obtained from the experiment (open circles) and from the simulations (lines) using different types of IBDs. (The θ_{max} in the figure caption is θ_n^m.) (Figure source: Jin et al., Model. Simul. Mat. Sci. Eng., 2020. [225])

3.2.4 Simulation of aligned spectra

The aligned spectra are necessarily produced in channeling configuration, which are highly sensitive to the trajectories of ions. As mentioned above, in this code, the ion trajectories are decided in elastic collision events. Thus, the procedure for the search of collision partners plays a crucial role. One important parameter in the search process is the maximum impact parameter b_{max}, as shown in Fig.3.1. Note that we are dealing here with the impact parameter in the search process of collision partners in a channeling configuration (for random spectra, the amorphous slowdown process is used). The larger b_{max} is, the more atoms will influence the search process. Originally, b_{max} was set to the value of r_v which equals to 1.482 Å in UO_2.

It may be intuitive to set b_{max} to r_v. However, this option could lead to underestimating the real influence of the target atoms on the moving ions. As shown in Fig.3.13, the blue and orange circles are located at the positions of U and O atoms in the (011) plane of UO_2, respectively. The radius of the circles is equal to r_v. It can be found that there are some regions not affected by any atom. When an ion, with a moving direction perpendicular to this plane, penetrates through the plane in the non-affected regions, it will find no collision partner and feel no force from nearby atoms. Thus, it is of interest to consider how the aligned spectra change with a larger value of b_{max}.

In a new method we propose for the search of collision partners, we use a minimum interatomic potential, V_{min}, to decide the value of b_{max}, instead of setting a fixed value

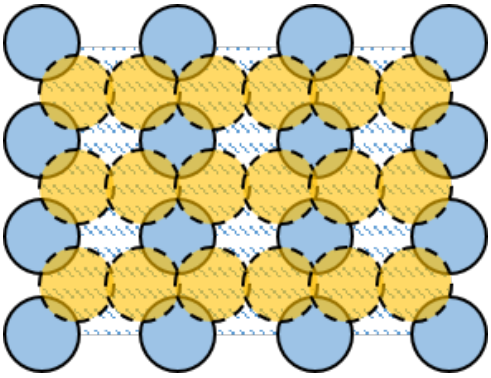

Figure 3.13 – Potential collision partners on the (011) plane of UO_2. The blue circles represent U atoms, and the orange circles represent O atoms. The radius of circles is equal to r_v.

for b_{max}. V_{min} is described by the ZBL universal potential [59], and the derivation of b_{max} from V_{min} is achieved by using Newton's method [232]. One advantage of this method is that b_{max} will have different values with different elements, which is more reasonable for compounds. The value of b_{max} decreases with a higher V_{min} value, as shown in Fig.3.14. When V_{min} is smaller than 2 eV, both the b_{max} values for U and O atoms are larger than the fixed r_v.

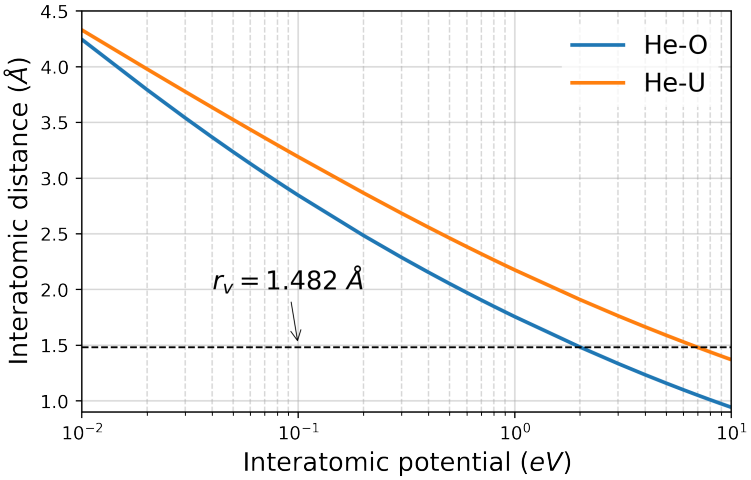

Figure 3.14 – Interatomic distances derived from the ZBL universal potentials. The blue and orange lines represent the distances between He and O and between He and U atoms, respectively. The black dotted line indicates the value of r_v in UO_2.

The effect of b_{max} on the yield of aligned spectra is presented in Fig.3.15. The simulated spectrum using the original method ($b_{max} = r_v$) is denoted as R_a, and the simulated spectra using the new method are obtained by setting different values for V_{min}. When the backscattered energy is high, the discrepancy between the different spectra is not

significant. As the energy decreases, the spectra with smaller V_{min} (higher b_{max}) exhibit a higher yield than those with higher V_{min} (smaller b_{max}). This finding indicates that, by taking into account the influence of more atoms, the ion would have a higher ability to break through atomic channels. The best fit to the experimental spectrum is achieved by setting V_{min} to 0.3 eV.

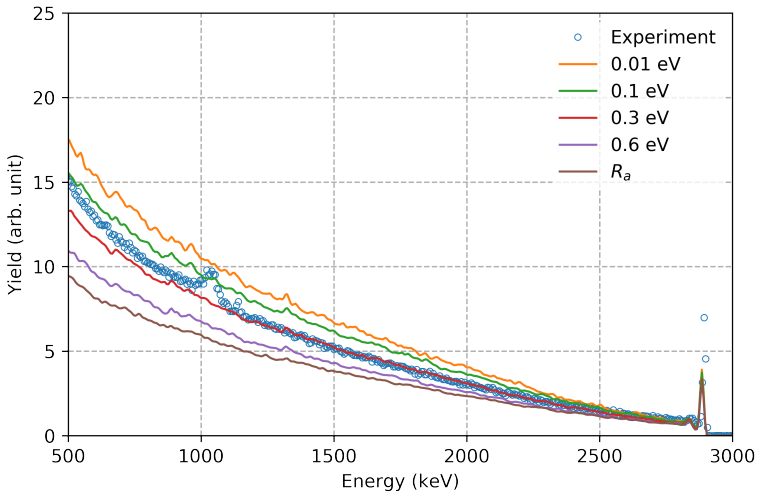

Figure 3.15 – RBS/C aligned spectra of 3.085 MeV He ions on an <011>-oriented UO_2 pristine crystal with different b_{max}. Blue circles represent the experimental spectra. Lines represent the simulated ones, in which the values of b_{max} are determined by V_{min} except the one denoted by R_a (using the fixed value r_v). (Figure source: Jin et al., Model. Simul. Mat. Sci. Eng., 2020. [225])

Finally, on the one hand, the incorporation of V_{min} provides a method to fit better experimental results; on the other hand, this brings an additional free fitting parameter which is difficult to determine without a fastidious trial and error process. One problem is that with a lower value of V_{min}, the increase of the aligned yield does not show a sign of saturation. One possible reason could be related to simultaneous collisions that are not taken into account. Robinson [101] has shown that disregarding this kind of collisions could lead to a larger deflection angle. Although the BCA algorithm is meant for binary collisions, it is necessary to consider multiple collisions at the same time in some conditions. One condition is when an ion moves through a midpoint between two atoms. Another condition is that, as shown in Fig.3.1, the target atom T_1 is selected as the collision partner, but an atom T_2 may be closer to the incident ion. Thus, before the ion collides with T_1, it is already strongly affected by T_2. This problem is handled in MARLOWE by introducing a parameter [101] which can be called the projection interval $\triangle\xi$, as shown in Fig.3.1. If the difference between ξ_i and ξ_1 is smaller than $\triangle\xi$, then the target atom T_i will participate in a simultaneous collision with T_1. This approach has been tested in RBSADEC. It shows that, with a higher $\triangle\xi$, the yield of simulated

spectra will be smaller and experimental spectra can be fitted by adjusting this parameter. However, the author of MARLOWE has found a flaw in the algorithm of simultaneous collisions. Thus, a new algorithm with a correction for the simultaneous collisions should be incorporated into the code in the future [233].

3.3 Discussion and summary

In this chapter, we presented several new approaches that can be used to increase the applicability and flexibility of the RBSADEC code. The new features are important for a broader usability of the code, but they are also mandatory for us, as they will allow to generate satisfactory RBS/C spectra for our case-study that is the use of 3.085 MeV He ions on an <011>-oriented pristine UO_2 crystal. These new approaches were introduced to improve the treatment in the amorphous slowdown process, which contains different models for the calculation of the FFP and of the impact parameter. In terms of the impact parameter models (which can have critical effects on the shapes of RBS/C spectra), the TRIM-exponential and modified fixed-volume models should be preferred. In terms of the FFP models, all three proposed models can generate satisfactory results. The energy dependent model can be selected for the purpose of quick simulations (being aware that some unphysical peaks can appear). By choosing a relatively large value, the fixed model can also provide relatively quick simulations, and without the generation of unphysical peaks. However, an ion having a fixed length of FFP regardless of its energy may not be physically sound, which can lead to problems when the fixed value is too high. Thus, a more rigorous simulation can be achieved by using the random sampling model.

Comparisons of simulated aligned spectra show that the Debye theory may not be suited for the calculation of atomic thermal vibration magnitudes for targets containing multiple elements. In this case, it is better to input the vibration magnitude, obtained from experiments, for each element, separately. The IBD type can also have non-negligible effects on the aligned spectra. While it is difficult to determine which type should be favored without a detailed knowledge of the ion beam characteristics, it is important to use the same type of IBD when results from different codes are cross-checked (or, equivalently, two different types can be used if otherwise impossible, but correct characteristic parameters of beam distributions must be used). In case that the simulated aligned spectra can not satisfactorily fit experimental results, users can decide to adjust the minimum interatomic potential that has an influence on the simulated spectra by affecting the search of collision partners.

Chapter 4

Combination of RBS/C and XRD with molecular dynamics to investigate radiation effects in materials

In this chapter, we will investigate radiation effects in materials by performing coupled XRD and RBS/C simulations. Two types of targets will be studied. For the first type, the targets are UO_2 MD cells with different damage levels, which will be presented in Sec.4.1 and Sec.4.2. The quantity and type of radiation defects in these UO_2 MD cells evolve with the damage level, which gives rise to elastic strain and disordering kinetics. For the second type, the targets are Fe MD cells with model defects, which will be presented in Sec.4.3. From these Fe MD cells, clear insights are expected to be obtained in terms of the response of XRD and RBS/C signals to different types of model defects.

4.1 Simulation methods: UO_2

4.1.1 Simulation of defects

MD simulations are extensively used to study radiation defects. Conventionally, radiation defects in MD cells can be obtained by simulating collision cascades induced by energetic atoms emulating PKAs; subsequently, the overlap of collision cascades can give rise to defect evolution [45, 46, 234]. However, since in MD simulations the timesteps in numerical evaluations need to be small enough to guarantee stable behaviors of atoms with high velocities, this approach consumes significant amount of computational time if high irradiation doses are required. Instead, in this work, radiation defects in MD cells are generated by the Frenkel pair accumulation (FPA) method, which bypasses the simulation of collision cascade by directly introducing stable defects, i.e., Frenkel pairs (FPs). This method has been applied to mimic evolutions of radiation defects in various materials,

including metals [235, 236] and ceramics [47, 55, 237, 238].

MD simulations using the FPA method were performed previously in UO_2 cells at 300 K and 0 pressure. Each cell contains 768000 atoms and has a cubic shape. The side length of a pristine cell is 21.6 nm. The x, y and z axes of the cells are along the [100], [010] and [001] directions, respectively. A Morelon empirical potential was used for the calculations of atomic interactions, which describes well the energies of formation and migration of point defects [239]. Only uranium FPs were created, which is reasonable considering the fact that the behavior of UO_2 under irradiation is primarily controlled by the cation sublattice [240]. Thereby, the damage in the MD cells is represented by the displacements (of uranium atom) per uranium atom (dpU), ranging from 0.01 to 7.85 in a total of 897 MD cells. Every 2 ps, 800 uranium FPs were created, which corresponds to an extremely high dose rate equal to 1.5625×10^9 dpU/s. Since the timescale of the simulation is small, thermal migration of defects is hindered. However, recombinations and evolutions of defects still can proceed through athermal motions of defects induced by elastic interactions [241]. In the following, the dpU generated in these MD cells will be denoted as FPA-dpU. More details about the simulations can be found in ref. [55].

Since the irradiation damage in a sample is usually represented by the dpa level, it is of interest to consider the conversion from dpa to dpU. This conversion, in UO_2, can be calculated by:

$$dpU = \frac{N_t}{N_U}\frac{d_U}{d_t}dpa \tag{4.1}$$

where N_t and N_U are the numbers of total atoms and uranium atoms, respectively, d_t is the total displacements of atoms and d_U is the corresponding quantity only for uranium atoms. While it is clear that the ratio of N_t to N_U is 3, the ratio of d_U to t_t depends on the displacement threshold energies E_d of U and O atoms, which are 40 eV and 20 eV, respectively [242]. According to SRIM Full-Cascade simulations, 1 dpa is equivalent to 0.76 dpU at the position of maximum damage in the irradiations used in the following (20 keV He ions, 500 keV La ions and 500 keV Ce ions on UO_2). The dpU calculated by SRIM (denoted hereafter as SRIM-dpU) is similar to FPA-dpU in the sense that both of them are the ratio of the number of displaced U atoms to the total number of U atoms. Nonetheless, like the calculation using the NRT model as mentioned in Sec.1.3.1, SRIM calculations (for both the Kinchin-Pease and Full-Cascade calculations) tend to overestimate the number of defects, i.e., the stable defects generated by collision cascades in MD simulations [243]. In addition, the FPs introduced in the cells should resemble the so-called freely migrating defects (FMDs), which are defects that become spatially uncorrelated to other defects created in a same collision cascade by escaping the cascade region. It is the FMDs that contribute to the long-term microstructural

evolution [244, 245]. In contrast, a certain fraction of stable defects inside a cascade region would further recombine without contributing to the defect evolution [246]. Thus, we can conclude that SRIM calculations would further overestimate the number of defects as compared to the actual FMDs quantity. This difference on the defect number is one important source of the discrepancy between SRIM-dpU and FPA-dpU, which will have strong implications on the comparison between simulated and experimental results in the following.

4.1.2 Analysis of defects

Although initially only FPs are introduced into the cells, the FPs can recombine or cluster. The latter could lead to changes in the microstructure, as mentioned in Sec.1.3.2. Thus, *ad hoc* characterizations are required to explore the type and concentration of defects that are actually present in damaged cells. For this purpose, we used the OVITO code [112] to visualize and analyze those defects. A Voronoi analysis method [49] was used to calculate the point defect (i.e., vacancies and interstitials) concentration. A dislocation analysis method (DXA) [50, 247] was applied to generate the information related to dislocation types and densities (defined by the dislocation length divided by cell volume).

A quick qualitative insight can be obtained from the visualization of the cells. For example, as shown in Fig.4.1.(a-d), U atoms in a small region of the cells, with damaged levels of 0 dpU (pristine), 0.1 dpU, 0.3 dpU and 3 dpU, respectively, are represented by blue circles. At 0 dpU, all U atoms are registered on regular lattice sites. When the dpU is slightly higher (0.1 dpU), some U atoms are displaced from their original positions, which can be assumed to be point defects. As the dpU level further increases (0.3 and 3 dpU), the original lattice structure becomes severely defective, with atomic rows now highly distorted. Clearly, dislocations are formed, and they are now predominant. The analysis of the cells shown in Fig.4.1.(e-h) indicates the presence of 1/3<111> Frank (blue), 1/6<11-2> Shockley partial (orange) and 1/2<110> perfect (green) dislocations. According to the shape of these dislocations, we can claim that Frank dislocations are loops. It is however difficult to discriminate loops and lines for the perfect dislocations.

A quantitative analysis of the defect concentrations and densities is displayed in Fig.4.2.a and Fig.4.2.b, respectively. The sequence of defect evolution can be decomposed as follows:

1. From 0 to 0.09 dpU, the concentration of both interstitials and vacancies grows roughly at a same speed as a function of dpU, and the dislocation density is negligible.

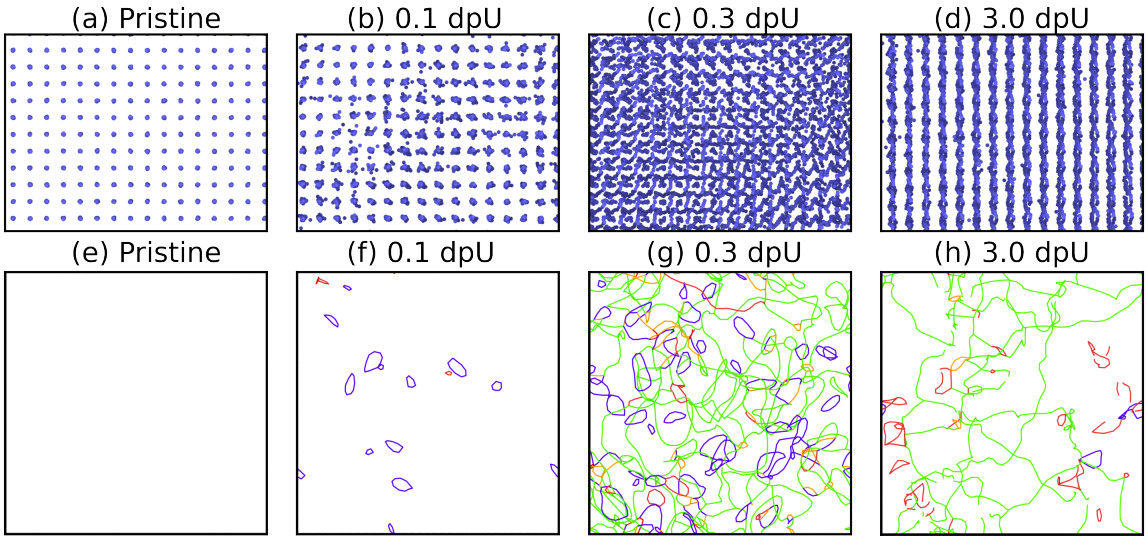

Figure 4.1 – Visualization of U atoms and of dislocations in UO_2 MD cells. (a-d) show U atoms represented by blue circles along the z direction (the visualization thickness is equal to the cell thickness). (e-h) show only dislocations, which includes Frank loops (blue), perfect dislocations (green) and Shockley partial dislocations (orange). (Other types of dislocations, e.g., stair-rod dislocations and ill-defined dislocations, are represented by red lines.)

2. From 0.09 to 1 dpU, while the concentration of vacancies keeps increasing, the concentration of interstitials drops and gradually approaches a steady, low value at the end of this stage. At the same time, dislocations start to emerge, which indicates that they are of interstitial type. Among the different dislocations, those that form initially are Frank loops, and Shockley partial and perfect dislocations are formed shortly after the onset of Frank loops. While the density of Frank loops reaches a maximum at around 0.25 dpU, the density of perfect dislocations surpasses that of Frank loops and reaches a maximum at around 0.4 dpU, which can be attributed to the fact that Frank loops can transform into perfect dislocations by reacting with Shockley partial dislocations [127]. From the direct visualization of the dislocations, the perfect dislocations are initially composed of dislocation loops, but then a mixture of loops and lines is observed at the end of this stage. However, at this stage, it is difficult to provide an exact dpU at which the transition of perfect dislocation loops to lines occurs due to the difficulty of separating loops and lines.

3. Above 1 dpU, both concentrations of vacancies and interstitials maintain relatively steady values, but the quantity of vacancies is much higher than that of interstitials. Perfect dislocations become the dominant dislocation type and their density gradually reaches a steady value. The overall steady values of defect

concentrations and densities indicate that a dynamical equilibrium of defect creation and recombination (or annihilation) is attained.

This sequence of defect evolution determined from the UO_2 MD cells is in line with the results obtained from both experiments and simulations [55, 131, 132, 248]. These qualitative and quantitative studies of defect characteristics will serve in the following as the basis for connecting the type and quantity of defects with the XRD and RBS/C signals.

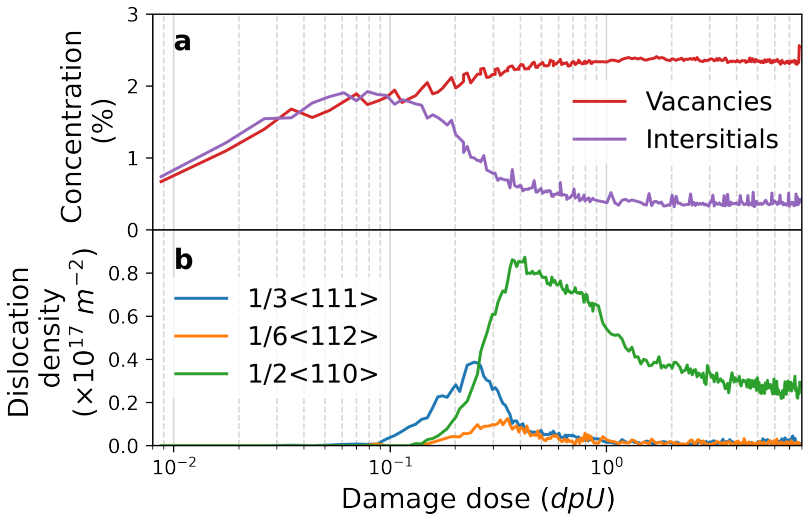

Figure 4.2 – Defect quantities in UO_2 MD cells as a function of dpU. (a) Concentrations of point defects, including vacancies and interstitials; (b) Densities of dislocations, including Frank loops, Shockley partial and perfect dislocations. (Figure source: Jin et al., Acta Mater., 2020 [249])

4.1.3 XRD and RBS/C methods

We used the method mentioned in Sec.2.2.3 to generate XRD signals from the MD cells. Three sets of 3D intensity distributions were calculated, using Eq.(2.36), in the vicinity of the 004 Bragg reflections, along the [001], [010] and [100] directions, respectively. For each direction, for example, along the [001] direction, two 2D RSMs were obtained by integrating the 3D intensity along the x and y directions, respectively. By this way, two sets of elastic strains and DW factors, obtained on the yz and xz planes, can be calculated along the [001] direction according to Eq.(2.43) and Eq.(2.44), respectively. Finally, we took the average of these two values. The relative disorder is defined as $1 - DW$. A same procedure was performed for the 3D intensities obtained along the [010] and [100] directions.

Examples of the intensity calculations are presented in Fig.4.3 using the MD cells with damaged levels of 0 (pristine), 0.1, 0.3 and 3.0 dpU. Fig.4.3.(a-d) are the corresponding RSMs obtained by measuring along the [001] direction and then integrating along the y direction. Peaks are represented by black dots, in which the maximum peak is denoted O_1. Units of h and l are reciprocal lattice units (r.l.u). Fig.4.3.(e-h) represent the corresponding intensities measured along h-line where O_1 is located, which provides the information related to the tilt or shear angle of the cells. Fig.4.3.(i-l) represent the corresponding intensities measured along the l-line where O_1 is located, which provides the information related to the elastic strain in the cells. It is clear that intensities at the O_1 in the damaged cells are smaller than that in the pristine one, which indicates higher levels of disorder. The l values of O_1 in the damaged cells are shifted towards smaller values, which indicates positive elastic strain (tensile strain). In the cell with 0.3 dpU, there are two peaks in which the h position of the second peak O_2 is clearly shifted from 0. This phenomenon is a sign that there are sub-crystallites or mosaic structures in which some sub-crystallites are tilted. More detailed studies on the sub-crystallite-like structures in these cells can be found in a forthcoming paper [250], in which both shear strain and rigid rotation of sub-structures are determined. Here, we only emphasize that, since the size of the MD cells is limited, we can expect that the existence of sub-structures would bring anisotropy when the cells are examined from the three (001) directions.

It is worth mentioning that sometimes the location of secondary-peaks found in RSMs cannot be intuitively reflected in 1D spectra measured either along the h or along the l direction. The first reason is that the 1D spectra are measured in the vicinity of the main peak. When secondary-peaks are not in the same h or l-line with the main peak, only parts of their intensities are measured. The second reason is due to the method of selecting the peaks. In addition to the magnitude of peak intensities, it is required that peaks are separated by a minimum distance. In Fig.4.3, this minimum distance is set to 0.051 in reciprocal lattice unit. Thus, coordinates with high intensities inside the range of this minimum distance will not be counted as secondary-peaks.

RBS/C simulations were performed by using the RBSADEC code with the new developments made by us [52, 225]. Periodic boundary conditions were applied to the x and y directions of the cells, while a beam of 3.085 MeV He ions (corresponding to available experimental data) enters into the cells along the z direction. Similar to the XRD simulations, three sets of RBS/C spectra were calculated by setting the z direction along the [001], [010] and [100] directions. Since the presence of defects in damaged cells can induce a change of the cell volume, for every cells along each of the three directions, both random and aligned spectra were calculated. By comparing the yield of the random spectra obtained from the pristine and damaged cells, a normalization

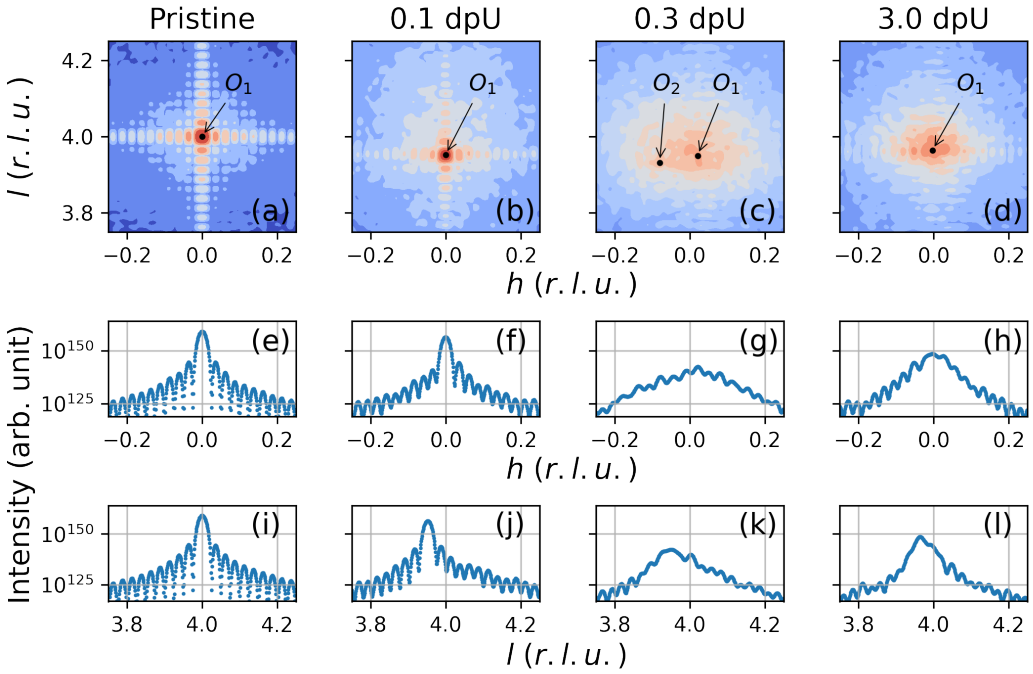

Figure 4.3 – Intensity distributions calculated from UO_2 MD cells. (a-d) 2D RSMs calculated in the vicinity of the 004 Bragg reflections, which are measured along the [001] direction and are integrated along the y direction using the cells with the damaged levels as 0 (pristine), 0.1, 0.3 and 3.0 dpUs, respectively. Peaks are indicated by black dots, in which the maximum one is denoted by O_1. Units of h and l are reciprocal lattice units (r.l.u). The intensities (on a logarithmic scale) are represented in a warm to cold color scale; (e-h) The corresponding intensities measured along the column of h where the maximum peak locates; (i-l) The corresponding intensities measure along the row of l where the maximum peak locates.

factor was obtained and applied to the aligned spectra generated from the damaged cells. According to the developments introduced in Sec.3.2, for the sake of quick calculations, the TRIM-based amorphous slowdown approach was used to describe the trajectories of backscattered virtual ions. The 1D rms values of atomic thermal vibrations were set to 6.5 pm and 9 pm for the U and O atoms, respectively [230]. The incident ion beam divergence was described by the type of IBD-B with the standard deviation angle as 0.12°. The minimum interatomic potential used to determine collision partners was set to 0.05 eV, which was determined by fitting an aligned spectrum generated from a perfect pristine sample calculated by RBSADEC to that calculated by the McChasy code [251]. The relative disorder is calculated according to Eq.(2.10), thus neglecting the effect of dechanneling (This point is justified in Appendix.A).

Examples of RBS/C spectra generated from 3.085 MeV He ions on <001>-oriented UO_2 MD cells are shown in Fig.4.4, in which the damage levels of the cells are 0 (pristine),

0.1, 0.2, 0.3, 1.0 and 3.0 dpU. Both spectra calculated from the random (blue) and aligned (along the [001] direction, orange) configurations are presented. As expected, the yields of aligned spectra obtained from damaged cells are higher than that obtained from the pristine one. The aligned yield calculated from the cell at 3.0 dpU is lower than that at 1.0 dpU, which indicates that some parts of the damaged crystal (in the cell at 3.0 dpU) recovered.

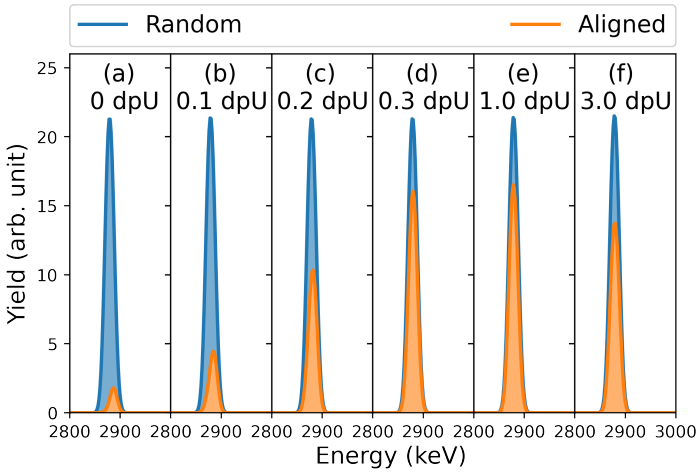

Figure 4.4 – RBS/C spectra generated from 3.085 MeV He ions on <001>-oriented UO_2 MD cells with the damage levels as 0 (pristine), 0.1, 0.2, 0.3, 1.0 and 3.0 dpUs. Blue and orange lines represent the spectra obtained from the random and aligned (along the [001] direction) configurations, respectively.

4.2 Characterization of radiation damage: UO_2

4.2.1 Strain kinetics

Qualitative study

Fig.4.5.(a) presents the elastic strain kinetics as a function of damage dose (dpU) calculated from the XRD simulations on the UO_2 MD cells. The kinetics were calculated along the [001] (blue), [010] (orange) and [100] (green) directions. In order to verify the validity of the simulation-based approach, the results of simulations were compared to experimental results obtained from irradiations of UO_2 crystals with 20 keV He ions [131, 252] and 500 keV Ce ions (see Fig.3-14 in ref. [184]), as shown in Fig.4.5.(b) and (c), respectively. In the experiments, damage levels were originally represented by dpa according to calculations using the SRIM Full-Cascade mode. They can be converted into dpU according to Eq.(4.1). As the dpU increases, the strain kinetics obtained from the simulations exhibits distinct features that shows strong correlations with the defect

evolution in the cells. In the low dpU region, where point defects are dominant, the elastic strain exhibits a rapid buildup. After the onset of Frank loop formation, the strain increases at a slower rate and reaches a maximum value (1.9 %) at around 0.28 dpU. Then, it starts to decrease, which coincides with the moment when perfect dislocations become the major type of defects. The strain measured from the three different directions starts to diverge after the peak, which can be attributed to the anisotropy of the cell structures induced by the formation of sub-crystals, as mentioned in Sec.4.1.3.

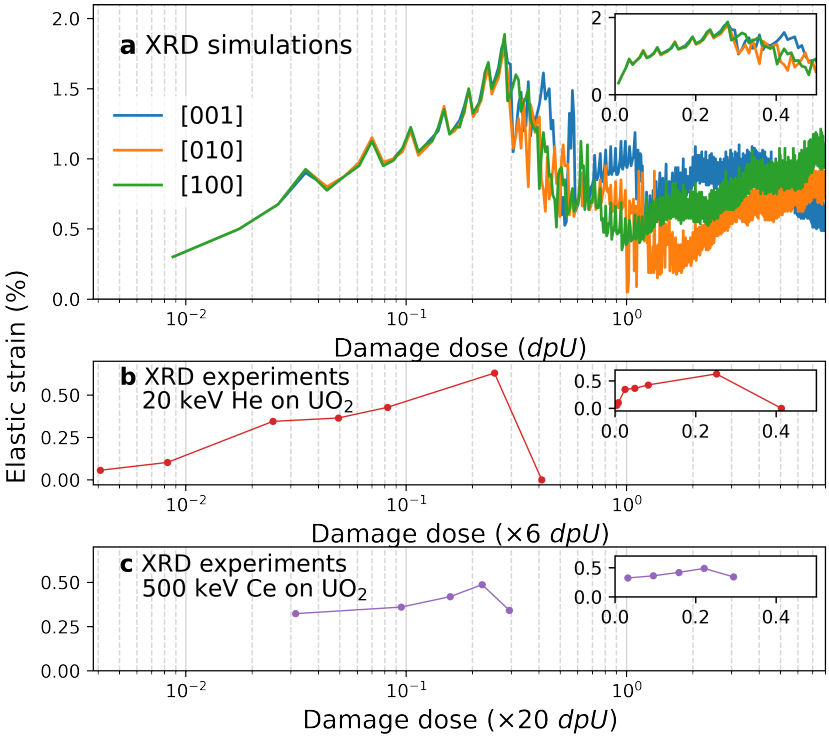

Figure 4.5 – Elastic strain kinetics as a function of dpU obtained from (a) the XRD simulations on the UO_2 MD cells, (b) XRD experiments of 20 keV He ions on UO_2 crystals and (c) XRD experiments of 500 keV Ce ions on UO_2 crystals. In the simulations, elastic strains were calculated along the [001] (blue), [010] (orange) and [100] (green) directions of MD cells. In the experiments, elastic strains were measured along <001> directions. (Insets use a linear scale for the x axis.) (Figure source: Jin et al., Acta Mater., 2020 [249])

Comparing simulated and experimental results, we can find two main discrepancies. The first one is that the maximum value of the simulated strain (1.84 %) is significantly higher than those measured from the experiments (0.63 % for 20 keV He ions and 0.49 % for 500 keV Ce ions). One plausible reason can be attributed to a sheer difference between the dpU production rates in simulations and experiments. The dpU production rate in experiments can be calculated by using SRIM. Fig.4.6 shows the depth profiles of displacements calculated for the two experimental conditions by using the Full-Cascade

mode of SRIM. By extracting the number of displacements, N_{SRIM}, from Fig.4.6, the dpa production rate, K_r, can be calculated by:

$$K_r = \frac{N_{SRIM}\phi_{ion} \times 10^8}{N_a} \tag{4.2}$$

where ϕ_{ion} is the flux of incident ions and N_a is the target atomic density. For the experiments with 20 keV He ions and 500 keV Ce ions on UO_2, the quantities of ϕ_{ion} are taken as 1×10^{12} cm^{-2}s^{-1} [252] and 5×10^{11} cm^{-2}s^{-1} [184], respectively. By considering the relation between dpU and dpa given in Eq.(4.1), the dpU production rates at the position of maximum damage in UO_2 irradiated by 20 keV He ions and 500 keV Ce ions are 5.2×10^{-5} dpU/s and 3.4×10^{-3} dpU/s, respectively, which are much smaller than that in the MD cells (1.5625×10^9 dpU/s). It is suggested that the dislocation density is proportional to $K_r^{1/6}$ [55], then the dislocation density in the MD cells would be much higher than that in the experiments.

The second discrepancy is that it takes around 6 times and 20 times higher dpU values for the onset of defect evolution in the experiments using the He and Ce ions, respectively. This is due to the different nature of SRIM-dpU and FPA-dpU: SRIM calculations tend to overestimate the number of stable defects produced by collision cascades; and some stable defects would further recombine without contributing to the defect evolution. It is worth mentioning that the overestimation of SRIM calculations of the stable defect number would be smaller when the PKA energy is smaller [108, 253]. Thus, the defect evolution in the experiments using 20 keV He ions occurs earlier compared to that using 500 keV Ce ions. In addition, it is reasonable to assume that the high defect density in the MD cells also accelerates the transformation of defects. Despite these two discrepancies, it can be observed that the strain obtained from the experiments exhibit a quick growth in the low dpU region and then approaches to maximum values with a lower speed when dpU is higher, which agrees qualitatively with the simulated results.

Quantitative study

Since we already obtained the quantities of the various defects by analyzing the MD cells, it is feasible to go beyond the qualitative description of the build-up of strain by decomposing the strain kinetics into components associated with each type of defects. It is generally considered that the elastic strain induced by point defects is proportional to their relaxation volume [124, 193]. For dislocation loops, both the density and size of the loops affect the elastic strain [254, 255]. However, in the MD cells, the geometries of the loops are not well characterized in terms of size, lying planes, etc. Therefore, for the sake of convenience, we assume a linear relationship between the quantity of defects and the

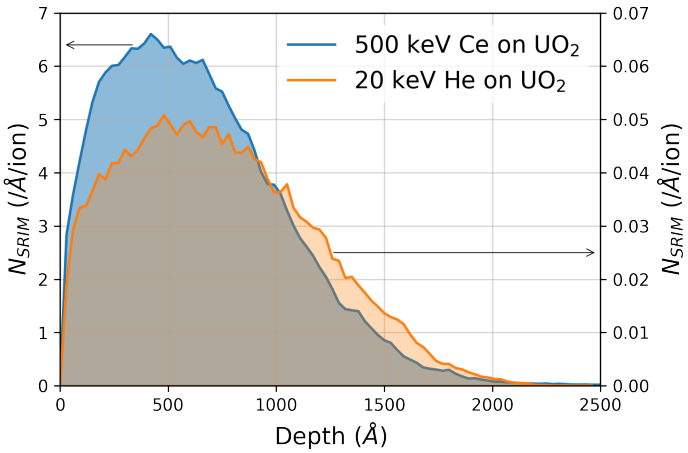

Figure 4.6 – Depth profiles of displacements calculated for 500 keV Ce ions on UO_2 (blue, left y axis) and for 20 keV He ions on UO_2 (orange, right y axis).

induced strain. Nonetheless, we will demonstrate that this simple assumption is able to give satisfactory results. The total elastic strain, ε_{def}, can be calculated by:

$$\varepsilon_{def} = \frac{1}{3}[C_V \frac{V_V^{rel}}{\Omega} + C_I \frac{V_I^{rel}}{\Omega} + (S_F \rho_F + S_p \rho_p)] \tag{4.3}$$

where C_V and C_I are the concentrations of vacancies and interstitials, respectively, V_V^{rel} and V_I^{rel} are the relaxation volumes expressed in atomic volume unit Ω for vacancies and interstitials, respectively, ρ_F is the density of Frank loops and ρ_p is the density of perfect dislocations; the terms S_F and S_p, which have the dimension of a surface, are the proportionality factors between the concentration of Frank loops and perfect dislocations, and the corresponding strain, respectively.

The decomposition of the elastic strain is performed by fitting a simulated kinetics which is averaged over those calculated along the three <001> directions. Since we are using multiple variables, i.e., the parameters in Eq.(4.3), to fit only one kinetics, it is possible that different sets of parameters can generate similar results. In addition, there is a controversy regarding the sign of V_V^{rel} in the literature [256, 257]. Thus, we fitted the simulated strain kinetics using both positive and negative V_V^{rel}, as shown in Fig.4.7, by using a non-linear least squares fitting algorithm available in SciPy [258]. The fitting parameters are listed in Table I. Fig.4.7 shows that the simulated kinetics can be fitted well by using both sets of parameters, except in the high dpU region (above 1 dpU).

In order to further compare the two fits, we calculated the root-mean-square deviation (RMSD) for each condition. It shows that the fit with a positive V_V^{rel} (0.4 Ω) has a better quality than that with a negative V_V^{rel} (-0.2 Ω). This is in line with the result of MD simulations using the same Morelon empirical potential, which generates an average

relaxation volume equal to 0.6 Ω. Now, by only considering the case with a positive V_V^{rel}, the relaxation volume for interstitials is found to be 1 Ω. The proportionality factors for Frank loops and perfect dislocations are 75 Å and 10 Å, respectively. In addition, it can be observed that the peak of the strain kinetics coincides, in terms of dpU, with that of Frank loops. These results indicate that the relaxation of strain is related to the transformation of Frank loops into perfect dislocations. The different contributions from these two types of dislocations could be induced by their different Burgers vectors. While a random spatial distribution of perfect dislocations can generate a vanishing average Burgers vector, this is not the case for the Frank loops. Thus, Frank loops are able to produce homogeneous (elastic) strain, whereas perfect dislocations rather give rise to heterogeneous (local) strain. The low strain induced by perfect dislocations indicates that although we are unable to distinguish between perfect loops and lines, it has probably no consequences (at least for the strain parameter).

Table I – Relaxation volumes, V^{rel}, of point defects and strain constants, S, of dislocations for: a vacancies with a positive relaxation volume and **b** vacancies with a negative relaxation volume. The errors are obtained from the non-linear least squares fitting algorithm.

	V_V^{rel} (Ω)	V_I^{rel} (Ω)	S_F (Å^2)	S_p (Å^2)
a	0.4 ± 0.1	1.0 ± 0.1	75.1 ± 3.5	10.3 ± 2.4
b	-0.2 ± 0.1	1.6 ± 0.1	77.3 ± 3.5	25.0 ± 2.4

4.2.2 Disordering kinetics

Qualitative study

The disordering kinetics of the MD cells were determined by using XRD and RBS/C simulations, as shown in Fig.4.8.(a) and Fig.4.8.(b), respectively. Similarly to the strain kinetics given in Fig.4.5.(a), the disordering kinetics were established along the [001], [010] and [100] directions. Fig.4.8.(c) presents the disordering kinetics measured from the RBS/C experiments of 500 keV La ions on UO_2 (see the supplementary material of ref. [123]). In the experiments, the damage dose was initially represented by dpa, which was converted into dpU in this thesis by using Eq.(4.1). As in the case of strain kinetics, the disordering kinetics obtained from both XRD and RBS/C simulations exhibit distinct features with the dpU level, but also different responses to the different defects. In the low dpU region where point defects dominate, the disorder fraction shows a steady increase. After around 0.1 dpU, when dislocations start to form, the disordering rate increases. The disorder fraction reaches a maximum at around 0.4 dpU, which is slightly larger than

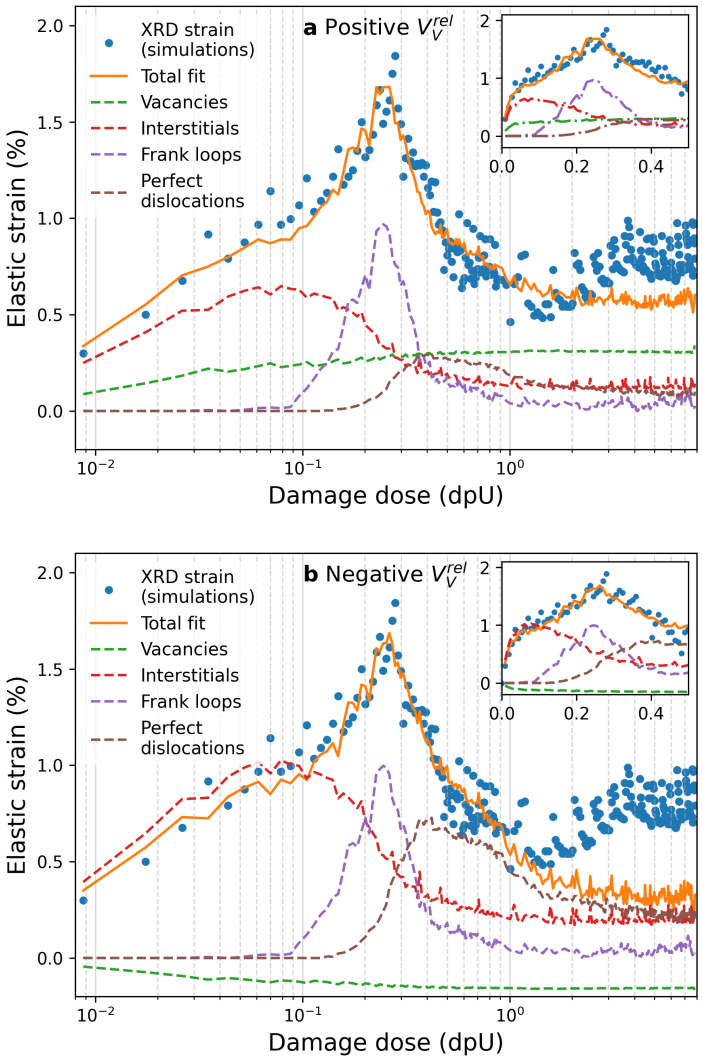

Figure 4.7 – Decompositions of the simulated elastic strain kinetics using (a) a positive V_V^{rel} (RMSD $= 1.7 \times 10^{-1}$) and (b) a negative V_V^{rel} (RMSD $= 3.4 \times 10^{-1}$). The blue dots represent the elastic strain computed from the XRD simulations and averaged over the three <001> directions. The solid line represents the total fit by combining contributions of the different defects (dashed lines). Insets use a linear scale for the x axis. (In order to avoid a dense overlap, only one value in every five simulation results is shown when the damage dose is larger than 1.0 dpU.)

the dpU of maximum strain ($\sim$ 0.28 dpU). We will show hereafter that this difference, albeit small, is meaningful. Instead of saturating at a maximum value, the disorder in the high dpU region is lower than the maximum value measured at intermediate dpU region, and in both regions, the disorder remains well below 100 %, which confirms that UO_2 cannot be amorphized by ion irradiation. In addition, in the high dpU region, the disorder fractions measured for the three directions diverge and experience considerable fluctuations, the reason of which can be attributed to the formation of sub-crystalline structures, which are slightly misoriented with respect to each other. In larger simulation

cells, it is reasonable to assume that this anisotropy effect would vanish as a result of an ensemble averaging.

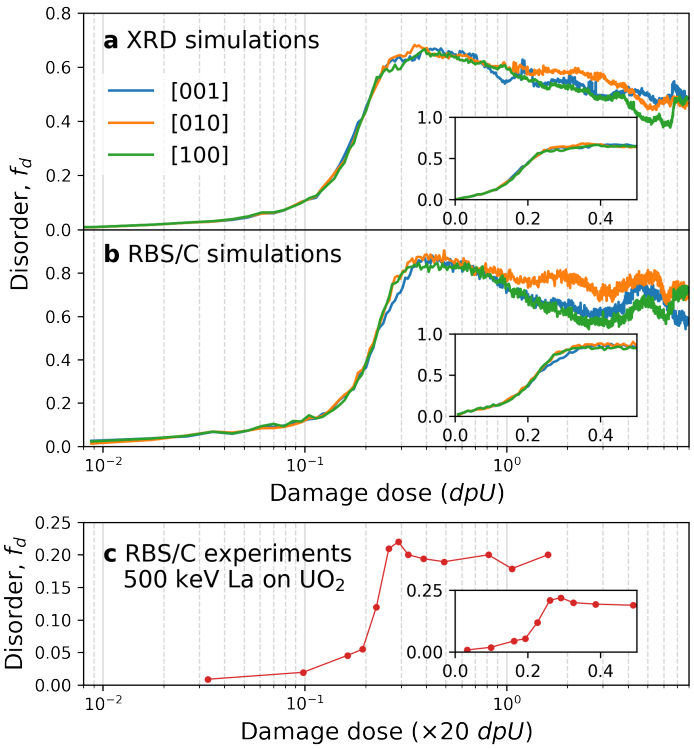

Figure 4.8 – Disordering kinetics as a function of dpU obtained from (a) the XRD simulations, (b) the RBS/C simulations on the UO_2 MD cells and (c) RBS/C experiments of 500 keV La ions on UO_2 crystals. In the simulations, disorder fractions were calculated along the [001] (blue), [010] (orange) and [100] (green) directions of MD cells. In the experiments, the channeling direction is along the <001> direction. (Insets use a linear scale for the x axis.) (Figure source: Jin et al., Acta Mater., 2020 [249], T. Nguyen, Ph.D. thesis, 2013 [184])

The absolute disorder values calculated from the XRD and RBS/C simulations differ, which is not unexpected. For instance, the disorder in XRD simulations is derived from the DW factor, which depends on the scattering vector **Q** (or Bragg reflection planes). The DW factor is therefore not an absolute measure of disorder. Besides, the disorder in RBS/C simulations is determined by the relative increase of the backscattering yield that depends on He energy. (Also, the effect of dechanneling was not taken into account, but a study provided in Appendix.A indicates that this effect is negligible.) Despite this discrepancy in the disorder values between the two techniques, noticeably, the overall shapes of disordering kinetics from the two simulations are in remarkably good agreement. This indicates that the two techniques can be used interchangeably to extract information related to disorder.

There are also discrepancies regarding the levels of disorder and dpU between the results obtained from simulations and experiments, which can be explained according to the same reasons given in the case of elastic strain. Since the atomic mass of La is very close to that of Ce, the dpU production rate of 500 keV La ions on UO_2 was similar to that induced by 500 keV Ce ions (3.4×10^{-3} dpU/s), which is smaller than that in the MD cells (1.5625×10^{9} dpU/s) by orders of magnitudes. The sheer difference on the dpU production rate generates more dislocations in the MD cells compared to those in the real samples, which explains why the disorder values in RBS/C simulations are around 4 times higher than those in the experiments. The onset of defect transformation in RBS/C experiments requires around 20 times higher dpU compared to that in the simulations. The reasons for the apparent higher damage level required in the experiments are same to those applied in the case of elastic strain kinetics: the overestimation of stable defects in the SRIM calculations compared to those in the current MD simulations and the higher defect density in the MD cells.

Overall, the disordering kinetics obtained from the simulations and experiments exhibit a good qualitative agreement. Similar disordering kinetics have been observed in materials in which the cationic sub-lattice or the entire crystal has a FCC structure, including cubic yttria-stabilized zirconia (YSZ) [139, 171], MgO [259], Ni [260] and Ni-based alloys [261]. Since the U sub-lattice in UO_2 also has a FCC structure, these materials can have similar types of defects, which might be a possible reason for the observed similarity between the disordering kinetics and the evolution of defects.

Quantitative study

In order to improve our qualitative observations regarding the connection between the disordering kinetics and the defect nature and quantity, we propose to decompose the disordering kinetics in a similar way to that applied for the strain kinetics. We modeled the disordering kinetics by assuming a linear relationship between the disorder and the quantity of defects (i.e., concentrations for point defects and densities for dislocations). Since it is commonly acknowledged that the contribution of vacancies to disorder is negligible [123, 180], we did not include these defects in the modelling.

Firstly, we fitted the disordering kinetics calculated from the RBS/C simulations, and averaged over the three <001> directions. The result is presented in Fig.4.9, in which the total fit (solid line) is obtained by combining contributions from the different defects (dashed lines). It can be observed that the fitting quality is satisfactory below 0.4 dpU. However, above 0.4 dpU, the fit fails. Above 0.4 dpU, the dominant defects are perfect dislocations. What was overlooked until now is that the perfect dislocations

can be composed of perfect loops and perfect lines. Thus, the most probable reason for the failure of the fit at higher dpU is that both types of dislocations have a different contributions to the disorder.

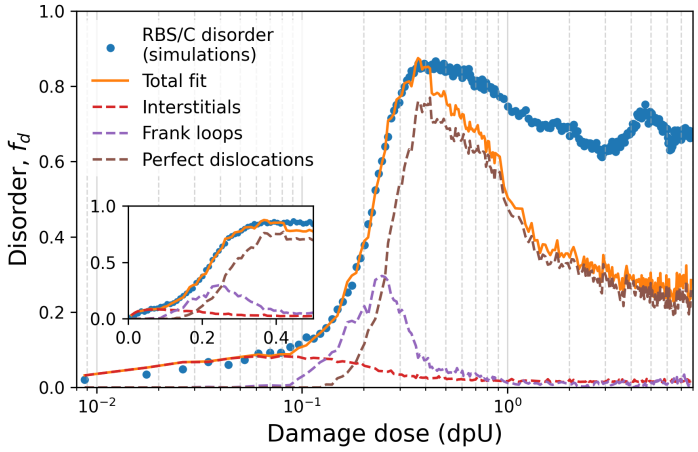

Figure 4.9 – Decomposition of the simulated disordering kinetics calculated from the RBS/C simulations. The blue dots represent the disorder fraction computed from the simulations and averaged over the three <001> directions. The solid line represents the total fit by combining contributions of the different defects (dashed lines). The inset uses a linear scale for the x axis. (In order to avoid a dense overlap, only one value in every five simulation results is shown when the damage dose is larger than 1.0 dpU.) (Figure source: Jin et al., Acta Mater., 2020 [249])

According to Fig.4.2, we can notice that both Frank loops and perfect dislocations have large incubation periods. Since the perfect dislocations start to form at around 0.12 dpU and the initial state of perfect dislocations should be loops, we can assume that the onset of the perfect lines requires a dpU level higher than 0.12. Then, a reasonable starting point for the formation of perfect lines could be set to 0.4 dpU, from which point the fit quality deteriorates. As more and more loops coalesce into lines with higher dpU, the density of perfect lines should grow and approach a saturation value as indicated in Fig.4.2. From the starting point to the final saturation stage, we used an *ad hoc* model to determine the shape of the density of perfect lines, ρ_p^{line}, which is assumed to have a sigmoidal shape (support for this assumption is provided in Appendix.B). The *ad hoc* model is a combination of the assumption of the linear relation between disorder and defect quantity and a modified (by us) version of the cascade-overlap model [262] (details of this *ad hoc* model are given in Appendix.B). Then, the density of perfect loops, ρ_p^{loop}, is calculated by $\rho_p^{loop} = \rho_p - \rho_p^{line}$. Finally, the total disorder, f_d, reads:

$$f_d = r_I C_I + r_F \rho_F + r_p^{loop} \rho_p^{loop} + r_p^{line} \rho_p^{line} \tag{4.4}$$

where r_I is the disorder constant for the interstitials, and r_F, r_p^{loop} and r_p^{line} are the disorder constants for the Frank loops, perfect loops and perfect lines, respectively, with a m^2 unit.

After separating the contributions of perfect loops and lines, new fits on the disordering kinetics obtained from the RBS/C and XRD simulations are presented in Fig.4.10.(a) and Fig.4.10.(b), respectively. The fit quality on the right side of the disorder peak is visibly improved as compared to Fig.4.9. The constants in Eq.(4.4) are listed in Table II. What is interesting to mention is that although the total disorder decreases from the intermediate dpU region (mainly loops) to the high dpU region (mainly lines), Table II shows that the disorder constants of perfect lines are higher than those of perfect loops in both RBS/C and XRD simulations, which indicates that lines induce an apparent disorder larger than loops. Thus, the decrease of disorder is mainly due to the decrease of the total dislocation density. This property could be used to identity defects from experimental data.

Table II – Disorder constants, r, for defects used in the fits. **a** RBS/C disordering kinetics, **b** XRD disordering kinetics. The errors are obtained from the non-linear least squares fitting algorithm.

	r_I	$r_F(\times 10^{-17} m^2)$	$r_p^{loop}(\times 10^{-17} m^2)$	$r_p^{line}(\times 10^{-17} m^2)$
RBS/C	4.31 ± 0.96	0.75 ± 0.07	0.92 ± 0.02	2.10 ± 0.08
XRD	2.60 ± 0.47	0.97 ± 0.03	0.67 ± 0.08	1.71 ± 0.05

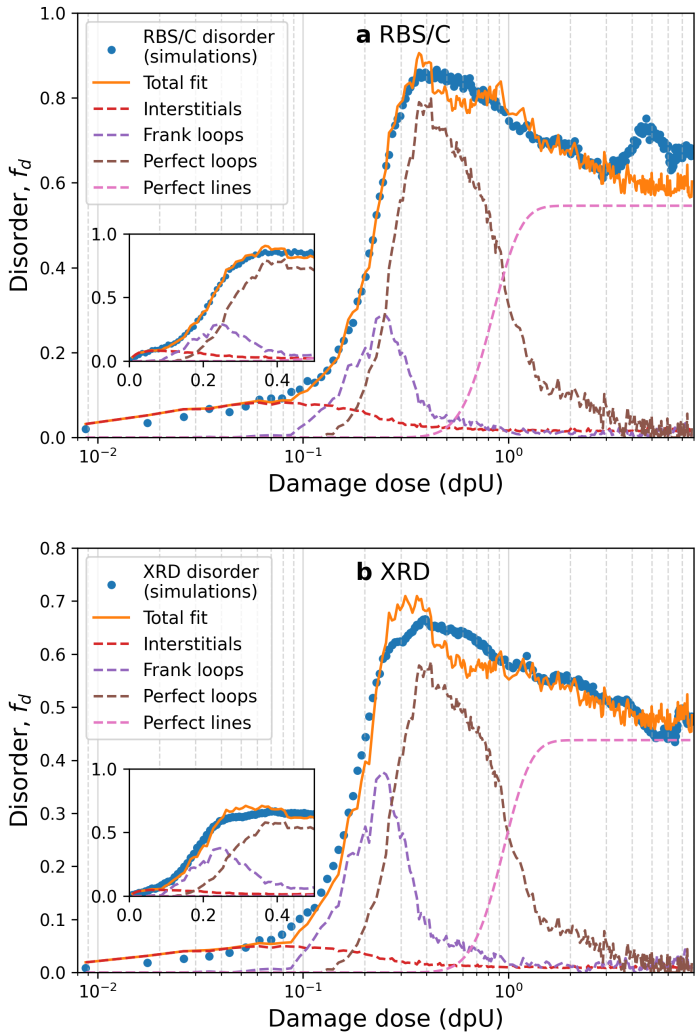

Figure 4.10 – Decomposition of the simulated disordering kinetics by separating the contributions of perfect loops and lines obtained from (a) the RBS/C simulations and (b) the XRD simulations. The blue dots represent the disorder fraction computed from the simulations and averaged over the three <001> directions. The solid line represents the total fit by combining contributions of the different defects (dashed lines). Insets use a linear scale for the x axis. (In order to avoid a dense overlap, only one value in every five simulation results is shown when the damage dose is larger than 1.0 dpU.) (Figure source: Jin et al., Acta Mater., 2020 [249])

4.3 Systematic study of model defective systems - Fe as a test-case

4.3.1 Description of model defective systems

In the previous sections, we studied the response of XRD and RBS/C techniques to the defects generated by the FPA method applied to UO_2 MD cells. In these UO_2 cells,

several types of defects can coexist and entangle with each other, which brings difficulties in terms of separating their individual contributions to the strain and disordering kinetics. In the current section, we will study model defective systems in the form of Fe MD cells containing, each, only one type of defects. By this way, a clear and unambiguous information can be obtained about the effect of defects, including vacancies, interstitials, dislocation loops, etc., on the XRD and RBS/C signals, without the need to decompose their respective contributions. This work is the prequel of a broader investigation (which is part of another PhD research work) dedicated to studying more complex Fe MD cells generated by the FPA method along with Fe samples irradiated under *ad hoc* conditions.

The type of Fe studied here is alpha-iron which has a BCC structure. A pristine Fe MD cell contains 10 000 422 atoms and has a cubic shape with a side length of 48.467 nm. The x, y and z directions of the cell are along the [100], [010] and [001] directions, respectively. An empirical potential of the embedded-atom method (EAM) type is used to describe the atomic interactions [263]. For defective cells, only one type of defect is introduced into each cell. The general categories of the defects are point defects, voids and dislocation loops. Point defects were randomly distributed inside the cells, and interstitials were introduced as <110> dumbbells. Voids were created with a spherical shape. Dislocation loops were produced by introducing circular platelets of interstitial or vacancy clusters into the cells. After the introduction of defects, the cells were relaxed at constant volume, which was decided either by a further relaxation at constant pressure or by successive energy calculations at various cell sizes to reach "by hand" the zero pressure.

In these defective cells, three of them contain point defects, which are listed as follows:

- One cell contains 1 % of vacancies. It will be denoted by $V1$ in the following;
- One cell contains 1 % of interstitials. It will be denoted by $I1$;
- The third one contains 1 % of RDA. It will be denoted by $R1$;

There are two cells containing voids, which are listed as follows:

- The first cell contains 100 voids, each of which is composed of 1000 vacancies. If the voids were dissolved into isolated vacancies, it would be equivalent to an injection of 1 % of vacancies. This cell will be denoted by $Vo100$;
- The second one contains 1000 voids, each of which is composed of 100 vacancies. Similar to the previous cell, it is equivalent to an injection of 1 % of vacancies. This cell will be denoted by $Vo1000$;

Other cells were filled with dislocation loops. A detailed description of these cells is given hereafter:

- The first cell contains 1000 dislocation loops, and each one is composed of 83 interstitials. The loops belong to perfect loops with the Burgers vector as 1/2<111>. If the loops were dissolved into isolated interstitials, it would be equivalent to an injection of 0.830 % of interstitials. This cell will be denoted by $L830$;
- The second one contains 100 1/2<111> loops, each of which is composed of 896 interstitials. These loops represent 0.896 % of interstitials. This cell will be denoted by $L896$;
- The third one contains 100 1/2<111> loops, each of which is composed of 1000 interstitials. These loops represent 1.000 % of interstitials. This cell will be denoted by $L1000$;
- The forth one contains 100 1/2<111> loops, each of which is composed of 1000 vacancies. If the loops were dissolved into isolated vacancies, it would be equivalent to an injection of 1.000 % of vacancies. This cell will be denoted by $L1000V$.

In all the cells containing dislocation loops, the lying planes of the loops are randomly chosen among the {111} planes. Visualization of $L830$ and $L896$ along the [001] direction is presented in Fig.4.11.(a) and (c), respectively, using the OVITO code. Fig.4.11.(b) and (d) show parts of $L830$ and $L896$, respectively. In Fig.4.11, the loop type is mainly of 1/2<111> type (green) according to the analysis using the DXA method. There is also a small amount of <100> loops (red), which were most likely produced by the interaction of 1/2<111> loops. It can be observed, especially in Fig.4.11(b) and (d), that Fe atoms (represented by blue dots) were mainly displaced towards two directions in the regions affected by the loops. The two displacement directions are represented by the orange and blue arrows in the figure.

In order to study the effect of the loop orientation, an additional perfect Fe MD cell was created, in which the z direction is along the [111] direction. Three defective cells were prepared, all of which were injected with 100 1/2<111> loops containing 896 interstitials, but the configuration of the Burgers vectors (i.e., the lying plane of the loops) is different. They are listed as follows:

- In the first cell, the directions of Burgers vectors were randomly distributed among the <111> directions. The cell will be denoted by $L896b1$;
- In the second cell, all Burgers vectors were along the [111] direction parallel to the z axis. The cell will be denoted by $L896b2$;

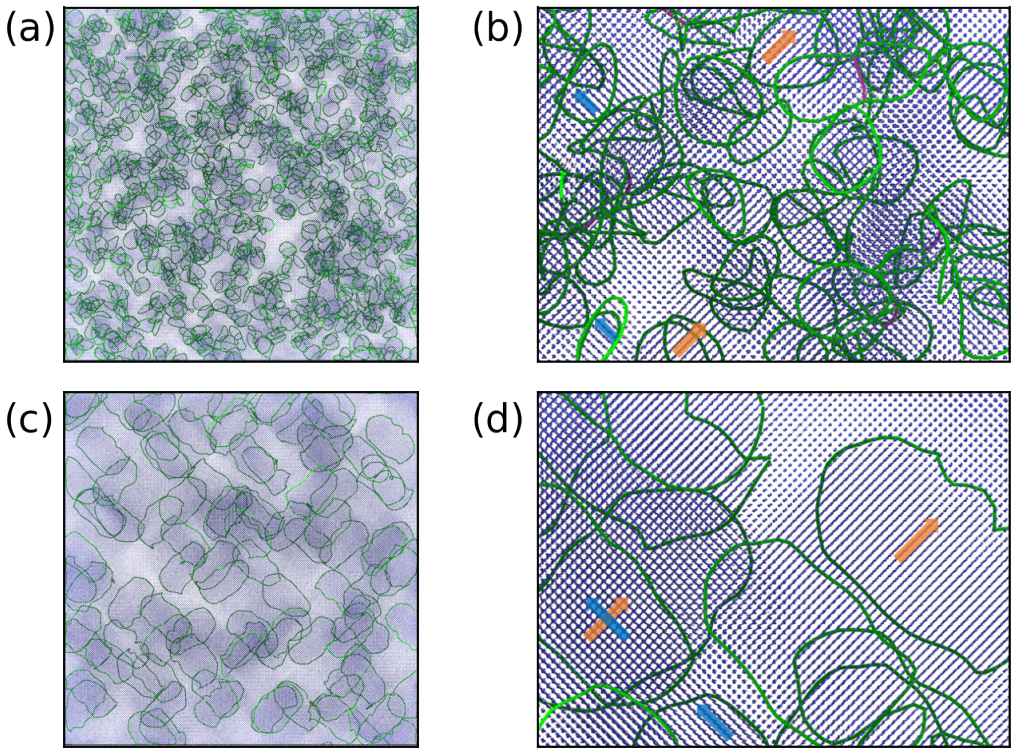

Figure 4.11 – Visualization of the Fe MD cells containing dislocation loops along the [001] direction. (a) and (c) show $L830$ and $L896$, respectively, in which 1/2<111> loops are represented by green lines and a small amount of <100> loops are represented by red lines. (b) and (d) shows parts of $L830$ and $L896$, respectively, in which Fe atoms are represented by blue dots. The orange and blue arrows indicate two moving directions of atoms affected be the loops.

- In the third cell, the directions of Burgers vectors were distributed among the <111> directions except that along the z axis. This cell will be denoted by $L896b3$;

4.3.2 Systematic study of model defective systems: Fe

XRD: elastic strain and disorder

XRD simulations were used to study both elastic strain and disorder in the Fe MD cells, using the method mentioned in Sec.2.2.3. 3D intensity distributions were calculated in the vicinity of the 002 Bragg reflection along the [001] direction. Subsequently, 2D RSMs were obtained by integrating the 3D intensity distributions along the y direction.

Fig.4.12.(a-d) show the 2D RSMs calculated in the vicinity of the 002 Bragg reflection using the Fe MD cells which are the pristine, $V1$, $I1$ and $R1$ cells, respectively. Peaks are represented by black dots, in which the maximum peak is denoted O_1. If there are other peaks, the subscript in O_i (i is integer) increases and the associated peak has

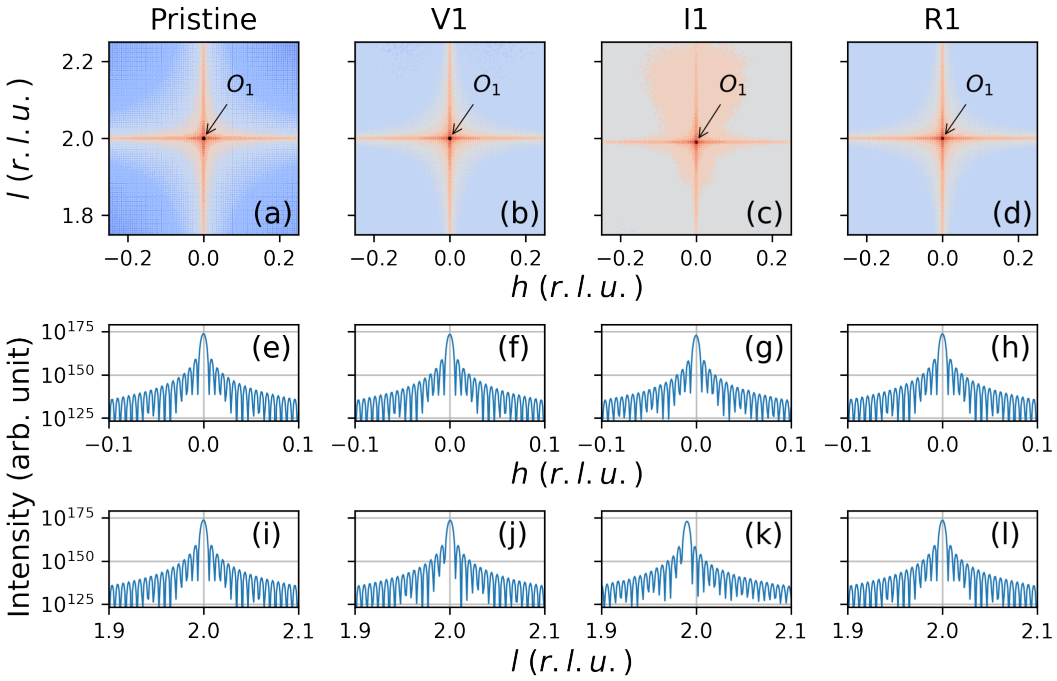

Figure 4.12 – Intensity distributions calculated from Fe MD cells (point defects). (a-d) 2D RSMs calculated in the vicinity of the 002 Bragg reflections using the pristine, $V1$, $I1$ and $R1$ cells, respectively. Peaks are indicated by black dots, in which the maximum one is denoted by O_1. Units of h and l are reciprocal lattice units (r.l.u). The intensities (on a logarithmic scale) are represented in a warm to cold color scale; (e-h) Corresponding 1D line scan determined along the h-line where the highest peak is located; (i-l) Corresponding 1D line scan determined along the l-line where the highest peak is located.

a lower intensity. Units of h and l are reciprocal lattice units (r.l.u). Fig.4.12.(e-h) represent the corresponding intensities measured along the h-line where O_1 is located, which provides the information related to the tilt angle. Fig.4.12.(i-l) represent the corresponding intensities measured along the l-line where O_1 is located, which provides the information related to the elastic strain. The settings in Fig.4.13 and Fig.4.14 are the same as those of Fig.4.12. The 2D RSMs in Fig.4.13 were calculated from the $Vo100$, $Vo1000$, $L830$ and $L896$ cells, respectively. The 2D RSMs in Fig.4.14 were calculated from the $L1000$ and $L1000V$ cells, respectively. It can be observed that there are multiple peaks in Fig.4.14.(a), which is probably due to a mosaic structure induced by the dislocation loops, as discussed in UO_2.

In the RSMs of defective cells, there are higher intensities in background regions, which correspond to diffuse scattering due to the presence of defects. Some information can be readily extracted from the shape of this signal. In Fig.4.12.(c), the diffuse scattering has an asymmetric shape with more intensity on the higher side of the Bragg reflection (i.e.,

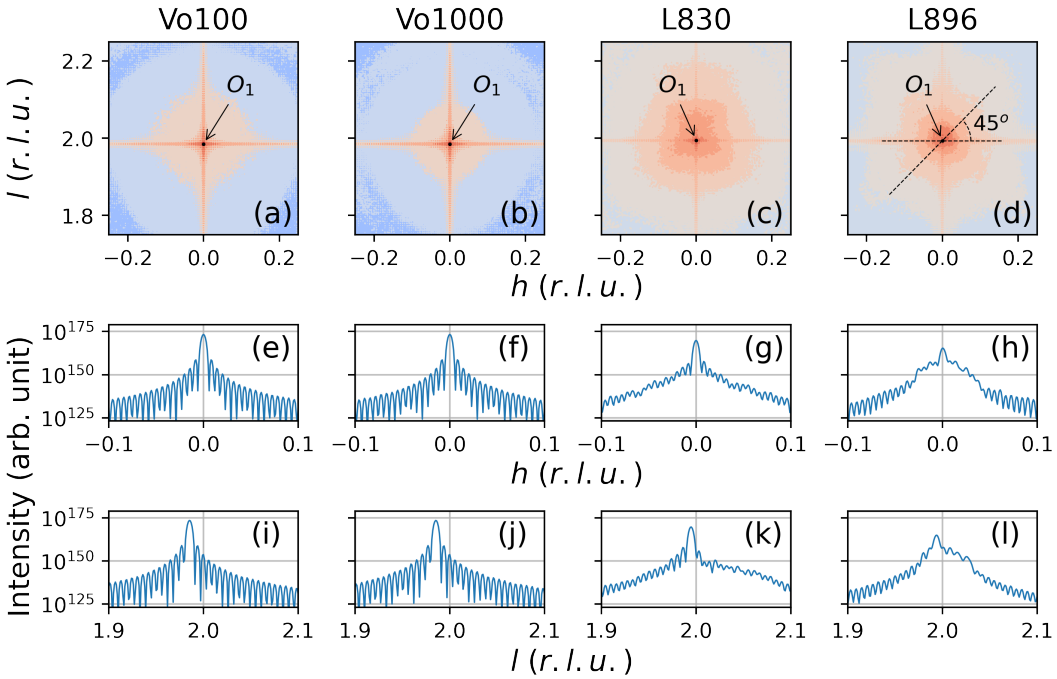

Figure 4.13 – Intensity distributions calculated from Fe MD cells (voids and some dislocation loops). (a-d) 2D RSMs calculated in the vicinity of the 002 Bragg reflections using the $Vo100$, $Vo1000$, $L830$ and $L896$ cells, respectively; (e-h) Corresponding 1D line scan determined along the h-line where the highest peak is located; (i-l) Corresponding 1D line scan determined along the l-line where the highest peak is located. Other setting are same to those in Fig.4.12

$l > 2.0$). This indicates the presence of local compressed regions, which is expected since the defects are interstitials (Note that interstitials induce homogeneous tensile strain) [254]. In Fig.4.13.(d), the iso-intensity curves of the diffuse scattering contain streaks, which are related to the loop plane itself. The angle between the streak and the horizontal axis is 45^o. This result is also expected, since the projection of Burgers vector of 1/2<111> dislocation loops onto the (010) plane (that is the xz plane) is along the <101> direction, which has an angle of 45^o with respect to the <100> direction. If the size of the dislocation loop is larger, clearer patterns of streaks should be observed [264, 265].

Elastic strain and DW factor levels were calculated using Eq.(2.43) and Eq.(2.44), respectively. The relative disorders were calculated as $(1 - DW)$. The accuracy of peak location in the 2D RSMs is determined by the width of the bins (peaks located in one bin are represented by one coordinate in the RSM), which is equal to 0.001 r.l.u. in the current simulations. Thus, for 002 Bragg reflections, the uncertainty for elastic strain,

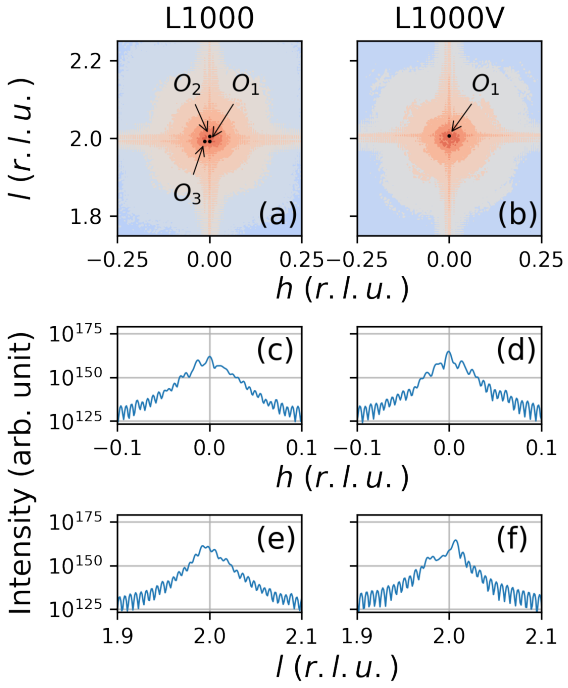

Figure 4.14 – Intensity distributions calculated from Fe MD cells (some dislocation loops). (a-b) 2D RSMs calculated in the vicinity of the 002 Bragg reflections using the $L1000$ and $L1000V$ cells, respectively; (c-d) Corresponding 1D line scan determined along the h-line where the highest peak is located; (e-f) Corresponding 1D line scan determined along the l-line where the highest peak is located. Other setting are same to those in Fig.4.12

Δe^{def}, is calculated as follows:

$$\Delta e^{def} = \frac{0.1}{l_d^2 - 2.5 \times 10^{-7}} \tag{4.5}$$

Values of the disorder should have very small uncertainties, because the calculation is based on the measurement of the intensity, the accuracy of which is determined by the precision of floating-point data used in the GPU or CPU calculations (for example, single-precision floating-point operations have a relative accuracy of around 10^{-7}) [266]. Due to these reasons, the uncertainty of disorder will not be given here. It is worth mentioning that the MD simulations themselves can also be an additional source of uncertainties. If multiple MD simulations were performed for each defective cell by using different settings related to the stochastic nature of the MD simulations (e.g., the settings for randomly choosing the location of defects), a mean value of the MD simulations could be obtained by taking the average of the multiple MD simulations. However, since the duration of the MD simulations is long due to large amounts of atoms in the cells, all XRD simulations (and RBS/C simulations which will be presented in the next subsection) were only performed

on one set of cells.

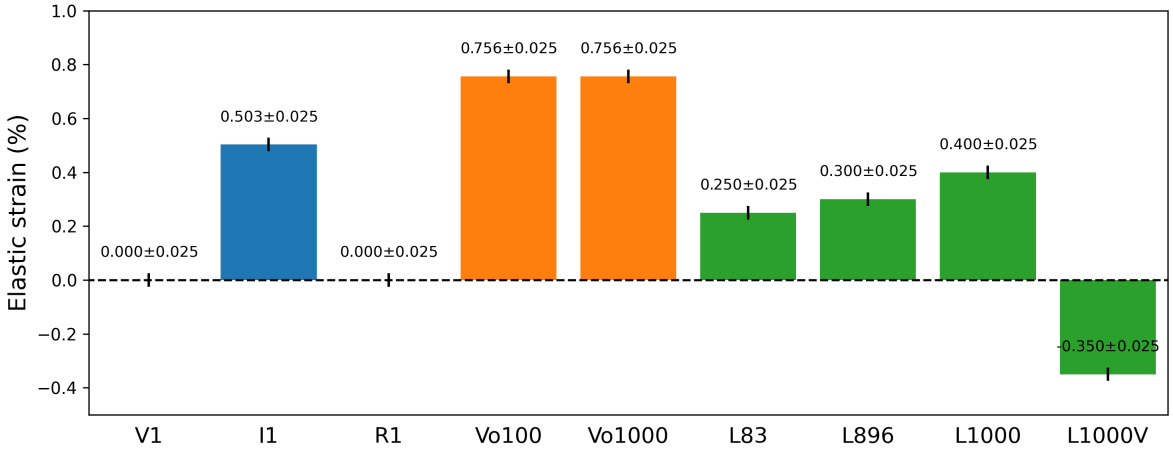

Figure 4.15 – Elastic strain calculated from the XRD signals obtained with the Fe MD cells containing point defects (blue), voids (orange) and dislocation loops (green). The black sticks represent the errors.

Elastic strain and point defects Fig.4.15 shows the elastic strain calculated from the Fe MD cells containing point defects (blue), voids (orange) and dislocation loops (green). The strain corresponding to the MD cells containing single vacancies is almost zero, which could be expected from such type of defects in metals [267]. There is basically no strain induced by the RDAs ($R1$) either, which can be explained by the fact that these defects do not correspond to regular point defects because their location in the lattice is completely random; hence, 1% of RDAs cannot induce strain. The elastic strain induced by interstitials ($I1$) is 0.50 %, which gives a relaxation volume of 1.5 Ω, according to Eq.(4.3). This relaxation volume is similar to that derived from a DFT calculation [267], which provides some confidence on the value we determined.

Elastic strain and extended defects In $Vo100V$ and $Vo1000V$, where voids are present, the lattice volume change is equal to 0.76 % for both sizes of defects. On the one hand, it is surprising to observe that voids induce such large lattice expansion (intuitively, we would have expected a contraction), and this result must be confirmed using other interatomic potentials; on the other hand, this result indicates that since the elastic energy of voids is higher than that of vacancies, it is not favorable to create voids from vacancies in Fe. In $L1000V$, where dislocation loops are formed by vacancies, the elastic strain is -0.35 %, the absolute value of which is significantly larger than that (i.e. 0 %) induced by an equivalent quantity of isolated vacancies ($V1$), which, similarly to voids, might exclude the formation of such defects from vacancies in Fe.

Regarding interstitial-type dislocation loops, we found that the elastic strain induced in $L1000$ (0.40 %) is smaller than that induced in $I1$ (i.e., 0.50 %), even though the total number of single defects is the same. Therefore, defects clustered into loops do not expand the lattice as much as single defects; this finding has a resonance with the strain kinetics given in Fig.4.7.(a), where the increase in strain in UO_2 becomes slower when interstitials transform into dislocation loops. In fact, it is known that the relaxation volume of interstitial defects gradually decreases from single, isolated interstitials to large dislocation loops [124]. The associated decrease in elastic energy is one of the reasons why defect clustering takes place.

In $L896$, which contains the same dislocation loops as $L1000$ but a slightly lower number of defects, the strain is 0.3 %, i.e. less than that in $L1000$. The difference cannot be due solely to the small difference in the total number of defects, so there might be another explanation that we will look for. Similarly, the strain decreases from $L1000$ to $L830$. It is reported that the relaxation volume of a defect in a dislocation loop should evolve with the perimeter of the loop, so it should be proportional to the square-root of the number of defects inside the loop. We do not have enough data to verify this statement. Additional work is currently in progress to complete this systematic study. Anyway, overall, our results are in reasonable agreement with what is known in the literature.

Disorder for point and extended defects Fig.4.16 shows the disorder calculated from the Fe MD cells containing point defects (blue), voids (orange, but the level is so low that this color is not visible) and dislocation loops (green) obtained by using XRD simulations. For cells containing single-vacancies ($V1$) and voids ($Vo100$ and $Vo1000$), basically no disorder is detected. No significant displacement of atoms surrounding these defects is expected (at least in metals), and the defect density is only 1 % (only 1% of atoms are simply missing). Therefore, the non-measurable disorder was expected. The disorder induced in $R1$ is also negligible. Single-interstitial defects ($I1$) produce a disorder barely detected (0.01) with the XRD technique (we recall that the absolute disorder level from XRD depends on the probed hkl reflection). In stark contrast, the disorder induced by extended defects such as dislocation loops (whether they are of vacancy- or interstitial-type) is significantly higher. For the largest loops investigated here, the disorder level is on the order of 0.5, and for smaller loops ($L830$ for instance), the disorder is still 0.2 (vs 0.01 for single-interstitials, even though the total number of defects is roughly the same). Thus, the transformation of point defects into dislocation loops leads to a higher degree of the disorder level as determined by XRD. This finding is in line with the results obtained for the study of UO_2 (see previous section and notably, Fig.4.10), and it makes

perfect sense. Indeed, it is no surprise that the disorder determined by XRD is much more related to extended defects than to point defects because the latter only induce short range disorder, contrarily to dislocations.

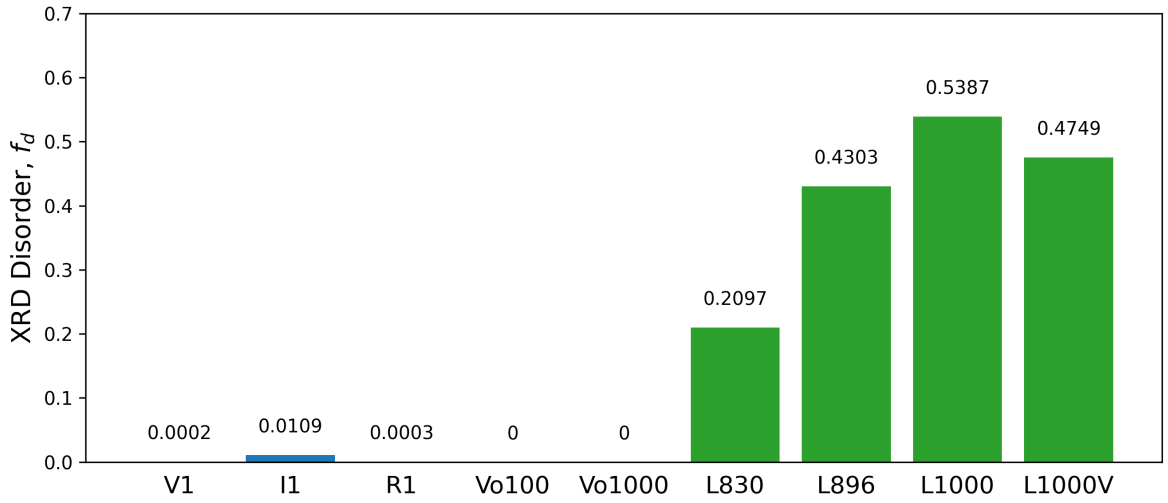

Figure 4.16 – Disorder obtained from XRD simulations performed on the Fe MD cells containing point defects (blue), voids (orange) and dislocation loops (green).

RBS/C: disorder

RBS/C simulations were performed to study the disorder in the Fe MD cells according to the method mentioned in Sec.2.1.2 by using the RBSADEC code. Periodic boundary conditions were applied to the x and y directions of the cells. A beam of 1.4 MeV He ions enters into the cells along the z direction. For each cell, both the spectra in the random and aligned configurations were calculated in order to compute normalization factors as in the case of simulating RBS/C spectra from the UO_2 MD cells. The TRIM-based amorphous slowdown approach was used to calculate the trajectories of backscattered virtual ions. The 1D rms value of the atomic thermal vibration magnitude at room temperature was calculated according to the temperature factor obtained from XRD experiments [268], which gives a value of 6.6 pm. The incident ion beam divergence was described by the type of IBD-B with the standard deviation angle as 0.12° (See Sec.3.2). For the simulation of aligned spectra, the original approach in the RBSADEC code was applied, in which the maximum impact parameter used in the search of collision partners was automatically set to a fixed value, i.e., r_v. The disorder was calculated using Eq.(2.10). Since the Monte-Carlo simulations in the RBSADEC code have a stochastic nature, we repeated the simulations 21 times with different random number seeds for each cell in order to determine the mean value of disorder and associated uncertainty.

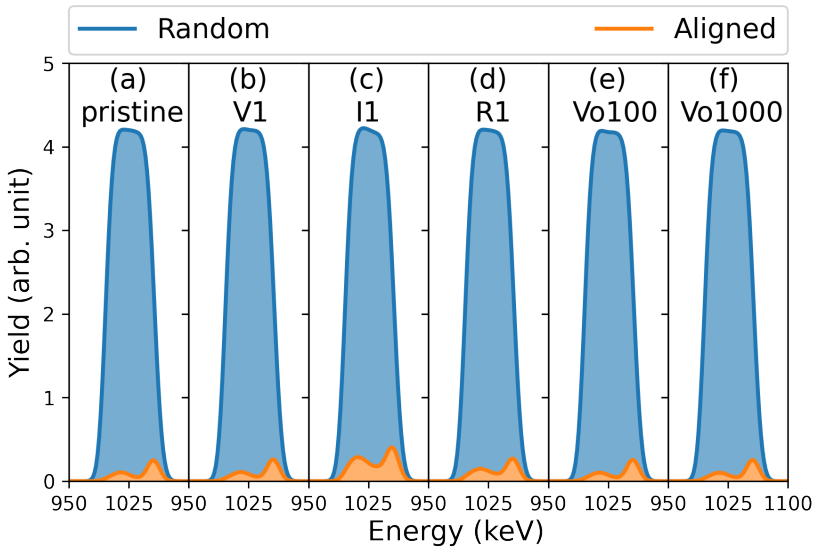

Figure 4.17 – RBS/C spectra generated from 1.4 MeV He ions on <001>-oriented Fe MD cells (point defects and voids). (a-f) represent the spectra generated from the pristine, $V1$, $I1$, $R1$, $Vo100$ and $Vo1000$ cells, respectively. Blue and orange lines represent the spectra obtained from the random and aligned configurations, respectively.

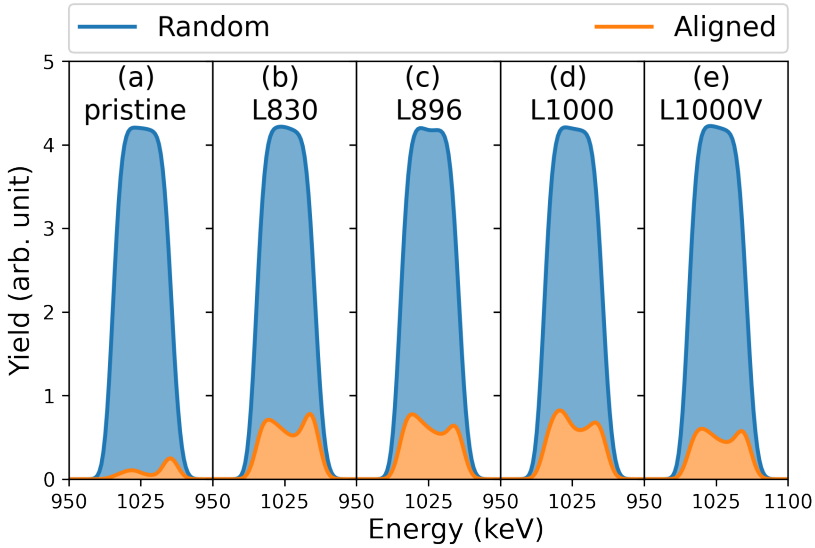

Figure 4.18 – RBS/C spectra generated from 1.4 MeV He ions on <001>-oriented Fe MD cells (dislocation loops). (a-e) represent the spectra generated from the pristine, $L830$, $L896$, $L1000$ and $L1000V$ cells, respectively. Blue and orange lines represent the spectra obtained from the random and aligned configurations, respectively.

Fig.4.17.(a-f) show the RBS/C spectra generated from 1.4 MeV He ions on <001>-oriented Fe MD cells, which includes the spectra calculated from the pristine cell and the cells containing point defects ($V1$, $I1$ and $R1$) and voids ($Vo100$ and $Vo1000$). The aligned spectrum (orange) generated from the pristine cell exhibits two peaks. The peak

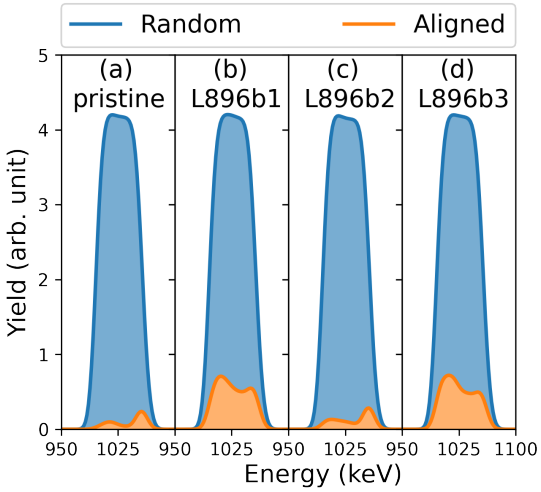

Figure 4.19 – RBS/C spectra generated from 1.4 MeV He ions on <111>-oriented Fe MD cells (dislocation loops). (a-d) represent the spectra generated from the pristine, *L*896*b*1, *L*896*b*2 and *L*896*b*3 cells, respectively. Blue and orange lines represent the spectra obtained from the random and aligned configurations, respectively.

on the high energy side is the surface peak, and the other peak is due to the interactions of He ions with atoms beneath the surface region. The settings in Fig.4.18 are the same as those in Fig.4.17, except that the damaged cells contain dislocation loops (*L*830, *L*896, *L*1000 and *L*1000*V*). Fig.4.19.(a-d) show the RBS/C spectra generated from 1.4 MeV He ions on <111>-oriented Fe MD cells, in which the damaged cells contain dislocation loops with different orientations (*L*896*b*1, *L*896*b*2 and *L*896*b*3).

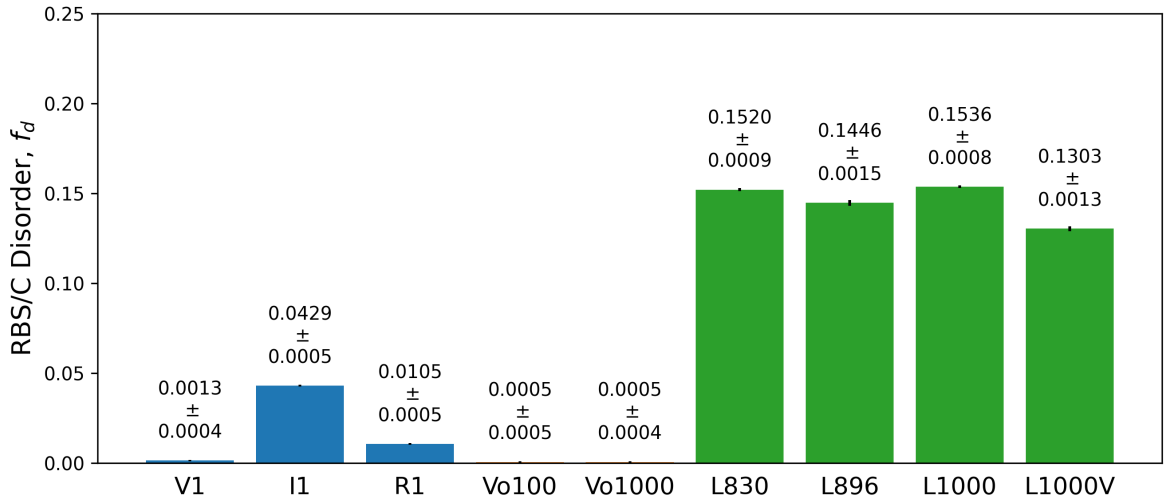

Figure 4.20 – Disorders obtained from RBS/C simulations performed on the <001>-oriented Fe MD cells containing point defects (blue), voids (orange) and dislocation loops (green). The black sticks represent the errors.

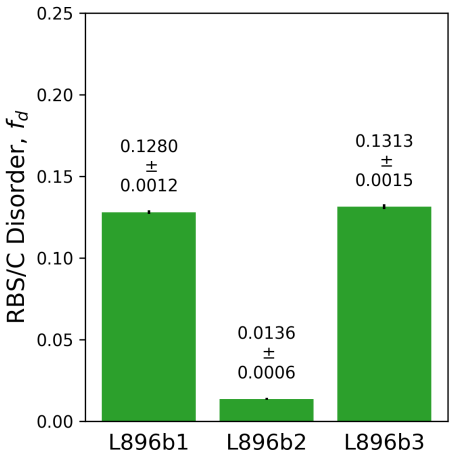

Figure 4.21 – Disorder obtained from RBS/C simulations performed on the <111>-oriented Fe MD cells containing dislocation loops. The black sticks represent the errors.

Fig.4.20 shows the disorder obtained from the RBS/C simulations performed on the different <001>-oriented Fe MD cells, as previously described. The uncertainties are represented by the black sticks, some of which are so small that they are barely visible. Vacancies ($V1$) and voids ($Vo100$ and $Vo1000$) generate trace amount of disorder, which is similar to the results obtained from the XRD simulations. The disorder induced by $R1$ is 0.01, which is the concentration of these randomly displaced atoms, but the disorder induced by $I1$ is more than 4 times greater. Thus, it is important to note that RDAs cannot be directly used to estimate the number of interstitials, though they provide a convenient way to estimate the disorder.

In terms of disorder induced by dislocation loops, it is always far larger than that produced by point defects, no matter if the dislocation is of interstitial or vacancy type. Considering only these results, it is impossible to draw a conclusion about how the size of the loops affects the disorder. A study in the next section may provide a hint about that very point. Another factor affecting the disorder level is the habit planes of the loops, which is exhibited by the disorder measured from the <111>-oriented Fe MD cells, as shown in Fig.4.21. While the disorder levels in $L896b1$ and $L896b3$ are close, it is significantly lower in $L896b2$. This very low value is due to the fact that atoms in $L896b2$ are mainly displaced along the direction parallel to that of the probing He ions and thus this displacement is difficult to be detected. The disorder levels in $L896b1$ and $L896b3$ (i.e., ~ 0.13 %) are slightly lower than that in $L896$ (i.e., ~ 0.14 %). A plausible reason could be that atoms in these cells are displaced in a smaller extent in directions perpendicular to <111> direction compared to <001> direction.

RBS/C: the effect of incident ion energy

Since the RBS/C yield is affected by the incident ion energy, it is of interest to study how this yield (and thus, the disorder) calculated from targets containing different types of defects vary as a function of this parameter. Hence, we calculated the disorder in the Fe MD cells using the method presented in the previous section, and we did that for He energies ranging from 1 MeV to 5 MeV. We then plotted and fitted the disorder as a linear function of $\sqrt{E}$, as shown in Fig.4.22. The reason for choosing a linear function of $\sqrt{E}$ is because the critical angle for channeling has this dependence, and thus, in the literature, researchers usually use this approach [186, 260].

The results obtained from the cells containing point defects ($V1$, $I1$ and $R1$) and voids ($Vo100$ and $Vo1000$) are given in Fig.4.22.(a), in which the linear dashed lines represent the linear fits. The numbers following the defect names in the figure legend are the slopes of the fits. Regardless of the He ion energy, the disorder induced by $V1$, $Vo100$, $Vo1000$ and even $R1$ is negligible. In contrast, for the cells containing single interstitials ($I1$), a slight but non-negligible positive slope is observed. This positive slope can be attributed to the fact that the lattice surrounding interstitials can be slightly distorted and thus, as indicated by Eq.(2.5), the shadowing effect is expected to diminish with a higher ion energy. Therefore, with a higher ion energy, there is greater probability that ions have stronger collisions with the slightly distorted atoms, which magnifies the apparent disorder.

The results obtained from the cells containing dislocations loops ($L830$, $L896$, $L1000$ and $L1000V$) are given in Fig.4.22.(b), in which all the fits (dashed lines) exhibit relatively large positive slopes. In the previous section, it was difficult to draw a conclusion about the relation between the disorder and the loop size. Here, by comparing the results obtained from $L830$, $L896$ and $L1000$, it can be inferred that the apparent disorder level does depend on the loop size, but it is required to vary the He energy to use this property. The positive slope (disorder vs $E^{1/2}$) was expected, and it is here confirmed, which is in itself a point worth putting forward. It can be explained as follows (see also discussion given in Sec.2.1.2). Dislocations induce significant distortions of atomic rows, which affects the He trajectories. As the critical angle decreases with $E^{1/2}$ (according to Eq.(2.8), the He trajectories are more influenced at high energy. If we assume that the disorder is related to those modifications of He trajectories, then we can expect that the disorder induced by dislocations loops increases with $E^{1/2}$.

It is worth mentioning that the disorder can be contributed by both direct scattering and dechanneling processes. Theoretical treatments of RBS/C data often tend to neglect direct scattering induced by dislocations. However, we should emphasize that the spatial

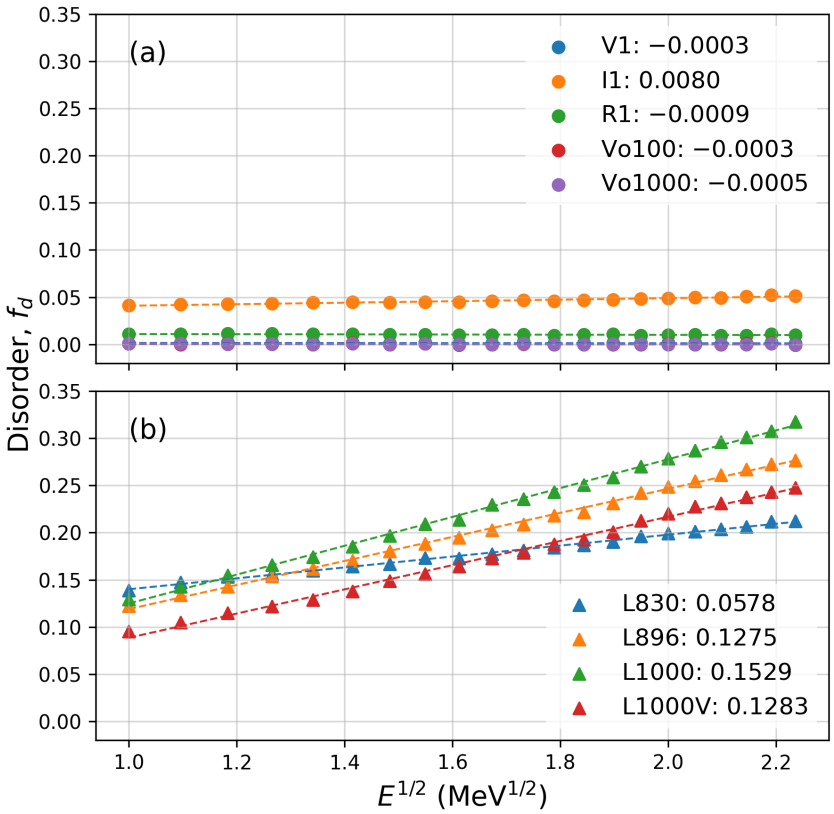

Figure 4.22 – Disorder fractions as a function of $E^{1/2}$ obtained from (a) the Fe MD cells containing point defects ($V1$, $I1$ and $R1$) and voids ($Vo100$ and $Vo1000$) and (b) the Fe MD cells containing dislocation loops ($L830$, $L896$, $L1000$ and $L1000V$). The fits of the disorders to $E^{1/2}$ are represented by the linear dashed lines, the slopes of which are the numbers following the defect names in the figure legend.

distribution of dislocations in our MD cells is isotropic and, importantly, some dislocations are located at the very 'surface' of the cells. It is therefore possible that atoms in the core of those dislocations are exposed to a He incident beam, and He ions in that beam would thus experience direct scattering events. In order to separate the contributions from direct scattering and dechanneling, we implemented two methods to determine the sole dechanneling fraction component.

In the first method (denoted as M1), one defective Fe MD cell is connected to a series of 6 pristine cells aligned along the z direction. Since there is a change of volume in defective cells as compared to the pristine one, scaling coefficients were used to adjust the atomic coordinates in the defective cells. An illustration of the connection of the cells is given in Fig.4.23. Fig.4.24 shows examples of RBS/C spectra calculated from these manually created targets, in which the He energy in Fig.4.24.(a-d) is 1000, 2400, 3800 and 5000 keV, respectively. In this figure, the blue spectra were obtained from random configurations. The orange and green spectra were obtained from aligned configurations with pristine

and $L1000$ first-cell targets, respectively. Dechanneling fractions were calculated using the same equation used to calculate the disorder. This calculation was performed at the middle of the target, i.e., where the crystal structure is pristine, which means that there is no source for direct scattering events. Thus, the backscattering yield (except the yield that can be found in pristine samples) in the corresponding energy-window is solely due to the dechanneling induced by defects at the target surface.

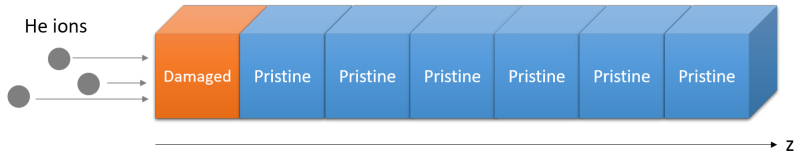

Figure 4.23 – Illustration of the connection of MD cells. Damaged and pristine cells are represented by orange and blue boxes, respectively. The damaged cell is located at the surface.

In the second method (denoted as M2), we first calculated the critical angle for pristine Fe with different He ion energies. More precisely, we used the half angle, $\psi_{1/2}$, which was calculated in the same way as that in Fig.A.1 by averaging over all ϕ_n. The values of $\psi_{1/2}$ are listed in Table.III. We then used, one by one, the pristine and defective MD cells and we determined the angular distribution of He ions after their passing through the cells. Fig.4.25 presents examples of such polar angle distributions for the $L1000$ Fe MD cell and for He energies ranging from 1 MeV to 5 MeV. If the polar angle of an ion is larger than $\psi_{1/2}$, this ion is considered as a dechanneled ion. Then, the dechanneling fraction is calculated as the ratio of the number of dechanneled ions to the number of probing ions. Note that in the calculation of the dechanneling fraction in M1, the contribution from a pristine target is subtracted (because values as normalized to that of a pristine cell, as in the case of the disorder fraction). Here, for the M2 method, the dechanneling fraction of a pristine cell is also removed (by a simple subtraction).

Table III – Half angles measured from the pristine Fe MD cell with different He ion energies.

Energy (MeV)	1.0	1.4	2.0	2.6	3.0	3.6	4.0	5.0
$\psi_{1/2}$ (°)	1.2	1.0	0.84	0.75	0.70	0.65	0.61	0.55

The dechanneling fractions calculated from cells containing interstitial point defects, namely $I1$ and $R10$ MD cells, are presented in Fig.4.26.(a) and Fig.4.26.(b), respectively. Note that since the dechanneling fraction induced by RDAs would be too small for a concentration of 1 %, here, we used a cell containing 10 % of RDAs. In these figures,

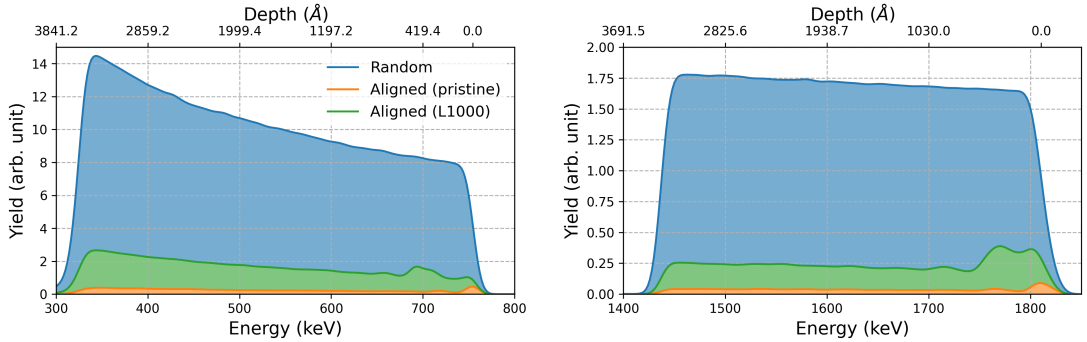

(a) 1000 keV **(b)** 2400 keV

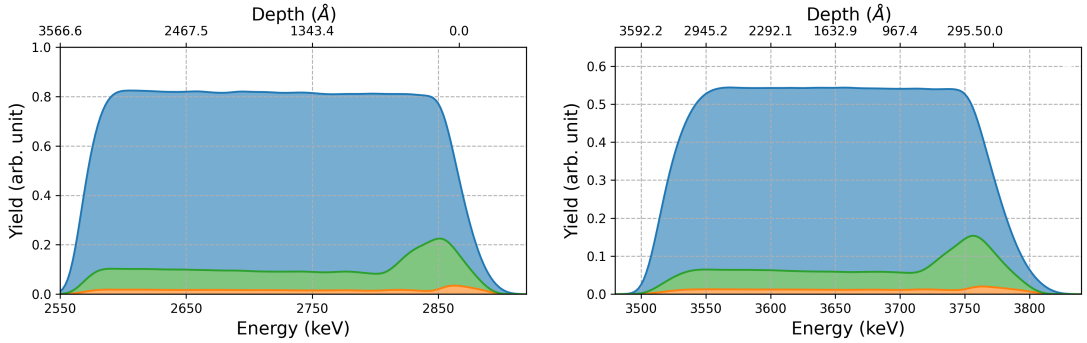

(c) 3800 keV **(d)** 5000 keV

Figure 4.24 – RBS/C spectra generated from He ions on <001>-oriented Fe targets created manually. The He energies in (a-d) are 1000, 2400, 3800 and 5000 keV, respectively. The orange spectra were calculated from aligned configurations, in which the target was created by connecting 7 pristine cells along the z direction. The green spectra were calculated from aligned configurations, in which that target was created by connecting 1 $L1000$ cell with additional 6 consecutive cells. The blue spectra were calculated from random configurations.

the blue and orange circles represent the values calculated from the M1 and M2 methods, respectively. As it will be explained hereafter, we chose to plot the dechanneling fractions for these defects as a function of E^{-1}. The fits represented by the dashed lines show that this dependence is effective. The slopes of the fits and the RMSD values are listed in the figure legends. For the two types of point defects studied here, the dechanneling fraction decreases with increasing energy; more specifically, it increases with E^{-1}. This behavior is exactly the one discussed in Sec.2.1.2. It is due to the decrease of the dechanneling cross section with a higher ion energy according to Eq.(2.12). For the case of $I1$, the values calculated from M2 are slightly smaller than those obtained from M1, which is most likely originating from an interface effect between the connected cells. Indeed, atomic rows in a defective cell may not be perfectly aligned with those in a connected pristine cell, and this artifact can be considered as a stacking fault inducing an additional dechanneling ion contribution. This phenomenon is not observed in the case of RDAs because these

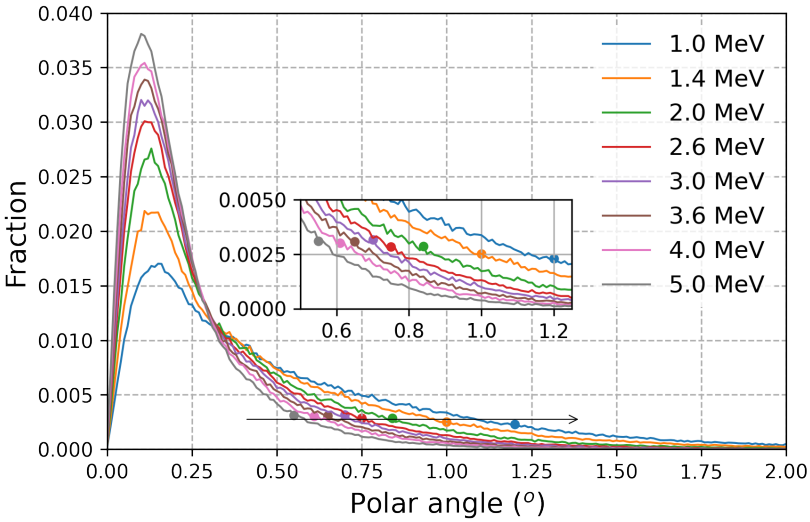

Figure 4.25 – Polar angle distributions of He ions after passing through the $L1000$ cell. The distributions with different He energies are represented by different colors. The black arrow is used as a guide for the eyes. Note that from the left to the right side, the He energy decreases from 5 MeV to 1 MeV. The dot on each distribution indicates the fraction of ions at the corresponding critical angle. Inset provides a zoomed view.

latter do not create any distortion in their vicinity (they would probably have if the cells containing these defects had been relaxed).

The dechanneling fractions calculated from the Fe MD cells containing dislocation loops ($L830$, $L896$ and $L1000$) are presented in Fig.4.27. Note that in this figure, the energy-scale is linear (and not in E^{-1} or $E^{1/2}$). The dechanneling fractions calculated from M1 and M2 methods are represented by the blue and orange triangles, respectively. The discrepancy between the values obtained from the two methods still occurs here, and a same explanation as for the point defects can hold. It can be noticed that the dechanneling fraction induced by dislocation loops is much larger (by around one decade) than that induced by an equivalent quantity of point defects (i.e., $I1$), which makes sense, owing to the very characteristics of those defects and their significant distortion induced on the surrounding crystalline lattice.

Data of Fig.4.27 were fitted with a power-law of the type E^n, and the best fits provided values of n ranging from -1 to -0.3, depending on the defect type and the method of calculation. This energy dependence appears to be quite striking, as theoretical treatments led to a dechanneling fraction proportional to $\sqrt{E}$, as indicated in Eq.(2.13)). But this discrepancy does not imply that either the theoretical derivations nor our results are wrong. It is actually more likely that different definitions of the dechanneling fraction were used.

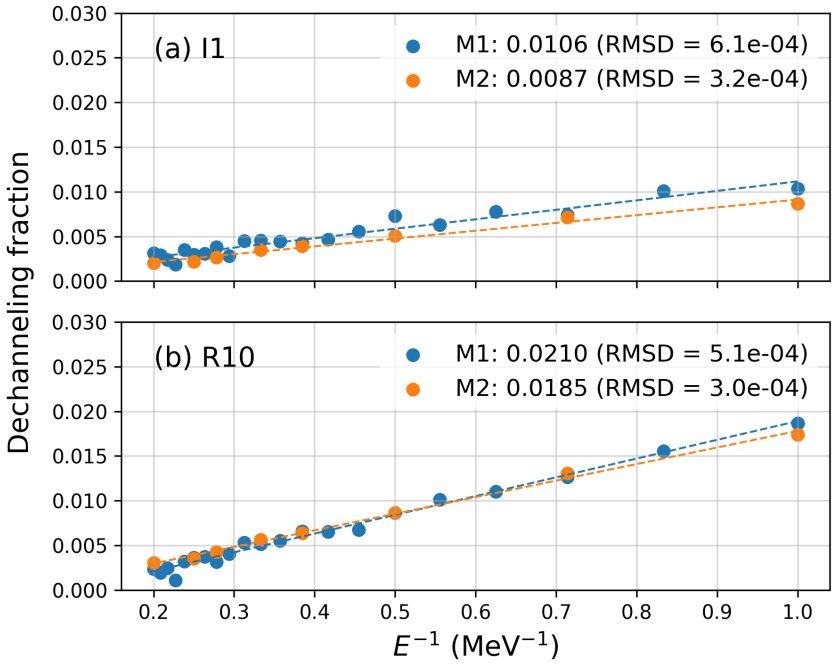

Figure 4.26 – Dechanneling fractions as a function of E^{-1} calculated from the Fe MD cells containing (a) $I1$ and (b) $R10$. The blue and orange circles represent the values calculated from M1 and M2, respectively. The fits are represented by the linear dashed lines. The slopes of the linear lines are the numbers following the symbol of M1 or M2 in the legend. The RMSDs of the fits are also provided in the legend.

In order to validate this statement, let's assume two particular scenarios, illustrated in Fig.4.28. In scenario A, we consider a target with point defects only, and no lattice distortions (i.e. no dislocation of any type). If after a collision with a point defect, the deflection angle of the probing ion is larger than the critical angle, the (originally channeled) ion becomes a dechanneled one. We will refer to this process as to the *global dechanneling*. In scenario B, we consider, opposite to scenario A, a target containing lattice distortions only, and no point defects. When an originally channeled ion arrives at a distorted region, it can be classified as a dechanneled ion if the angle between its moving direction and the distorted channel is larger than the critical angle. We will refer to this process as to the *local dechanneling*. But in fact, what really happens in this situation depends on the rest of the ion path. If the deflection angle after the interaction with the distorted region is larger than the critical angle, then the ion is effectively dechanneled in the bulk pristine region behind, and we come back to the *global dechanneling* above-presented. If the deflection angle allows the ion to be re-channeled in the bulk pristine region, then there is finally no dechanneling; this effect is called the transparency effect [187]. In short, global indicates that dechanneling will occur anywhere in the target, while local suggests that ions may be classified as dechanneled ions in distorted regions, but

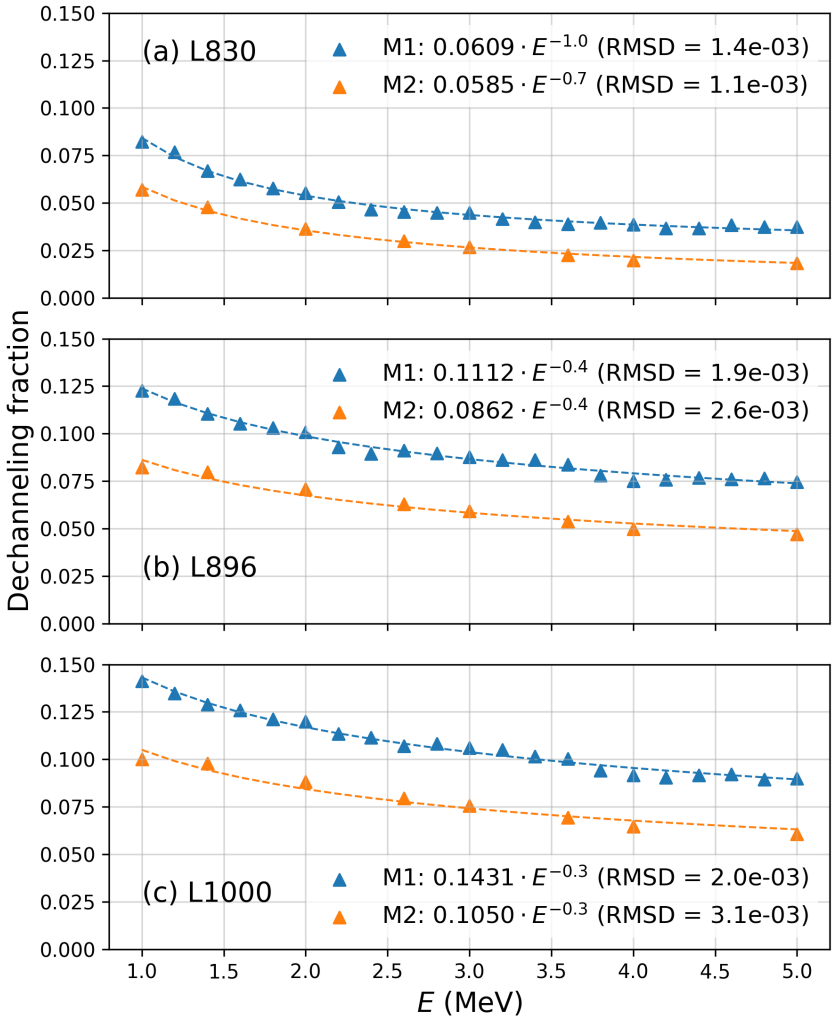

Figure 4.27 – Dechanneling fractions as a function of E calculated from the (a) $L830$, (b) $L896$ and (c) $L1000$ Fe MD cells. The blue and orange triangles represent the values calculated using the M1 and M2 methods, respectively. The fits are represented by the dashed lines. The slopes, exponents and RMSD of the fits are the numbers following the symbol of M1 or M2 in the legend.

may be designated as channeled ions in other regions, for example, in pristine regions.

Both our M1 and M2 methods evaluate the *global dechanneling*, whereas theoretical treatments of the dechanneling induced by dislocations, as reported in the literature, refer to the *local dechanneling*. The most accurate definition seems to be the *global dechanneling* because it studies probing ions after their passing through the damaged layer. In contrast, the *local dechanneling* relies on an a priori assumption, and the dechanneling is assumed before the interaction with the distorted region occurs. But for this reason, the *local dechanneling* appears to be a sound estimation of the density of the local distortions and thus of the dislocation density.

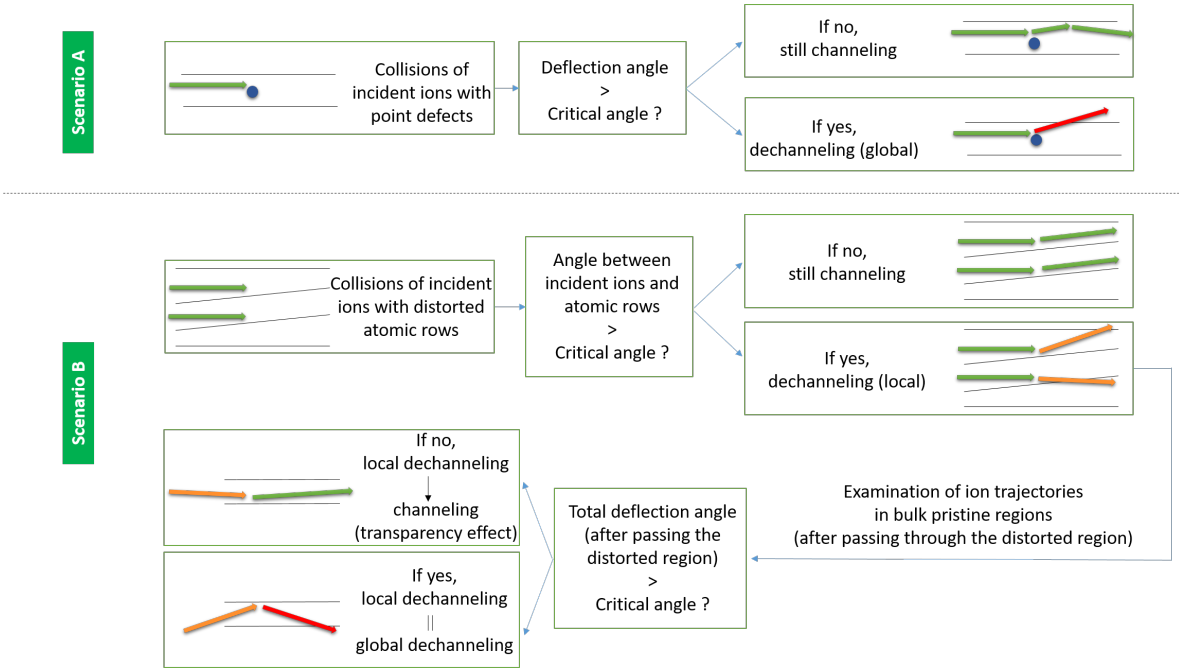

Figure 4.28 – Illustration of dechanneling induced by point defects and dislocations presented in scenario A and B, respectively. Horizontal and inclined black lines represent pristine and distorted atomic rows, respectively. Point defects are represented by blue circles. Beams of incident ions in channeling, global dechanneling and local dechanneling conditions are denoted by green, red and orange arrows, respectively.

The difference in the dechanneling descriptions appears as one highly plausible reason to explain why our simulation results conflict with theoretical predictions, but this is not the sole one. Another reason is the difference in the damaged thickness. For thin layers, as those we are dealing with in this work, when we estimate the disorder fraction f_d, we are in fact measuring the distortion density and thus the *local dechanneling*, which is why we observe a dependence of f_d with $E^{1/2}$ in the presence of dislocations. When estimating the global dechanneling, we find a dependence with E^{-1} for the point defects, as expected (see ref.[180] and scenario A in Fig.4.28); for dislocations, it is observed an energy dependence that arises from the $E^{1/2}$ dependence strongly affected by the transparency effect which is important (hence, dislocations could be partly considered as a collection of point defects, and the actual power-law coefficient may be a mixture between 1/2 and -1). For thick layers, as in most experiments, although the concept of *local dechanneling* is used (since the dechanneling fraction is determined in the energy (or depth) range corresponding to the damaged layer, not behind, in the pristine part of the crystal), the values of *local dechanneling* and *global dechanneling* could be similar when the transparency effect is negligible. Therefore, the dependence of the backscattering yield with $E^{1/2}$ is, in the literature, observed for dislocations, as we would most likely have found if we had used a much larger MD cell to determine the *global dechanneling*. We can then conclude

that theoretical derivations of the dechanneling fraction, experimental estimations of this quantity and our simulation data can be reconciled if one considers that there exists two different descriptions of the dechanneling fraction, and that their correct evaluation procedure depends on the thickness of the damaged layer that is under investigation.

4.4 Summary

In the first study using UO_2 MD cells containing defects created by the FPA method, we generated elastic strain kinetics and disordering kinetics from the simulation of XRD and RBS/C signals. Qualitatively, those simulated kinetics show good agreement with experimental ones, which indicates that the approach we developed is valid. Furthermore, we established direct connections between both quantity and nature of defects on the one hand and XRD and RBS/C signals on the other hand. Thus, it is now possible to infer the type of dominant defects in irradiated materials exhibiting a similar behavior as UO_2 (e.g. most of fluorite-structure materials but also MgO) without having to perform the MD simulations, but simply using experimental data. In this regard, XRD and RBS/C can be used interchangeably for the determination of the disordering kinetics. Nonetheless, the study of the elastic strain may provide complementary information on the microstructure, for instance regarding defects that affect the most the lattice parameter (e.g. point defects and Frank loops). In addition, the two techniques show different sensitivities to the various defects encountered in the irradiated materials. These findings demonstrate that the use of the two techniques can be effective in terms of providing a comprehensive description of crystals containing complex defects.

In the second study using model defective Fe MD cells, we examined the response of XRD and RBS/C signals induced by different types of defects. We found that both disorder and strain induced by vacancies is essentially null. From interstitial point defects to dislocation loops, the elastic strain decreases, while the disorder tends to be higher, irrespective of the technique used. These variations of elastic strain and disorder have a good correspondence with that observed in UO_2. The response of RBS/C to interstitials and dislocation loops was further investigated by varying the energy of the probing ions. In order to interpret our results, we introduced, in addition to our disorder fraction parameter, two forms of dechanneling processes, the *global* and the *local dechanneling*. We showed that usual analytical treatments of the RBS/C signals generated from targets containing dislocations refer to the latter, while methods that we developed evaluate the former. Comparing results from the literature and (all) our results, we managed to reconcile the different approaches. One important output is that we confirmed that the backscattering yield (we use this quantity because it involves no modeling) increases with

$E^{1/2}$ when the crystal contains dislocations.

Conclusions and perspectives

In order to have a better use of energetic particles, it is imperative to have a comprehensive understanding of the mechanisms related to irradiation-induced effects. For this purpose, both computational and experimental approaches can provide valuable insights. In this thesis, we applied computational RBS/C and XRD methods to characterize irradiation-induced effects by determining some phenomenological parameters, i.e., disorder and elastic strain. We not only explored the evolution of these parameter with irradiation fluence in certain materials (e.g., UO_2), but also highlighted the connection between these parameters and irradiation-induced defects. Some computational results have been confronted with experiments.

The computational RBS/C and XRD signals were mainly generated from targets containing realistic defects, i.e., cells obtained from MD simulations. In order to emulate experimental signals as accurately as possible, we improved a recently developed RBS/C simulation code called RBSADEC in the following aspects:

- In the RBSADEC code, when an incident ion collides with a target atom, a virtual backscattered ion is generated, which then moves towards the detector and may eventually give rise to RBS/C signals. The interaction of this virtual backscattered ion with target atoms is described by an algorithm that considers the target to be amorphous. We improved this algorithm by providing alternative methods for the calculations of FFPs and impact parameters. After the improvement, the random spectrum generated by this code can better fit the experimental one;

- Efforts have also been made to improve the simulation of aligned spectra. The first one is that we realized that the original analytical method for calculating target atomic thermal vibration magnitude using the Debye temperature cannot give satisfactory results for both the U and O atoms at the same time. Thus, we propose to use the values obtained from experiments that can distinguish the vibration magnitudes of U and O atoms, such as RBS/C and XRD experiments. The second one is to introduce a fitting parameter called the minimum interatomic potential that provides a cut-off distance for the interaction of incident ions and

target atoms. It can affect the search of collision partners and thus is able to modify the shape of the aligned spectra;

- In RBS/C simulations, the type of incident ion beam divergence has a non-negligible effect on the simulation of an aligned spectrum. Thus we provided additional beam divergence types to enhance the flexibility of this code, especially when the code is used to compare with others.

After the improvement of the RBSADEC code, we computed RBS/C signals as well as XRD signals from UO_2 MD cells containing defects. The defects in the UO_2 MD cells were created by the FPA method, which includes point defects (e.g., vacancies and interstitials) and extended defects (e.g., dislocation loops and lines). The computed disordering and elastic strain kinetics from the UO_2 cells exhibit distinct features from low to high irradiation fluence, which show good qualitative agreements with experimental ones. Since we know the types and quantities of defects in the UO_2 cells, we established a direct connection between the defect and the phenomenological parameters by decomposing the kinetics to different components, each of which is induced by one single type of defect. This connection could allow a quick determination of the type of dominant defect in real samples from experimental kinetics.

While we managed to separate the effect of different types of defects in the UO_2 cells, clearer insight can be gained by conducting computations with MD cells containing one single type of defects. For this purpose, a set of Fe MD cell was prepared for a systematic study. The simulation results show that an evolution of interstitials to dislocation loops would lead to a decrease of the elastic strain. On the contrary, the same evolution would induce an increase of the disorder. An evolution of vacancies to voids would lead to a significant increase of the elastic strain, but has little effect on the disorder. Compared to RDAs, interstitials can induce larger elastic strain and disorder. In addition, we explored the variation of RBS/C signals with different energies of He ions. For point defects, the disorder fraction remains constant or slightly increases with a higher He ion energy, but for dislocation loops, the disorder fraction clearly increases as the square root of He ion energy. In terms of dechanneling fraction, values both point defects and dislocations loops decrease with higher energy, but with different dependencies.

More research works can be expected in the future. On the computational side, a systematic study in UO_2, like that in Fe, can be performed to confirm the results obtained from the decomposition of disordering and elastic strain kinetics; defects can also be generated in Fe MD cells using the FPA method, which allows the computation of disordering and elastic strain kinetics in Fe as those in UO_2. After studying a ceramic oxide and a metal, one would like to consolidate the global approach by investigating a covalent

material that undergoes amorphization upon irradiation. In the current simulations, the size of MD cells remains small compared to that of real samples. Efforts can be made to increase the MD cell size, for example by properly connecting MD cells, in order to mimic experimental XRD and RBS/C spectra in addition to the phenomenological parameters. On the experimental side, ion irradiation of Fe is being performed. We can hope that RBS/C and XRD techniques will be used to characterize disorder and elastic strain for the purpose of confronting the results of future simulations using Fe MD cells.

Appendix A

Dechanneling fractions in RBS/C spectra generated from UO_2 MD cells

In the calculation of the disorder fractions in the UO_2 MD cells using RBS/C simulations, we assumed that the contribution of dechanneled particles to the increase of the yield in the damaged samples is negligible, because of the thin thickness of the cells. Thus, we used Eq.(2.10) to estimate the disorder fraction, instead of using Eq.(2.9) which takes into account the effect of dechanneling. However, the analysis of defects, as shown in Fig.4.2, indicates that dislocations are dominant defects in the high dpU region, which is supposed to mainly induce dechanneling, according to the literatures [180]. Therefore, it is necessary to check if the effect of dechanneling in these cells is really negligible.

As mentioned in Sec.2.1.1, if the moving direction of an ion with respect to the channeling direction is larger than a critical angle, then the ion is considered to be dechanneled. One type of critical angle, denoted as $\psi_{1/2}$, can be measured via an angular scan by adjusting the angle between the channeling direction and the direction of incident ions. Fig.A.1 presents angular scans performed by using the pristine MD cells with the channeling direction along the [001] direction. Since the critical angle depends on the nature of incident ions, we used the same ions as those used in the disorder measurements, which are 3.085 MeV He ions. The blue dotted line represents the change of yield as a function of the polar angle θ_n of the incident ions, in which, for the measurement at each polar angle, the yield is measured and averaged over all the azimuthal angles ϕ_n. The orange and green dotted lines represent the scans along θ_n, while ϕ_n is set to 13° and 15°, respectively. It can be readily observed that, when θ_n is close to 0°, the yield is low, which corresponds to the yield in the aligned configuration, y_a. For the blue spectrum, with a larger value of θ_n, the yield increases and approaches a steady value, which corresponds to the yield in the random configuration, y_r. In contrast, the orange and green spectra

exhibit a shoulder-like region, in which the yield is higher than that in the blue spectrum and it shows a peak. These features can be explained by the fact that an ion moving along certain directions can encounter more atoms than those moving in an amorphous target. With a higher value of θ_n, the yields of the orange and green spectra also gradually approach that of the blue spectrum. Eventually, the $\psi_{1/2}$ is defined as the angle at which position the yield equals the average of y_a and y_r. For the condition of 3.08 MeV He ions on the pristine UO_2 MD cell along the [001] direction, the $\psi_{1/2}$ is measured as 0.8 degree.

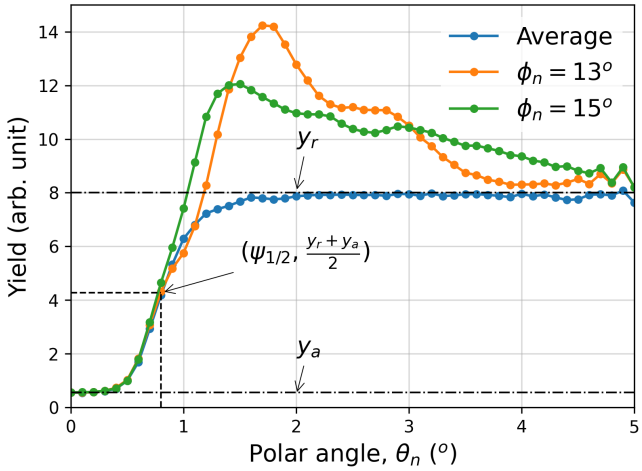

Figure A.1 – Angular scans performed on the pristine UO_2 MD cell using 3.085 MeV He ions along the [001] direction. The blue dotted line represents the scan in which the yield is averaged over all ϕ_n. For the scans represented by the orange and green dotted lines, the yields are measured by setting ϕ_n to 13° and 15°, respectively.

Knowing the value of $\psi_{1/2}$, we modified the RBSADEC code to distinguish the ions with an angle between their moving direction and the [001] direction smaller and larger than $\psi_{1/2}$: the former contribute to the increase of the yield through direct scattering; whereas the latter contribute to the increase of the yield through dechanneling. In this way, we can take into account the effect of dechanneling and calculate the disorder according to Eq.(2.9). Fig.A.2 shows the disordering kinetics obtained from the RBS/C simulations along the [001] direction of the UO_2 MD cells neglecting (blue) and taking into account (orange) the effect of dechanneling. Taking into account dechanneling leads to a decrease in disorder, because the contribution of dechanneling to the yield is rejected in Eq.(2.9). However, the decrease of the disorder is so small that it is valid to estimate the value of disordering by neglecting the influence of dechanneling in these MD cells. It is not surprising that there are large fractions of direct scattering, even in the cells containing dislocations. The visualization of the U atoms in the cells, as shown in Fig.4.1.(c) and (d), indicates that the distortion of the U lattice induced by dislocations is so strong that

some channels are clearly blocked by displaced atoms. In a pristine sample, surface atoms can shadow the atoms in a greater depth from the small-impact-parameter-collisions with incident ions. However, the effect of shadowing diminishes significantly in the cells severely distorted by dislocations. Thus, the displaced atoms in the distorted cells are exposed to the incident beam and can contribute to the increase of RBS/C yield through direct scattering.

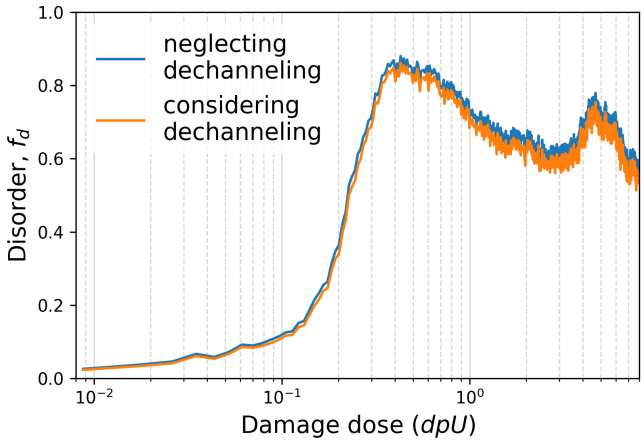

Figure A.2 – The disordering kinetics of the UO_2 MD cells obtained from the RBS/C simulations along the [001] direction without (blue) and with (orange) considering the effect of dechanneling.

Appendix B

Models of the disorder build-up

Over the past decades, several models for describing irradiation-induced amorphization have been developed [269], including the direct-impact [262], cascade-overlap [262], direct-impact/defect-stimulated models [270], etc. With the increase of irradiation fluence, the disorder fractions eventually saturate at 1 in these models, which indicates the full amorphization of the sample. If the target does not amorphize (i.e., the disorder saturates at a value smaller than 1), it is possible to multiply the functions of these models with a constant smaller than 1 to describe the disorder build-up. However, it is difficult to directly apply these models to describe the specific disordering kinetics in UO_2, which exhibits a complex profile. One model that is able to tackle this kind of complex disorder build-up is the so-called multi-step damage accumulation (MSDA) model, which assumes that the damage accumulation can be separated into different steps and the accumulation in each step is described by the direct-impact model [271–273]. This model has been used to describe the damage accumulation in YSZ, which has similar profiles of disordering kinetics to that of UO_2, as mentioned previously.

Apart from the MSDA model, a modified version of the cascade-overlap model, which contains the information related to the "multi-step damage" by its very definition, can be used to describe the build-up of disorder in UO_2. The original cascade-overlap model

is derived from a series of coupled differential equations as follows:

$$df_0 = -\sigma f_0 d\phi \tag{B.1a}$$
$$df_1 = \sigma(f_0 - f_1)d\phi \tag{B.1b}$$
$$\vdots$$
$$df_i = \sigma(f_{i-1} - f_i)d\phi \tag{B.1c}$$
$$\vdots$$
$$df_n = \sigma(f_{n-1} - f_n)d\phi \tag{B.1d}$$
$$df_a = \sigma f_n d\phi \tag{B.1e}$$

where ϕ represents a fluence-like quantity (for example, dpU, Frenkel pairs per area, incident ions per area, etc), σ represents the cross section of damage (its unit depends on that of ϕ), f_0 is the undamaged fraction, f_i $(i = 1, ..., i, ...n)$ represents the corresponding fraction of areas being damaged (e.g., by collision cascades, by Frenkel pairs in the UO_2 MD cells, etc.) i times, f_a is the final amorphization fraction after being damaged $n+1$ times (note that $n+1$ times of damage correspond to n times of damage-overlap). According to Eq.(B.1), the function f_a can be derived as:

$$f_a = 1 - (\sum_{k=0}^{n} \frac{(\sigma\phi)^k}{k!} e^{-\sigma\phi}) \tag{B.2}$$

From the above equations, we can realize that the growth of disorder is not only decided by the final amorphization fraction f_a, but is also contributed by the fraction of damaged areas f_i. Furthermore, with a higher number of damaged time i, the corresponding profile of f_i would have a longer incubation time. By this way, the onset fluences of f_i are separated, which resembles the feature of "multi-step" in the MSDA model. Therefore, we can use the functions f_i to describe the disorder build-up which occurs before the final saturation of disorder decided by f_a. In order to take into account the fact that UO_2 is non-amorphizable, f_i and f_a must be scaled to adjust the maximum level of disorder. Thus, the functions of this modified cascade-overlap model, f_d^i $(i = 1, ..., i, ...n)$ and $f_d^{a,n}$

are calculated by:

$$f_d^1 = c_1 \sigma\phi e^{-\sigma\phi} \tag{B.3a}$$

$$\vdots$$

$$f_d^i = c_i \frac{(\sigma\phi)^i}{i!} e^{-\sigma\phi} \tag{B.3b}$$

$$\vdots$$

$$f_d^n = c_n \frac{(\sigma\phi)^n}{n!} e^{-\sigma\phi} \tag{B.3c}$$

$$f_d^{a,n} = c_a[1 - (\sum_{k=0}^{n} \frac{(\sigma\phi)^k}{k!})e^{-\sigma\phi}] \tag{B.3d}$$

where c_i $(i = 1, ..., i, ...n)$ and c_a are the corresponding scaling constants.

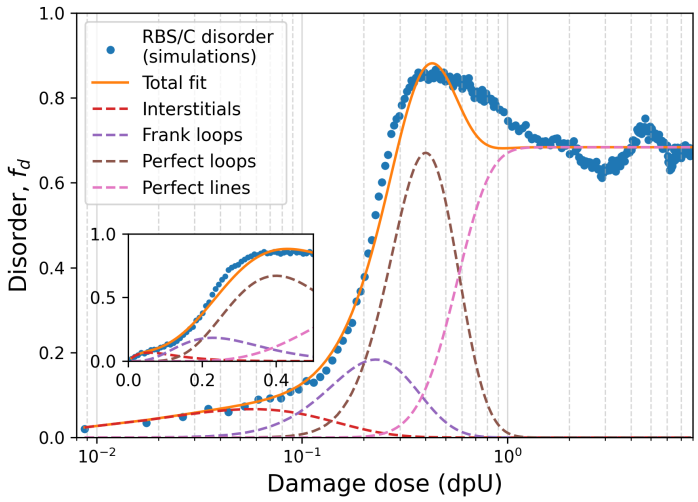

Figure B.1 – Fit of the simulated disordering kinetics generated from UO_2 MD cells using the modified cascade-overlap model. Blue dots represent the disordering kinetics obtained from the RBS/C simulation and averaged over the three <001> directions. The solid line represents the total fit by combining contributions of the different defects (dashed lines). Insets use a linear scale for the x axis. (In order to avoid a dense overlap, only one value in every five simulation results is shown when the fluence is larger than 1.0 dpU.)

Fig.B.1 presents the fit of the simulated disordering kinetics generated from UO_2 MD cells. It was obtained from the RBS/C simulations using the modified cascade-overlap model. The fit was performed by using the non-linear least squares method. The fitting functions and corresponding constants are listed in Table I. In this case, ϕ represents dpU and σ is a unit-less quantity which equals to 17.5.

Table I – Functions, f_d^i and $f_d^{a,n}$, and disorder constants, c_i, used in the modified cascade-overlap model to fit the disordering kinetics obtained from the RBS/C simulations.

	Interstitials	Frank loops	Perfect loops	Perfect lines
$f_d^i(RBS/C)$	f_d^1	f_d^4	f_d^7	$f_d^{a,9}$
$c_i(RBS/C)$	0.18 ± 0.04	0.94 ± 0.13	4.50 ± 0.09	0.68 ± 0.00

Now, we can present how the *ad hoc* method used in Fig.4.10 was applied. According to the fit using the modified cascade-overlap model, the kinetics induced by the perfect lines can be described by the Eq.(B.3d), which is sigmoidal-like. Since, in Fig.4.10, we assumed a linear relationship between the disorder and defect quantity, we multiplied $f_d^{a,n}$ with a constant C_p to determine the density of perfect lines ρ_p^{line}. Thus, a complete form of Eq.(4.4) is given by:

$$f_d = r_I C_I + r_F \rho_F + r_p^{loop}[\rho_p - r_p^{line} \cdot (C_p \cdot f_d^{a,n})] + r_p^{line} \cdot (C_p \cdot f_d^{a,n}) \tag{B.4}$$

Note that since we used the quantities of defects given in Fig.4.2, the fitting parameters of perfect lines ($n = 13$, $c_a = 1$ and $\sigma = 16.6$) derived from Eq.(B.4) are different with those calculated from the modified overlap model. Finally, the fitted densities of perfect loops and lines are presented in Fig.B.2, which is for the case of the RBS/C simulations in Fig.4.10. The value of C_p is 2.6×10^{17} m^{-2}.

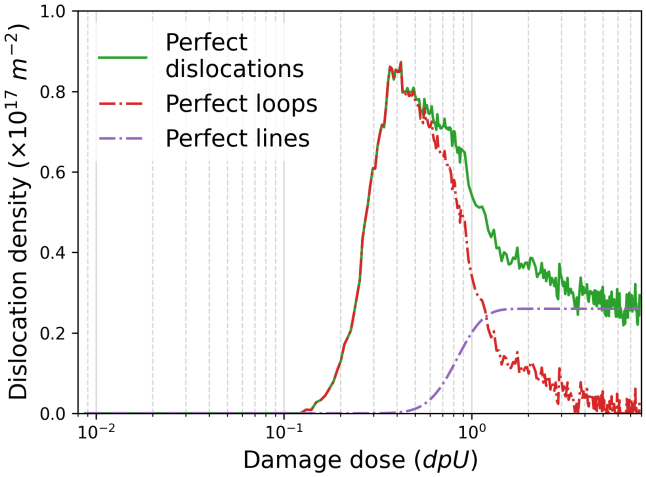

Figure B.2 – The densities of perfect loops and lines obtained according to the fit of the disordering kinetics presented in Fig.4.10.(a).

References

[1] Bame, S. J., Hundhausen, A. J., Asbridge, J. R. & Strong, I. B. Solar wind ion composition. *Physical Review Letters* **20**, 393–395 (1968).

[2] Hundhausen, A. J., Bame, S. J., Asbridge, J. R. & Sydoriak, S. J. Solar Wind Proton Properties. Vela 3 Observations From July 1965 To June 1967. *Journal of Geophysical Research* **75**, 4643–4657 (1970).

[3] Alfvén, H. On the Electric Field Theory of Magnetic Storms and Aurorae. *Tellus* **7**, 50–64 (1955).

[4] McIlwain, C. E. Direct measurement of particles producing visible auroras. *J. Geophys. Res.* **65**, 2727–2747 (1960).

[5] Alfvén, H. On the Theory of Comet Tails. *Tellus* **9**, 92–96 (1957).

[6] Biermann, L., Brosowski, B. & Schmidt, H. U. The interaction of the solar wind with comets. *Solar Physics* 254–284 (1967).

[7] Rubin, L. & Poate, J. Ion implantation in silicon technology. *The Industrial Physicist* **9**, 12–15 (2003).

[8] Chason, E. *et al.* Ion beams in silicon processing and characterization. *J. Appl. Phys.* **81**, 6513–6561 (1997).

[9] Zhu, J. G., White, C. W., Budai, J. D., Withrow, S. P. & Chen, Y. Growth of Ge, Si, and SiGe nanocrystals in SiO_2 matrices. *Journal of Applied Physics* **78**, 4386–4389 (1995).

[10] Banhart, F. & Ajayan, P. M. Carbon onions as nanoscopic pressure cells for diamond formation. *Nature* **382**, 433–435 (1996).

[11] Warner, J. H. *et al.* Structural transformations in graphene studied with high spatial and temporal resolution. *Nat. Nanotechnol.* **4**, 500–504 (2009).

[12] Krasheninnikov, A. V. & Nordlund, K. Ion and electron irradiation-induced effects in nanostructured materials. *J. Appl. Phys.* **107** (2010).

[13] Peng, B. *et al.* Measurements of near-ultimate strength for multiwalled carbon nanotubes and irradiation-induced crosslinking improvements. *Nat. Nanotechnol.* **3**, 626–631 (2008).

[14] Gómez-Navarro, C. *et al.* Tuning the conductance of single-walled carbon nanotubes by ion irradiation in the Anderson localization regime. *Nat. Mater.* **4**, 534–539 (2005).

[15] Talapatra, S. *et al.* Irradiation-induced magnetism in carbon nanostructures. *Phys. Rev. Lett.* **95**, 15–18 (2005).

[16] Was, G. S. Challenges to the use of ion irradiation for emulating reactor irradiation. *J. Mater. Res.* **30**, 1158–1182 (2015).

[17] Zinkle, S. J. & Snead, L. L. Opportunities and limitations for ion beams in radiation effects studies: Bridging critical gaps between charged particle and neutron irradiations. *Scr. Mater.* **143**, 154–160 (2018).

[18] Stork, D. *et al.* Towards a programme of testing and qualification for structural and plasma-facing materials in 'fusion neutron' environments. *Nucl. Fusion* **57** (2017).

[19] Maurette, M. & Price, P. B. Electron Microscopy of Irradiation Effects in Space. *Science* **187**, 121–129 (1975).

[20] Bringa, E. M. *et al.* Energetic Processing of Interstellar Silicate Grains by Cosmic Rays. *ApJ* **662**, 372–378 (2007).

[21] Nagao, K. *et al.* Irradiation History of Itokawa Regolith Material Deduced from Noble Gases in the Hayabusa Samples. *Science* **333**, 1128–1131 (2011).

[22] Starukhina, L. V. & Shkuratov, Y. G. The Lunar Poles: Water Ice or Chemically Trapped Hydrogen? *Icarus* **147**, 585–587 (2000).

[23] Pieters, C. M. *et al.* Character and spatial distribution of OH/H_2O on the surface of the moon seen by M^3 on chandrayaan-1. *Science* **326**, 568–572 (2009).

[24] Nuclear Power Reactors in the World. Tech. Rep., International Atomic Energy Agency, Vienna (2019).

[25] Zinkle, S. J. & Was, G. S. Materials challenges in nuclear energy. *Acta Mater.* **61**, 735–758 (2013).

[26] Chopra, O. K. & Rao, A. S. A review of irradiation effects on LWR core internal materials - Neutron embrittlement. *Journal of Nuclear Materials* **412**, 195–208 (2011).

[27] Mansur, L. K. Theory and experimental background on dimensional changes in irradiated alloys. *J. Nucl. Mater.* **216**, 97–123 (1994).

[28] Scott, P. A review of irradiation assisted stress corrosion cracking. *Journal of Nuclear Materials* **211**, 101–122 (1994).

[29] Fyfitch, S. *Corrosion and Stress Corrosion Cracking of Ni-Base Alloys*, vol. 4 (2020), 2nd edn.

[30] Bauer, N., Brecha, R. J. & Luderer, G. Economics of nuclear power and climate change mitigation policies. *Proceedings of the National Academy of Sciences of the United States of America* **109**, 16805–16810 (2012).

[31] Technology Roadmap Update for Generation IV Nuclear Energy Systems. Tech. Rep., Generation IV international forum (2014). URL https://www.gen-4.org/gif/upload/docs/application/pdf/2014-03/gif-tru2014.pdf.

[32] Zinkle, S. J. Advanced materials for fusion technology. *Fusion Engineering and Design* **74**, 31–40 (2005).

[33] Guerin, Y., Was, G. S. & Zinkle, S. J. Materials challenges for advanced nuclear energy systems. *MRS Bulletin* **34**, 10–14 (2009).

[34] Trinkaus, H. & Singh, B. N. Helium accumulation in metals during irradiation - Where do we stand? *J. Nucl. Mater.* **323**, 229–242 (2003).

[35] Bloom, E. E. *et al.* Critical questions in materials science and engineering for successful development of fusion power. *Journal of Nuclear Materials* **367-370 A**, 1–10 (2007).

[36] Diaz De La Rubia, T. & Gilmer, G. H. Structural transformations and defect production in ion implanted silicon: A molecular dynamics simulation study. *Phys. Rev. Lett.* **74**, 2507–2510 (1995).

[37] Petasecca, M., Moscatelli, F., Passeri, D., Pignatel, G. U. & Scarpello, C. Numerical simulation of radiation damage effects in p-type and n-type FZ silicon detectors. *IEEE Trans. Nucl. Sci.* **563**, 192–195 (2006).

[38] Li, Y. *et al.* Influence of fast neutron and gamma irradiation on the thermoelectric properties of n-type and p-type SiGe alloy. *J. Nucl. Mater.* **528**, 151856 (2020).

[39] Grove, W. R. On the electro-chemical polarity of gases. *Philosophical Transactions* **142**, 87–101 (1852).

[40] Betz, G. & Wien, K. Energy and angular distributions of sputtered particles. *International Journal of Mass Spectrometry and Ion Processes* **140**, 1–110 (1994).

[41] Jenkins, M. L. Characterisation of radiation-damage microstructures by TEM. *Journal of Nuclear Materials* **216**, 124–156 (1994).

[42] Zhang, Y., Debelle, A., Boulle, A., Kluth, P. & Tuomisto, F. Advanced techniques for characterization of ion beam modified materials. *Curr Opin Solid State Mater Sci* **19**, 19–28 (2015).

[43] Nordlund, K. Historical review of computer simulation of radiation effects in materials. *J. Nucl. Mater.* **520**, 273–295 (2019).

[44] Nordlund, K. *et al.* Primary radiation damage: A review of current understanding and models. *J. Nucl. Mater.* **512**, 450–479 (2018).

[45] Zhang, S. *et al.* Absence of single critical dose for the amorphization of quartz under ion irradiation. *J. Phys. Condens. Matter* **30**, 1–10 (2018).

[46] Granberg, F. *et al.* Mechanism of Radiation Damage Reduction in Equiatomic Multicomponent Single Phase Alloys. *Phys. Rev. Lett.* **116**, 1–8 (2016).

[47] Crocombette, J. P., Chartier, A. & Weber, W. J. Atomistic simulation of amorphization thermokinetics in lanthanum pyrozirconate. *Appl. Phys. Lett.* **88**, 1–3 (2006).

[48] Aidhy, D. S., Millett, P. C., Wolf, D., Phillpot, S. R. & Huang, H. Kinetically driven point-defect clustering in irradiated MgO by molecular-dynamics simulation. *Scr. Mater.* **60**, 691–694 (2009).

[49] Stukowski, A. Structure identification methods for atomistic simulations of crystalline materials. *Model. Simul. Mat. Sci. Eng.* **20**, 1–15 (2012).

[50] Stukowski, A. & Albe, K. Extracting dislocations and non-dislocation crystal defects from atomistic simulation data. *Model. Simul. Mat. Sci. Eng.* **18**, 085001 (2010).

[51] Zhu, H., Averback, R. S. & Nastasi, M. Molecular dynamics simulations of a 10keV cascade in β-NiAl. *Phil. Mag. A* **71**, 735–758 (1995).

[52] Zhang, S. *et al.* Simulation of Rutherford backscattering spectrometry from arbitrary atom structures. *Phys. Rev. E* **94**, 043319 (2016).

[53] Ayache, J., Beaunier, L., Boumendil, J., Ehret, G. & Laub, D. *Sample preparation handbook for transmission electron microscopy: Methodology* (Springer Science+Business Media, 2010).

[54] Wiss, T. *Radiation effects in UO_2*, vol. 2 (Elsevier Inc., 2012).

[55] Chartier, A. *et al.* Early stages of irradiation induced dislocations in urania. *Appl. Phys. Lett.* **109**, 181902 (2016).

[56] BOHR, N. the Penetration of Atomic Particles Through Matter. *Kgl. Danske Videnskab. Selskab. Mat.-Fys. Medd.* **18** (1948).

[57] Nastasi, M., Mayer, J. W. & Hirvonen, J. k. *Ion-solid interactions: fundamentals and applications* (Cambridge University Press, 1996).

[58] Biersack, J. & Haggmark, L. A Monte Carlo computer program for the transport of energetic ions in amorphous targets. *Nucl. Instrum. Methods* **174**, 257–269 (1980).

[59] Ziegler, J., Biersack, J. & Ziegler, M. *The Stopping and Range of Ions in Matter* (Chester, Maryland, 2015).

[60] Rutherford, E. LXXIX. The scattering of α and β particles by matter and the structure of the atom. *Philos. Mag.* **21**, 669–688 (1911).

[61] Griffiths, D. J. *Introduction to Quantum Mechanics* (Prentice Hall, 1995).

[62] Mott, N. F. The collision between two electrons. *Proc. R. Soc. Lond. A* **126**, 259–267 (1930).

[63] Lindhard, J., Schiøtt, H. E. & Scharff, M. Range concepts and heavy ion ranges (Notes on atomic collisions, II). *Kgl. Dan. Vidensk. Selsk., Mat.-Fys. Medd.* **33** (1963).

[64] Ziegler, J. F. SRIM. Available at http://www.srim.org/.

[65] Bragg, W. H. & Kleeman, R. XXXIX. On the α particles of radium, and their loss of range in passing through various atoms and molecules. *Philos. Mag.* **10**, 318–340 (1905).

[66] Simeone, D. & Luneville, L. DART version 1 user guide (2014). URL www.oecd-nea.org/tools/abstract/detail/nea-1885/.

[67] Luneville, L., Simeone, D., Baldinozzi, G., Gosset, D. & Serruys, Y. How to simulate the microstructure induced by a nuclear reactor with an ion beam facility : DART. *MRS Proceedings* **1215**, 1215–V13–03 (2009).

[68] Lindhard, J., Nielsen, V. & Scharff, M. Approximation method in classical scattering by screened Coulomb fields. *Kgl. Dan. Vidensk. Selsk., Mat.-Fys. Medd.* **36** (1968).

[69] Winterbon, B., Sigmund, P. & Sanders, J. B. Spatial distribution of energy deposited by atomic particles in elastic collisions. *Kgl. Dan. Vidensk. Selsk., Mat.-Fys. Medd.* **37** (1970).

[70] Winterbon, K. B. Heavy-ion range profiles and associated damage distributions. *Radiat. Eff.* **13**, 215–226 (1972).

[71] Thomson, J. XLII. Ionization by moving electrified particles. *Philos. Mag.* **23**, 449–457 (1912).

[72] Kunert, T. & Schmidt, R. Excitation and fragmentation mechanisms in ion-fullerene collisions. *Phys. Rev. Lett.* **86**, 5258–5261 (2001).

[73] Correa, A. A., Kohanoff, J., Artacho, E., Sánchez-Portal, D. & Caro, A. Nonadiabatic forces in ion-solid interactions: The initial stages of radiation damage. *Phys. Rev. Lett.* **108**, 1–5 (2012).

[74] Bohr, N., Bøggild, J. K., Brostrøm, K. J. & Lauritsen, T. Velocity-range relation for fission fragments. *Phys. Rev.* **58**, 839–840 (1940).

[75] Lindhard, J. & Scharff, M. Energy Dissipation by Ions in the kev Region. *Phys. Rev.* **124**, 128–130 (1961).

[76] Sugiyama, H. Modification of Lindhard-Scharff-Schiott Formula for Electronic Stopping Power. *J. Phys. Soc. Jpn.* **50**, 929–932 (1981).

[77] Firsov, O. B. A qualitative interpretation of the mean electron excitation energy in atomic collisions. *Sov. Phys. JETP* **36** (1959).

[78] Nastasi, M. & Tesmer, J. R. *Handbook of Modern Ion Beam Materials Analysis* (Materials Research Society, Pittsburgh, Pennsylvania,USA, 1995).

[79] Brandt, W. & Kitagawa, M. Effective stopping-power charge of ions in condensed matter. *Phys. Rev. B* **25**, 5631–5637 (1982).

[80] Doolittle, L. R. Algorithms for the rapid simulation of Rutherford backscattering spectra. *Nucl. Instrum. Methods Phys. Res., B* **9**, 344–351 (1985).

[81] RUMP stopping power modules. URL www.genplot.com/doc/RUMP/stp_inf.htm.

[82] Robinson, M. T. Basic physics of radiation damage production. *J. Nucl. Mater.* **216**, 1–28 (1994).

[83] Lilley, J. *Nuclear Physics: Principles and Applications* (Wiley, 2001), 1st edn.

[84] Greenwood, L. R. Neutron interactions and atomic recoil spectra. *J. Nucl. Mater.* **216**, 29–44 (1994).

[85] Krane, K. S. *Introductory Nuclear Physics* (Wiley, 1987), 3rd edn.

[86] X-5 Monte Carlo team. MCNP — A General Monte Carlo N-Particle Transport Code, Version 5 (2003).

[87] Petit, O., Hugot, F.-X., Lee, Y.-K., Jouanne, C. & Mazzolo, A. Tripoli-4 version 4 user guide. Tech. Rep., Commissariat à l'Énergie Atomique (2008).

[88] Chadwick, M. B. *et al.* ENDF/B-VII.1 nuclear data for science and technology: Cross sections, covariances, fission product yields and decay data. *Nucl. Data Sheets* **112**, 2887–2996 (2011).

[89] Susi, T., Meyer, J. C. & Kotakoski, J. Quantifying transmission electron microscopy irradiation effects using two-dimensional materials. *Nat Rev Phys* **1**, 397–405 (2019).

[90] Bethe, H. & Heitler, W. On the stopping of sast particles and on the creation of positive electrons. *Proc. R. Soc. Lond. A* **146**, 83–112 (1934).

[91] Compton, A. H. A quantum theory of the scattering of X-rays by light elements. *Phys. Rev.* **21**, 483–502 (1923).

[92] Warren, B. *X-Ray Diffraction* (Addison-Wesley, 1969).

[93] Zinkle, S. J. & Kinoshita, C. Defect production in ceramics. *J. Nucl. Mater.* **251**, 200–217 (1997).

[94] Wigner, E. P. Theoretical physics in the metallurgical laboratory of Chicago. *J. Appl. Phys.* **17**, 857–863 (1946).

[95] Kinchin, G. H. & Pease, R. S. The displacement of atoms in solids by radiation. *Rep. Prog. Phys.* **18** (1955).

[96] Robinson, M. T. The influence of the scattering law on the radiation damage displacement cascade. *Philos. Mag.* **12**, 741–765 (1965).

[97] Sigmund, P. A note on integral equations of the kinchin-pease type. *Radiat. Eff.* **1**, 15–18 (1969).

[98] Robinson, M. T. & Oen, O. S. On the use of thresholds in damage energy calculations. *J. Nucl. Mater.* **110**, 147–149 (1982).

[99] Lindhard, J., Nielsen, V., Scharff, M. & Thomsen, P. V. Integral equations governing radiation effects. *Kgl. Dan. Vidensk. Selsk., Mat.-Fys. Medd.* **33**, 1–42 (1963).

[100] Nordlund, K. *et al.* Improving atomic displacement and replacement calculations with physically realistic damage models. *Nat. Commun.* **9**, 1–8 (2018).

[101] Robinson, M. & Torrens, I. Computer simulation of atomic-displacement cascades in solids in the binary-collision approximation. *Phys. Rev. B* **9**, 5008–5024 (1974).

[102] Weber, W. J. & Zhang, Y. Predicting damage production in monoatomic and multi-elemental targets using stopping and range of ions in matter code: Challenges and recommendations. *Curr Opin Solid State Mater Sci* **23**, 100757 (2019).

[103] Crocombette, J.-p. & Wambeke, C. V. Quick calculation of damage for ion irradiation : implementation in Iradina and comparisons to SRIM. *EPJ Nucl. sci. technol.* **5**, 1–9 (2019).

[104] Stoller, R. E. *Primary radiation damage formation*, vol. 1 (Elsevier Inc., 2012).

[105] Brinkman, J. A. On the nature of radiation damage in metals. *J. Appl. Phys.* **25** (1954).

[106] Bacon, D. J. & Diaz de la Rubia, T. Molecular dynamics computer simulations of displacement cascades in metals. *J. Nucl. Mater.* **216**, 275–290 (1994).

[107] Diaz de la Rubia, T., Averback, R. S., Benedek, R. & King, W. E. Role of Thermal Spikes in Energetic Collision Cascades. *Phys. Rev. Lett.* **59**, 1930–1933 (1987).

[108] Crocombette, J. P., Van Brutzel, L., Simeone, D. & Luneville, L. Molecular dynamics simulations of high energy cascade in ordered alloys: Defect production and subcascade division. *J. Nucl. Mater.* **474**, 134–142 (2016).

[109] Plimpton, S. Fast parallel algorithms for short-range molecular dynamics. *Journal of Computational Physics* **117**, 1–19 (1995).

[110] LAMMPS. Available at http://lammps.sandia.gov.

[111] Devanathan, R., Diaz De La Rubia, T. & Weber, W. J. Displacement threshold energies in β-SiC. *J. Nucl. Mater.* **253**, 47–52 (1998).

[112] Stukowski, A. Visualization and analysis of atomistic simulation data with OVITO-the Open Visualization Tool. *Model. Simul. Mat. Sci. Eng.* **18**, 015012 (2010).

[113] Gibson, J. B., Goland, A. N., Milgram, M. & Vineyard, G. H. Dynamics of radiation damage. *Phys. Rev.* **120**, 1229–1253 (1960).

[114] Nordlund, K. & Averback, R. S. Inverse kirkendall mixing in collision cascades. *Phys. Rev. B* **59**, 20–23 (1999).

[115] Nordlund, K., Ghaly, M. & Averback, R. Defect production in collision cascades in elemental semiconductors and fcc metals. *Phys. Rev. B Condens. Matter Mater. Phys.* **57**, 7556–7570 (1998).

[116] Calder, A. F., Bacon, D. J., Barashev, A. V. & Osetsky, Y. N. On the origin of large interstitial clusters in displacement cascades. *Philos Mag (Abingdon)* **90**, 863–884 (2010).

[117] Sand, A. E., Dudarev, S. L. & Nordlund, K. High-energy collision cascades in tungsten: Dislocation loops structure and clustering scaling laws. *Epl* **103** (2013).

[118] Peng, Q. *et al.* Shockwave generates $< 100 >$ dislocation loops in bcc iron. *Nat. Commun.* **9** (2018).

[119] Nordlund, K. & Averback, R. Point defect movement and annealing in collision cascades. *Phys. Rev. B Condens. Matter Mater. Phys.* **56**, 2421–2431 (1997).

[120] Yi, X. *et al.* Direct observation of size scaling and elastic interaction between nano-scale defects in collision cascades. *Epl* **110** (2015).

[121] Golubov, S. I., Barashev, A. V. & Stoller, R. E. *Radiation damage theory*, vol. 1 (Elsevier Inc., 2012), 1 edn.

[122] Sizmann, R. The effect of radiation upon diffusion in metals. *J. Nucl. Mater.* **69-70**, 386–412 (1978).

[123] Debelle, A. *et al.* How relative defect migration energies drive contrasting temperature-dependent microstructural evolution in irradiated ceramics. *Phys. Rev. Mater.* **2**, 1–8 (2018).

[124] Dederichs, P. H., Lehmann, C., Schober, H. R., Scholz, A. & Zeller, R. Lattice theory of point defects. *J. Nucl. Mater.* **70**, 176–199 (1978).

[125] Miao, Y. *et al.* The evolution mechanism of the dislocation loops in irradiated lanthanum doped cerium oxide. *J. Nucl. Mater.* **445**, 209–217 (2014).

[126] Le Prioux, A., Fossati, P., Maillard, S., Jourdan, T. & Maugis, P. Empirical potential simulations of interstitial dislocation loops in uranium dioxide. *J. Nucl. Mater.* **479**, 576–584 (2016).

[127] Hull, D. & Bacon, D. J. *Introduction to Dislocations* (Butterworth-Heinemann, 2011), fifth edn.

[128] Chen, D. *et al.* The effects of loop size on the unfaulting of Frank loops in heavy ion irradiation. *J. Nucl. Mater.* **529**, 151942 (2020).

[129] Marian, J., Wirth, B. D. & Perlado, J. M. Mechanism of Formation and Growth of $< 100 >$ Interstitial Loops in Ferritic Materials. *Phys. Rev. E* **88**, 4 (2002).

[130] Soullard, J. Mise en evidence de boucles de dislocation imparfaites dans des echantillons de bioxyde d'uranium irradies. *J. Nucl. Mater.* **78**, 125–130 (1978).

[131] Debelle, A. *et al.* Lattice strain in irradiated materials unveils a prevalent defect evolution mechanism. *Phys. Rev. Mater.* **2**, 1–8 (2018).

[132] Onofri, C. *et al.* Full characterization of dislocations in ion-irradiated polycrystalline UO2. *J. Nucl. Mater.* **494**, 252–259 (2017).

[133] Ye, B. *et al.* Irradiation effects in UO_2 and CeO_2. *Journal of Nuclear Materials* **441**, 525–529 (2013).

[134] He, L. F. *et al.* In situ TEM observation of dislocation evolution in Kr-irradiated UO_2 single crystal. *J. Nucl. Mater.* **443**, 71–77 (2013).

[135] Martin, G. *et al.* Irradiation-induced heterogeneous nucleation in uranium dioxide. *Phys. Lett. A* **374**, 3038–3041 (2010).

[136] Sabathier, C. *et al.* In-situ TEM observation of nano-void formation in UO_2 under irradiation. *Nucl. Instrum. Methods Phys. Res., B* **326**, 247–250 (2014).

[137] Nogita, K. & Une, K. Irradiation-induced recrystallization in high burnup UO_2 fuel. *J. Nucl. Mater.* **226**, 302–310 (1995).

[138] Sonoda, T. *et al.* Transmission electron microscopy observation on irradiation-induced microstructural evolution in high burn-up UO_2 disk fuel. *Nucl. Instrum. Methods Phys. Res., B* **191**, 622–628 (2002).

[139] Moll, S. *et al.* Multistep damage evolution process in cubic zirconia irradiated with MeV ions. *J. Appl. Phys.* **106**, 2–11 (2009).

[140] Zinkle, S. J. & Snead, L. L. Influence of irradiation spectrum and implanted ions on the amorphization of ceramics. *Nucl. Instrum. Methods Phys. Res., B* **116**, 92–101 (1996).

[141] Benyagoub, A. & Thome, L. Amorphization mechanisms in ion-bombarded metallic alloys. *Phys. Rev.* **38**, 10205–10216 (1988).

[142] Lian, J. *et al.* Radiation-Induced amorphization of rare-Earth titanate pyrochlores. *Phys. Rev. B* **68**, 1–9 (2003).

[143] Motooka, T. & Holland, O. W. Amorphization processes in self-ion-implanted Si: Dose dependence. *Appl. Phys. Lett.* **58**, 2360–2362 (1991).

[144] Thomé, L. *et al.* Combined effects of nuclear and electronic energy losses in solids irradiated with a dual-ion beam. *Appl. Phys. Lett.* **102** (2013).

[145] Debelle, A. *et al.* Combined experimental and computational study of the recrystallization process induced by electronic interactions of swift heavy ions with silicon carbide crystals. *Phys. Rev. B* **86**, 2–5 (2012).

[146] Gao, F. & Weber, W. J. Cascade overlap and amorphization in 3C-SiC: Defect accumulation, topological features, and disordering. *Phys. Rev. B* **66**, 1–10 (2002).

[147] Gao, F., Bacon, D. J., Calder, A. F., Flewitt, P. E. & Lewis, T. A. Computer simulation study of cascade overlap effects in α-iron. *J. Nucl. Mater.* **230**, 47–56 (1996).

[148] Trachenko, K. Understanding resistance to amorphization by radiation damage. *J. Phys. Condens. Matter* **16** (2004).

[149] Trachenko, K., Pruneda, J. M., Artacho, E. & Dove, M. T. How the nature of the chemical bond governs resistance to amorphization by radiation damage. *Phys. Rev. B* **71**, 1–5 (2005).

[150] Chartier, A., Catillon, G. & Crocombette, J. P. Key role of the cation interstitial structure in the radiation resistance of pyrochlores. *Phys. Rev. Lett.* **102**, 5–8 (2009).

[151] Takano, T., Ohnuma, H., Ohtani, H., Nakajima, S. & Yamazaki, S. Method of manufacturing a semiconductor device (2000).

[152] Asahi, R., Morikawa, T., Ohwaki, T., Aoki, K. & Taga, Y. Visible-light photocatalysis in nitrogen-doped titanium oxides. *Science* **293**, 269–271 (2001).

[153] Plumton, D. L. & Kulcinshki, G. L. The magnitude and distribution of the excess interstitial fraction during heavy ion irradiation. *J. Nucl. Mater.* **133-134**, 444–447 (1985).

[154] Nordlund, K. Molecular dynamics simulation of ion ranges in the 1-100 keV energy range. *Comput. Mater. Sci.* **3**, 448–456 (1995).

[155] Hobler, G. & Betz, G. On the useful range of application of molecular dynamics simulations in the recoil interaction approximation. *Nucl. Instrum. Methods Phys. Res., B* **180**, 203–208 (2001).

[156] Nordlund, K., Djurabekova, F. & Hobler, G. Large fraction of crystal directions leads to ion channeling. *Phys. Rev. B* **94** (2016).

[157] Weber, W. J., Duffy, D. M., Thomé, L. & Zhang, Y. The role of electronic energy loss in ion beam modification of materials. *Curr Opin Solid State Mater Sci* **19**, 1–11 (2015).

[158] Backman, M. *et al.* Cooperative effect of electronic and nuclear stopping on ion irradiation damage in silica. *J. Phys. D: Appl. Phys* **45** (2012).

[159] Merkle, K. L. Fission-fragment tracks in metal and oxide films. *Phys. Rev. Lett.* **9**, 150–152 (1962).

[160] Izui, K. Fission fragment damage in semiconductors and ionic crystals. *J PHYS SOC JPN* **20**, 915–932 (1965).

[161] Toulemonde, M., Paumier, E. & C.Dufour. Thermal spike model in the electronic stopping power regime. *Radiat. Eff. Defects Solids* **126**, 201–206 (1993).

[162] Zhu, Y., Cai, Z. X., Budhani, R. C., Suenaga, M. & Welch, D. O. Structures and effects of radiation damage in cuprate superconductors irradiated with several-hundred-MeV heavy ions. *Phys. Rev.* **48**, 6436–6450 (1993).

[163] Jiang, N. Electron beam damage in oxides: a review. *Rep. Prog. Phys.* **79**, 16501 (2015).

[164] Egerton, R. F., Li, P. & Malac, M. Radiation damage in the TEM and SEM. *Micron* **35**, 399–409 (2004).

[165] Ewing, R. C., Weber, W. J. & Clinard, F. W. Radiation effects in nuclear waste forms for high-level radioactive waste. *Progress in Nuclear Energy* **29**, 63–127 (1995).

[166] Egerton, R. F., McLeod, R., Wang, F. & Malac, M. Basic questions related to electron-induced sputtering in the TEM. *Ultramicroscopy* **110**, 991–997 (2010).

[167] Backman, M. *et al.* Molecular dynamics simulations of swift heavy ion induced defect recovery in SiC. *Comput. Mater. Sci.* **67**, 261–265 (2013).

[168] Zhang, Y. *et al.* Ionization-induced annealing of pre-existing defects in silicon carbide. *Nat. Commun.* **6**, 1–7 (2015).

[169] Thomé, L. *et al.* Behavior of nuclear materials irradiated with a dual ion beam. *Nucl. Instrum. Methods Phys. Res., B* **326**, 219–222 (2014).

[170] Zhang, Y. *et al.* Influence of chemical disorder on energy dissipation and defect evolution in concentrated solid solution alloys. *Nat. Commun.* **6** (2015).

[171] Debelle, A. *et al.* Comprehensive study of the effect of the irradiation temperature on the behavior of cubic zirconia. *J. Appl. Phys.* **115**, 1–9 (2014).

[172] Gan, J., Was, G. S. & Stoller, R. E. Modeling of microstructure evolution in austenitic stainless steels irradiated under light water reactor condition. *J. Nucl. Mater.* **299**, 53–67 (2001).

[173] Satoh, Y., Sohtome, T., Abe, H., Matsukawa, Y. & Kano, S. Athermal migration of vacancies in iron and copper induced by electron irradiation. *Philos. Mag.* **97**, 638–656 (2017).

[174] Gemmell, D. S. Channeling and related effects in the motion of charged particles through crystals. *Rev. Mod. Phys.* **46**, 129–227 (1974).

[175] Davies, J. A., McIntyre, J. D., Cushing, R. L. & Lounsbury, M. The range of Alkali metal ions of kiloelectron volt energies in Aluminum. *Can. J. Chem.* **38**, 1535–1546 (1960).

[176] Kornelsen, E. V., Brown, F., Davies, J. A., Domeij, B. & Piercy, G. R. Penetration of Heavy Ions of keV Energies into Monocrystalline Tungsten. *Phys. Rev.* **136**, 849–858 (1964).

[177] Robinson, M. T. & Oen, O. S. The channeling of energetic atoms in crystal lattices. *Appl. Phys. A* **2**, 30–32 (1963).

[178] Oen, O. S. & Robinson, M. T. The effect of channeling on displacement cascade theory. *Appl. Phys. Lett.* **2**, 83–85 (1963).

[179] Feldman, L. C. & Rodgers, J. W. Depth profiles of the lattice disorder resulting from ion bombardment of silicon single crystals. *J. Appl. Phys.* **41**, 3776–3782 (1970).

[180] Feldman, L. C., Mayer, J. W. & Picraux, S. T. *Materials Analysis by Ion Channeling: Submicron Crystallography* (Academic Press, 1982).

[181] Lindhard, J. Motion of swift charged particles, as influenced by strings of atoms in crystals. *Phys. Lett.* **12**, 126–128 (1964).

[182] Lindhard, J. Influence of Crystal Lattice on Motion of Energetic Charged Particles. *Kgl. Dan. Vidensk. Selsk., Mat.-Fys. Medd.* **34** (1965).

[183] Bøgh, E. Defect studies in crystals by means of channeling. *Can. J. Phys.* **46**, 653–662 (1968).

[184] Nguyen, T. H. *Channelling investigation of the behaviour of urania under low-energy ion irradiation.* Ph.D. thesis, Université Paris Sud - Paris XI (2013). URL https://tel.archives-ouvertes.fr/tel-00966967.

[185] Haddad, Y. *Investigation of the formation mechanisms of the high burnup structure in the spent nuclear fuel - experimental simulation with ions beams.* Ph.D. thesis, Université Paris-Saclay (2017).

[186] Quéré, Y. About the dechanneling due to dislocation loops. *Radiat. Eff.* **38**, 131–132 (1978).

[187] Wieluński, L., Wieluńska, D., Della Mea, G. & Turos, A. Analysis of the dechannelling mechanism due to dislocations. *Nucl. Instrum. Methods* **168**, 323–328 (1980).

[188] Batterman, B. W. & Cole, H. Dynamical diffraction of x rays by perfect crystals. *Rev. Mod. Phys.* **36**, 681–717 (1964).

[189] Ehrhart, P. Investigation of radiation damage by X-ray diffraction. *J. Nucl. Mater.* **216**, 170–198 (1994).

[190] Kittel, C. *Introduction to Solid State Physics* (Wiley, 2004), 8th edn.

[191] Channagiri, J. *Strain and defects in irradiated materials – A study using X-ray diffraction and diffuse scattering.* Ph.D. thesis, Université de Limoges (2015).

[192] Debelle, A. & Declémy, A. XRD investigation of the strain/stress state of ion-irradiated crystals. *Nucl. Instrum. Methods Phys. Res., B* **268**, 1460–1465 (2010).

[193] Bachiller-Perea, D., Debelle, A., Thomé, L. & Crocombette, J. P. Study of the initial stages of defect generation in ion-irradiated MgO at elevated temperatures using high-resolution X-ray diffraction. *J. Mater. Sci.* **51**, 1456–1462 (2016).

[194] Willis, B. T. M. Neutron diffraction studies of the actinide oxides II. Thermal motions of the atoms in uranium dioxide and thorium dioxide between room temperature and 1100 °C. *Proc. Math. Phys. Eng. Sci.* **274**, 134–144 (2006).

[195] Willis, B. T. & Hazell, R. G. Re-analysis of single-crystal neutron-diffraction data on UO_2 using third cumulants. *Acta Cryst.* **36**, 582–584 (1980).

[196] Boulle, A. & Debelle, A. Statistical Nature of Atomic Disorder in Irradiated Crystals. *Phys. Rev. Lett.* **116**, 1–5 (2016).

[197] Channagiri, J., Boulle, A. & Debelle, A. Diffuse X-ray scattering from ion-irradiated materials: A parallel-computing approach. *J. Appl. Crystallogr.* **48**, 252–261 (2015).

[198] Prince, E. (ed.) *International Tables for Crystallography, Volume C* (2004), third edn.

[199] Shao, L. & Nastasi, M. Methods for the accurate analysis of channeling Rutherford backscattering spectrometry. *Appl. Phys. Lett.* **87** (2005).

[200] Zhang, Y. *et al.* Response of strontium titanate to ion and electron irradiation. *J. Nucl. Mater.* **389**, 303–310 (2009).

[201] Jin, K. *et al.* Channeling analysis in studying ion irradiation damage in materials containing various types of defects. *J. Nucl. Mater.* **517**, 9–16 (2019).

[202] Robinson, M. T. & Oen, O. S. Computer studies of the slowing down of energetic atoms in crystals. *Phys. Rev.* **132**, 2385–2398 (1963).

[203] Barrett, J. H. Location of shoulders in channeling phenomena. *Phys. Rev.* **166**, 219–221 (1968).

[204] Barrett, J. H. Monte carlo channeling calculations. *Phys. Rev. B* **3**, 1527–1547 (1971).

[205] Albertazzi, E. & Lulli, G. Monte Carlo simulation of ion implantation in crystalline SiC. *Nucl. Instrum. Methods Phys. Res., B* **120**, 147–150 (1996).

[206] S. Oen, O. & T. Robinson, M. Computer studies of the reflection of light ions from solids. *Nucl. Instrum. Methods* **132**, 647–653 (1976).

[207] Smulders, P. J. & Boerma, D. O. Computer simulation of channeling in single crystals. *Nucl. Instrum. Methods Phys. Res., B* **29**, 471–489 (1987).

[208] Lulli, G. *et al.* Determination of He electronic energy loss in crystalline Si by Monte-Carlo simulation of Rutherford backscattering-channeling spectra. *Nucl. Instrum. Methods Phys. Res., B* **170**, 1–9 (2000).

[209] Albertazzi, E., Bianconi, M., Lulli, G., Nipoti, R. & Cantiano, M. Different methods for the determination of damage profiles in Si from RBS-channeling spectra: a comparison. *Nucl. Instrum. Methods Phys. Res., B* **118**, 128–132 (1996).

[210] Bianconi, M. *et al.* RBS-channeling analysis of virgin 6H-SiC : Experiments and Monte Carlo simulations. *Nucl. Instrum. Methods Phys. Res., B* **136-138**, 1267–1271 (1998).

[211] Lulli, G. *et al.* Interpretation of ion-channeling spectra in ion-implanted Si with models of structurally relaxed point defects and clusters. *Phys. Rev. B Condens. Matter Mater. Phys.* **69**, 1–7 (2004).

[212] Bianconi, M. *et al.* Channeling characterization of defects in silicon: An atomistic approach. *Nucl. Instrum. Methods Phys. Res., B* **230**, 185–192 (2005).

[213] Nowicki, L., Turos, A., Ratajczak, R., Stonert, A. & Garrido, F. Modern analysis of ion channeling data by Monte Carlo simulations. *Nucl. Instrum. Methods Phys. Res., B* **240**, 277–282 (2005).

[214] Dygo, A. & Turos, A. Small angle scattering by screened coulomb fields. *Radiat. Eff.* **85**, 237–242 (1984).

[215] Nowicki, L., Turos, A., Choffel, C., Garrido, F. & Thomé, L. Quasiepitaxial growth of a monoclinic phase on single crystals upon leaching. *Phys. Rev. B Condens. Matter Mater. Phys.* **56**, 534–542 (1997).

[216] Turos, A., Jozwik, P., Nowicki, L. & Sathish, N. Ion channeling study of defects in compound crystals using Monte Carlo simulations. *Nucl. Instrum. Methods Phys. Res., B* **332**, 50–55 (2014).

[217] Jozwik, P. *et al.* Monte Carlo simulations of ion channeling in crystals containing dislocations and randomly displaced atoms. *J. Appl. Phys.* **126**, 1–11 (2019).

[218] Barrett, J. H. Methods of channeling simulation. *Nucl. Instrum. Methods Phys. Res., B* **44**, 367–372 (1990).

[219] Yuan, B., Yu, P. C. & Tang, S. M. A database method for binary atomic scattering angle calculation. *Nucl. Instrum. Methods* **83**, 413–418 (1993).

[220] Arstila, K., Sajavaara, T. & Keinonen, J. Monte Carlo simulation of multiple and plural scattering in elastic recoil detection. *Nucl. Instrum. Methods Phys. Res., B* **174**, 163–172 (2001).

[221] Zhang, S. *et al.* Radiation damage buildup by athermal defect reactions in nickel and concentrated nickel alloys. *Mater. Res. Lett.* **5**, 433–439 (2017).

[222] Bacri, C. O. *et al.* SCALP, a platform dedicated to material modifications and characterization under ion beam. *Nucl. Instrum. Methods Phys. Res., B* **406**, 48–52 (2017).

[223] Gentils, A. & Cabet, C. Investigating radiation damage in nuclear energy materials using JANNuS multiple ion beams. *Nucl. Instrum. Methods Phys. Res., B* **447**, 107–112 (2019).

[224] Borschel, C. & Ronning, C. Ion beam irradiation of nanostructures - A 3D Monte Carlo simulation code. *Nucl. Instrum. Methods Phys. Res., B* **269**, 2133–2138 (2011).

[225] Jin, X. *et al.* New developments in the simulation of Rutherford backscattering spectrometry in channeling mode using arbitrary atom structures. *Model. Simul. Mat. Sci. Eng.* **28**, 075005 (2020).

[226] Cameron, R. J. Elastic Scattering of Alpha-Particles by Oxygen. *Phys. Rev.* **90**, 839–844 (1953).

[227] Nordlund, K. & Hobler, G. Dependence of ion channeling on relative atomic number in compounds. *Nucl. Instrum. Methods Phys. Res., B* **435**, 61–69 (2018).

[228] McQuarrie, D. A. *Statistical Mechanics* (Harper & Row, New York, 1976).

[229] Dolling, G., Cowley, R. A. & Woods, A. D. B. The Crystal Dynamics of Uranium Dioxide. *Can. J. Phys.* **43**, 1397–1413 (1965).

[230] Garrido, F., Nowicki, L. & Thomé, L. Channeling investigation of the crystalline structure of U4 O9-y. *Phys. Rev. B Condens. Matter Mater. Phys.* **74**, 1–13 (2006).

[231] Toader, O. F. & Naab, F. U. Beam profiling and measurement at MIBL. *Proceedings of DIPAC09, Basel, Switzerland* 333–335 (2009).

[232] Atkinson, K. E. *An Introduction to Numerical Analysis* (New York, 1989), 2nd edn.

[233] Hou, M. & Robinson, M. T. Computer studies of low energy scattering in crystalline and amorphous targets. *Nucl. Instrum. Methods* **132**, 641–645 (1976).

[234] Byggmästar, J., Granberg, F. & Nordlund, K. Effects of the short-range repulsive potential on cascade damage in iron. *J. Nucl. Mater.* **508**, 530–539 (2018).

[235] Aidhy, D. S. *et al.* Point defect evolution in Ni, NiFe and NiCr alloys from atomistic simulations and irradiation experiments. *Acta Mater.* **99**, 69–76 (2015).

[236] Chartier, A. & Marinica, M. C. Rearrangement of interstitial defects in alpha-Fe under extreme condition. *Acta Mater.* **180**, 141–148 (2019).

[237] Devanathan, R., Weber, W. J. & Gale, J. D. Radiation tolerance of ceramics - Insights from atomistic simulation of damage accumulation in pyrochlores. *Energy Environ. Sci.* **3**, 1551–1559 (2010).

[238] Debelle, A., Boulle, A., Chartier, A., Gao, F. & Weber, W. J. Interplay between atomic disorder, lattice swelling, and defect energy in ion-irradiation-induced amorphization of SiC. *Phys. Rev. B Condens. Matter Mater. Phys.* **90**, 13–17 (2014).

[239] Morelon, N. D., Ghaleb, D., Delaye, J. M. & Van Brutzel, L. A new empirical potential for simulating the formation of defects and their mobility in uranium dioxide. *Philos. Mag.* **83**, 1533–1550 (2003).

[240] Aidhy, D. S., Millett, P. C., Desai, T., Wolf, D. & Phillpot, S. R. Kinetically evolving irradiation-induced point defect clusters in UO_2 by molecular dynamics simulation. *Phys. Rev. B Condens. Matter Mater. Phys.* **80**, 1–9 (2009).

[241] Limoges, Y., Rahman, A., Hsieh, H. & Sidney, Y. Computer simulation studies of radiation induced amorphization. *J. Non-Cryst. Solids* **99**, 75–88 (1988).

[242] Soullard, J. High voltage electron microscope observations of UO_2. *J. Nucl. Mater.* **135**, 190–196 (1985).

[243] Stoller, R. E. *et al.* On the use of SRIM for computing radiation damage exposure. *Nucl. Instrum. Methods Phys. Res., B* **310**, 75–80 (2013).

[244] Xu, H., Osetsky, Y. N. & Stoller, R. E. Cascade annealing simulations of bcc iron using object kinetic Monte Carlo. *J. Nucl. Mater.* **423**, 102–109 (2012).

[245] Jourdan, T. & Crocombette, J. P. On the transfer of cascades from primary damage codes to rate equation cluster dynamics and its relation to experiments. *Comput. Mater. Sci.* **145**, 235–243 (2018).

[246] Gao, F., Bacon, D. J., Barashev, A. V. & Heinisch, H. L. Kinetic Monte Carlo annealing simulation of damage produced by cascades in alpha-iron. *Mater. Res. Soc. Symp. Proc.* **540**, 703–708 (1998).

[247] Stukowski, A. A triangulation-based method to identify dislocations in atomistic models. *J. Mech. Phys. Solids* **70**, 314–319 (2014).

[248] Onofri, C. *et al.* Evolution of extended defects in polycrystalline UO_2 under heavy ion irradiation: Combined TEM, XRD and Raman study. *Nucl. Instrum. Methods Phys. Res., B* **374**, 51–57 (2016).

[249] Jin, X., Boulle, A., Chartier, A., Crocombette, J.-p. & Debelle, A. Analysis of strain and disordering kinetics based on combined RBS-channeling and X-ray diffraction atomic-scale modelling. *Acta Materialia* **201**, 63–71 (2020).

[250] Boulle, A., Chartier, A., Debelle, A., Jin, X. & Crocombette, J.-P. A reciprocal space approach to retrieving strain and disorder in molecular dynamics simulation: the example of radiation damage. *To be published* (2020).

[251] Nowicki, L. *et al.* Defect analysis of NiMnSb epitaxial layers. *Nucl. Instrum. Methods Phys. Res., B* **240**, 356–359 (2005).

[252] Debelle, A., Boulle, A., Garrido, F. & Thomé, L. Strain and stress build-up in He-implanted UO_2 single crystals: An X-ray diffraction study. *J. Mater. Sci.* **46**, 4683–4689 (2011).

[253] Van Brutzel, L., Delaye, J. M., Ghaleb, D. & Rarivomanantsoa, M. Molecular dynamics studies of displacement cascades in the uranium dioxide matrix. *Philos Mag* **83**, 4083–4101 (2003).

[254] Dederichs, P. H. The theory of diffuse X-ray scattering and its application to the study of point defects and their clusters. *J Phys F Met Phys* **3**, 471–496 (1973).

[255] Ullah, M. W. *et al.* Evolution of irradiation-induced strain in an equiatomic NiFe alloy. *Scr. Mater.* **140**, 35–39 (2017).

[256] Goyal, A. *et al.* The conundrum of relaxation volumes in first-principles calculations of charged defects in UO_2. *Appl. Sci.* **9**, 1–24 (2019).

[257] Freyss, M., Petit, T. & Crocombette, J. P. Point defects in uranium dioxide: Ab initio pseudopotential approach in the generalized gradient approximation. *J. Nucl. Mater.* **347**, 44–51 (2005).

[258] Virtanen, P. *et al.* SciPy 1.0: fundamental algorithms for scientific computing in Python. *Nat. Methods* **17**, 261–272 (2020).

[259] Moll, S. *et al.* Damage processes in MgO irradiated with medium-energy heavy ions. *Acta Mater.* **88**, 314–322 (2015).

[260] Velişa, G. *et al.* Multi-axial and multi-energy channeling study of disorder evolution in ion-irradiated nickel. *J. Nucl. Mater.* **525**, 92–101 (2019).

[261] Jin, K., Bei, H. & Zhang, Y. Ion irradiation induced defect evolution in Ni and Ni-based FCC equiatomic binary alloys. *J. Nucl. Mater.* **471**, 193–199 (2016).

[262] Gibbons, J. Ion implantation in semiconductors - Part II: Damage production and annealing. *Proc. IEEE* **60** (1972).

[263] Malerba, L. *et al.* Comparison of empirical interatomic potentials for iron applied to radiation damage studies. *J. Nucl. Mater.* **406**, 19–38 (2010).

[264] Nordlund, K., Beck, U., Metzger, T. H. & Patel, J. R. Diffuse X-ray streaks from stacking faults in Si analyzed by atomistic simulations. *Appl. Phys. Lett.* **76**, 846–848 (2000).

[265] Boulle, A. *et al.* X-ray diffuse scattering from stacking faults in thick 3C-SiC single crystals. *Appl. Phys. Lett.* **89**, 2006–2008 (2006).

[266] Favre-Nicolin, V., Coraux, J., Richard, M. I. & Renevier, H. Fast computation of scattering maps of nanostructures using graphical processing units. *J. Appl. Cryst.* **44**, 635–640 (2011).

[267] Ma, P.-W. & Dudarev, S. L. The universality of point defect structure in body-centred cubic metals. *To be submitted* (2020).

[268] Paakkari, T. A determination of the Debye-Waller temperature factor and the X-ray Debye temperature for Ni, Cr, Fe, Mo and W. *Acta Cryst.* **30**, 83–86 (1974).

[269] Weber, W. J. Models and mechanisms of irradiation-induced amorphization in ceramics. *Nucl. Instrum. Methods Phys. Res., B* **166**, 98–106 (2000).

[270] Hecking, N., Heidemann, K. F. & Te Kaat, E. Model of temperature dependent defect interaction and amorphization in crystalline silicon during ion irradiation. *Nucl. Instrum. Methods Phys. Res., B* **15**, 760–764 (1986).

[271] Jagielski, J. & Thomé, L. Damage accumulation in ion-irradiated ceramics. *Vacuum* **81**, 1352–1356 (2007).

[272] Jagielski, J. & Thomé, L. Multi-step damage accumulation in irradiated crystals. *Appl. Phys. A* **97**, 147–155 (2009).

[273] Jagielski, J. & Thomé, L. Discontinuous character of the damage build-up in the elastic collision regime. *Radiat. Eff. Defects Solids* **166**, 367–372 (2011).

Combinant RBS/C, diffraction des rayons X et modélisations à l'échelle atomique pour étudier des défauts induits par l'irradiation et des changements microstructuraux

Résumé : Les particules énergétiques sont souvent impliquées dans les activités de la société moderne. Ils ont contribué à l'essor de l'industrie des semi-conducteurs et pourront à l'avenir jouer un rôle important dans la mise en forme des matériaux de manière contrôlée. Cependant, leur nature énergétique pose de grands défis. Ainsi, il est essentiel d'avoir une compréhension globale des mécanismes sous-jacents des défauts induits par l'irradiation et des changements microstructuraux associés. Expérimentalement, les effets induits par l'irradiation peuvent être suivis par des techniques de caractérisation telles que la rétrodiffusion de Rutherford en mode canalisé (RBS/C) et la diffraction des rayons X (XRD), pour ne citer que ces deux car elles sont extrêmement sensibles aux perturbations au sein des cristaux. Cependant, il n'est pas aisé d'établir un lien clair entre le résultat de la mesure et la quantité et la nature des défauts, et ce lien est généralement fait à partir de modèles phénoménologiques.

Dans ce travail de thèse, afin de faire face à ce problème, nous avons couplé modélisations à l'échelle atomique et simulations de signaux de RBS/C et XRD. La première étape a consisté à améliorer un code de simulation RBS/C récemment développé qui peut générer des signaux à partir de structures atomiques. En modifiant les algorithmes décrivant les interactions ion-solide et en ajoutant de nouvelles fonctionnalités, nous avons amélioré la flexibilité du code et son applicabilité à différents types de matériaux. Par la suite, nous avons utilisé le code RBS/C amélioré avec un code pour la DRX, lui aussi utilisant les données de structures atomiques. Avec ces signaux, nous avons extraits des paramètres de désordre et de déformation élastique et nous avons déterminé les cinétiques d'évolution associées et ce, pour un matériau modèle, à savoir UO_2. Les défauts d'irradiation ont été générés par dynamique moléculaire (MD) avec la technique de l'accumulation de paires de Frenkel. Les cinétiques issues des modélisations présentent un accord qualitativement étroit avec celles déterminées expérimentalement, indiquant la validité de la méthodologie utilisée. La décomposition des cinétiques modélisées a permis de décrire de façon quantitative l'évolution des différents de types de défauts. Enfin, nous avons calculé les signaux RBS/C et XRD à partir de cellules modèles de Fe produites par MD et contenant chacune un type de défauts à une concentration donnée, les deux informations étant connues. Une comparaison claire du désordre et de la déformation élastique induits par les différents types de défauts dans Fe a été faite. La relation entre le rendement RBS/C et l'énergie des ions sonde a également été étudiée et la dépendance en énergie, fonction de la nature des défauts, a été établie. L'approche globale utilisée dans ce travail doit désormais être étendue et testée dans d'autres matériaux.

Mots clés : Effets d'irradiation, défauts cristallins, RBS/C, XRD, modélisation

Combining RBS/Channeling, X-ray diffraction and atomic-scale modelling to study irradiation-induced defects and microstructural changes

Abstract: Energetic particles are involved in many activities of modern society. They constitute a significant aspect of the semiconductor industry and may play important role in shaping materials in a controllable way in the future. However, their energetic nature also poses grand challenges, especially in the nuclear industry. Thus, it is crucial to have a a comprehensive understanding of the underlying mechanisms of irradiation-induced defects and the associated microstructural changes. Experimentally, irradiation-induced effects can be monitored by characterization techniques including, but not limited to, Rutherford backscattering spectrometry in channeling mode (RBS/C) and X-ray diffraction (XRD), because they are extremely sensitive to changes in the crystalline structure. However, it is not straightforward to establish a clear link between the characterization results and the defect quantity and nature, and this connection is usually made according to simple phenomenological models.

In this thesis work, in order to cope with this problem, we performed RBS/C and XRD atomic-scale modelling. The first step was to improve a recently developed RBS/C simulation code that can generate RBS/C signals from arbitrary atomic structures. By modifying the algorithms describing ion-solid interactions and adding new features, we enhanced the flexibility of the code and its applicability to different types of materials. Subsequently, we employed the improved RBS/C code with a XRD program to compute disordering and elastic strain kinetics of a model material, namely UO_2, as a function of irradiation fluence. Radiation defects in UO_2 were simulated by molecular dynamics (MD) calculations. Both the strain and disordering kinetics exhibit qualitatively close agreement with those determined experimentally, indicating the validity of the used methodology. The decomposition of the kinetics was performed in order to study the effect of each defect separately, which enables a quantitative description of the disordering and strain build-up processes. Finally, we computed RBS/C and XRD signals from Fe MD cells, each of which contains one single type of defects. A clear comparison of disorder and elastic strain induced by different types of defects in Fe was made. The relation between RBS/C yield and He energy was also studied using the Fe MD cells, which shows dependency with defect types. The global approach used in this work has the hope to be extended and tested in more materials.

Keywords: Radiation effect, irradiation-induced defect, RBS/C, XRD, modelling.

IRCER - UMR CNRS n° 7315
Centre Européen de la Céramique, 12 rue Atlantis - 87068 LIMOGES